



Politecnico di Bari

Repository Istituzionale dei Prodotti della Ricerca del Politecnico di Bari

Design and fabrication of a compact, flexible and biocompatible antenna for wearable sensing applications

This is a PhD Thesis

Original Citation:

Design and fabrication of a compact, flexible and biocompatible antenna for wearable sensing applications / Marasco, Ilaria. - ELETTRONICO. - (2022). [10.60576/poliba/iris/marasco-ilaria_phd2022]

Availability:

This version is available at <http://hdl.handle.net/11589/246020> since: 2022-12-17

Published version

DOI:10.60576/poliba/iris/marasco-ilaria_phd2022

Publisher: Politecnico di Bari

Terms of use:

(Article begins on next page)



Politecnico
di Bari

Department of Electrical and Information Engineering
ELECTRICAL AND INFORMATION ENGINEERING

Ph.D. Program

SSD: ING-INF/02–ELECTROMAGNETIC FIELDS

Final Dissertation

Design and fabrication of a compact,
flexible and biocompatible antenna for
wearable sensing applications

by

Ilaria Marasco

Supervisors:

Prof. Antonella D'Orazio

Prof. Massimo De Vittorio

Dr. Francesco Rizzi

Coordinator of Ph.D. Program:

Prof. Mario Carpentieri



Politecnico
di Bari

Department of Electrical and Information Engineering
ELECTRICAL AND INFORMATION ENGINEERING

Ph.D. Program

SSD: ING-INF/02–ELECTROMAGNETIC FIELDS

Final Dissertation

Design and fabrication of a compact,
flexible and biocompatible antenna for
wearable sensing applications

by

Ilaria Marasco

Referees:

Prof. Giuseppe Schettini

Prof. Marco Donald

Migliore

Supervisors:

Prof. Antonella D'Orazio

Prof. Massimo De Vittorio

Dr. Francesco Rizzi

Coordinator of Ph.D Program:

Prof. Mario Carpentieri

Contents

Introduction	2
1 State of the art	3
1.1 Antenna design requirements	5
1.2 Flexible substrates	9
1.3 Fabrication techniques	13
2 Theoretical overview	17
2.1 Figures of merit	18
2.2 SAR Evaluation	20
2.3 Design techniques: FEM, FDTD, MoM	20
2.4 Power link budget	25
3 Compact evolved patch antenna	29
3.1 Antenna design	30
3.1.1 Polyethylene Naphthalate (PEN)	31
3.2 Genetic algorithm: the evolved patch	32
3.3 Metamaterials: Split Ring Resonator	36
3.4 SAR simulations	41
3.5 Antenna fabrication	42
3.6 Characterization	45
3.7 Bending Analysis	48
4 Planar Inverted-F Antenna on flexible substrates	49
4.1 Design and simulations	50
4.2 Fabrication and characterization on PEN	54
4.3 Fabrication and characterization on flexible glasses	57
5 Chitosan-based Planar Inverted-F antenna	65
5.1 Chitosan Substrate synthesis	66
5.2 Design and simulations of a metallic chitosan-based antenna	67
5.2.1 Fabrication Protocol	71

<i>CONTENTS</i>	2
5.2.2 Characterization	73
5.3 Design and Simulation of a non-metallic PIFA	74
5.3.1 Fabrication	76
5.3.2 Device Characterization	79
6 Wearable system for vital parameters monitoring	81
6.1 Design of the System	83
6.2 First generation board: Proof of Concept	87
6.3 Second generation board: integration of the evolved patch antenna	88
6.3.1 Characterization of the system	89
6.3.2 Measurements Results	91
6.4 System Design in ISM Band	93
6.4.1 Characterization of the ISM Board	94
6.4.2 Results in ISM band: from single to multiple subjects	95
6.4.3 Summary of the sensor platform configurations	98
7 Conclusion	99
References	102

Introduction

High wearability and low intrusivity are increasingly common characteristics of new generations of electronic personal devices. Given the high number of devices used by the average person daily, having small and non-invasive devices becomes more and more important. In this scenario, wireless communications are crucial to open the door to new generations of wearable nodes connected to wireless sensor networks. In this technological transition, antennas play a fundamental role. Antennas for these new applications have to face several challenges. Firstly, the compactness of the footprint. Secondly, the flexibility of the substrate, improving the yield of the majority of non-invasive and wearable systems. Thirdly, optimal radiation properties, that combining high gains with low Specific Absorption Reference (SAR), minimize the risks on the human body application. All these peculiarities are very difficult to achieve and require several advanced techniques such as artificial intelligence algorithms fabricated using advanced manufacturing processes. In this thesis work, several wearables and flexible antennas for remote sensing platforms are exposed. The antennas are designed using several approaches to minimize their dimensions without affecting the radiation properties. Moreover, the effects on the human body are carefully evaluated using Finite-Different Time-Domain (FDTD) solvers. Finally, the integration of wearable antennas in a real scenario is presented. More in detail, the integration of wearable and biocompatible piezoelectric sensors with flexible patch antennas is described. The obtained radiofrequency system has a lightweight profile, is very compact and low consuming, and can monitor the Heart Rate (HR) of one to multiple patients from remote. This thesis work is structured as follows. In the first part, the state of the art as regards

flexible antennas and remote wearable sensing platforms is exposed. Chapter 2 follows a brief theoretical explanation of the mathematical instruments to characterize and design the flexible antennas and the radio link. In chapter 3, an evolved patch antenna is detailed. The antenna is a multilayer device composed of a radiative part designed through a genetic algorithm and loaded with a split-ring resonator. All the steps of the design and the fabrication protocol are exposed. In the end, the characterization of the device is provided. Chapter 4 presents two examples of Planar Inverted-F Antennas (PIFAs) on flexible substrates. In the first part, the design, fabrication, and characterization of a PEN-based PIFA antenna are reported. In the second section, the same antenna is replicated on a flexible glass substrate. Both two antennas present a very straightforward fabrication process suitable for rapid prototyping and mass production and can be exploited for wearable systems. Chapter 5 regards the design and fabrication of flexible antennas based on a plastic-free chitosan substrate. In particular, two generations of antennas are detailed, both based on the same geometry and a chitosan dielectric layer. The first uses metal traces based on silver nanoparticles, while the second is all based on biodegradable materials such as a PEDOT:PSS conductive layer. Antennas are characterized in terms of return loss and radiation properties and show to be an optimal choice for wireless sensor network applications. In chapter 6 the integration of a piezoelectric deformation sensor integrating patch antennas to build a wireless remote sensing platform is exposed. Three generations of boards are prototyped and tested with gradually decreasing power consumption and sizes. All three boards are characterized in terms of the degree of signal distortions and signal-to-noise ratio. Moreover, the third-generation board working in the Industrial, Scientific, and Medical (ISM) band is used to measure from one to three patients simultaneously. Finally, chapter 7 reports the conclusions and perspective of this work. All the reported fabrication protocols have been developed at the Center for Biomolecular Nanotechnologies (CBN) of Istituto Italiano di Tecnologia sited in Lecce.

Chapter 1

State of the art

With the maturity of fabrication processes, a multitude of biocompatible and flexible materials have been applied for sensing technologies to realize sensing platforms characterized by very high wearability combined with high sensitivities. The number of wearable flexible sensors is constantly increasing, and several highly sensitive platforms have been successfully applied for monitoring biological parameters. In [1] a wearable platform able to measure humidity has been proposed. The sensor is formed by patterning interdigitated electrodes made of graphene on a 40 μm -thick polyimide substrate. The working principle is based on the variation of resistance because of the humidity in the air. The sensor has been demonstrated to be very sensitive and able to monitor breath with low-invasive measurements. Another example of a pressure sensor is presented in [2]. The sensor is composed of micro conformal graphene electrodes (MGrEs) transferred to a PET substrate through a (UVA) adhesion layer. By sandwiching a Polydimethylsiloxane (PDMS) dielectric layer between the top MGrE and the bottom electrode, the authors obtained a capacitive pressure sensor with high sensitivity, fast response speed, ultralow detection limit, tuneable sensitivity, high flexibility, and high stability. Reference [3] details a new sensing platform able to monitor, at the same time, heartbeat and temperature. The sensor is composed of a core thermosensitive micro/nano porous fiber (graphene/ $\text{Fe}_2(\text{MoO}_4)_3$ /TPU) wrapped with nylon filament outside. The heartbeats are measured by ex-

exploiting the triboelectricity of the whole textile, while the sensitivity to the temperature is given by the thermosensitive core. The use of such minimally invasive sensors has opened up scenarios far beyond the simple use of wearable technology but has also enabled the realization of monitoring platforms inside the human body; unthinkable to achieve with other technologies. As an example, in [4] a flexible piezoelectric sensor for monitoring gastrointestinal (GI) motility has been presented. The sensor is placed within the gastrointestinal tract for the diagnosis and treatment of motility disorders, monitoring of ingestion to aid in the treatment of obesity, and development of flexible therapies in the form of GI electroceuticals. The main issue regarding this kind of technology is related to the reading setup which always requires wires and cumbersome interconnections that drastically increase the physical complexity of the application environment. To overcome this challenge, the next revolution in sensing platforms regards the integration of sensors in complex networks composed of several nodes able to wirelessly transmit information remotely. One of the main advantages of replacing cables with wireless transmissions is the minimizing of the impact of the sensors. The latter becomes extremely important in wearable or even endometrial sensing applications. For example, in [5] a wireless and battery-free cuff-type sensor for monitoring arterial blood flow is presented.

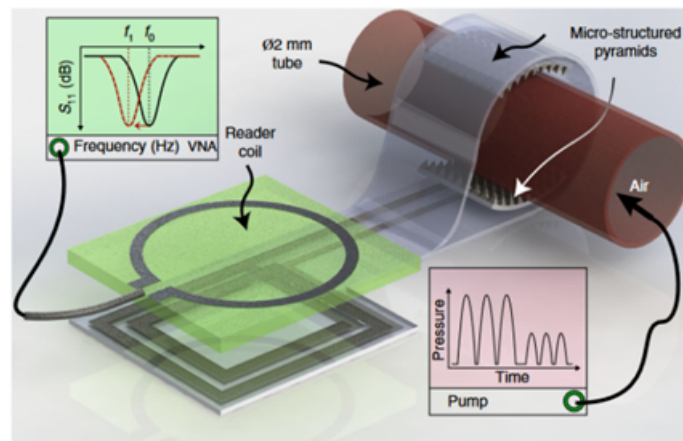


Figure 1.1: Schematic drawing of In vitro sensor characterization using an artificial artery model [5]

The system is formed of a thin and flexible structure easy to be wrapped around arteries of various sizes. In addition, the device is made entirely of biodegradable materials and is resorbed after several months. The wireless sensing is enabled using an external antenna which couples with an LCR resonator placed on the artery. An external antenna transmits power to the sensor which absorbs more power when the frequency of the transmitted signal matches the resonance value. In this scenario the role of antennas becomes crucial. Antennas convert electromagnetic waves traveling through the air to transmission lines-guided signals and vice versa and represent the most important building block of any wireless system. However, the design and fabrication of antennas suitable for such systems are challenging in terms of design requirements and fabrication techniques.

1.1 Antenna design requirements

From a design point of view, wearable antennas have to satisfy several requirements. First, the overall footprint has to be as smaller as possible to be unobtrusive. The commonly used substrates for flexible electronics are very thin and characterized by low permittivity, hence compactness becomes very challenging to achieve; therefore, minimization techniques come to the aid. A very straightforward technique is the shorting pin [6]: a shortcut between the positive and the negative parts of the antenna. In [7] two shorting pins have been used to fabricate an electrically small antenna (ESA) [8] on a felt substrate. The antenna exhibits optimal performance even when applied to a human arm, despite compact dimensions ($70 \times 25 \text{ mm}^2$). One of the problems of this approach is the design of the interconnection in terms of feed position and length. The last becomes particularly challenging at gigahertz frequencies as the effect of a shorting pin is the increasing value of the input impedance of the antenna. An alternative approach is shown in ref. [9], where a high-dielectric constant substrate is exploited. A nanocomposite paper substrate with a high dielectric value (k) was used to miniaturize a dipole antenna working at 2.4 GHz up to 50%. An interesting approach is the optimization of the geometry of the antenna through the use of artifi-

cial intelligence optimization algorithms, such as Genetic Algorithm (GA). In general, the GA optimizes the features of a given population using Darwinian laws. The algorithm starts with a random population and iteration by iteration new generations are formed by combining the individuals. The Darwinian fitness of the elements is evaluated using a given cost function, and the individuals having the highest values mate to form new generations. Ref. [10] details the design of a waffle-type antenna using genetic algorithms (GAs) in the 402-405 MHz MICS band of a size potentially suitable for cardiac pacemakers. The antenna is treated as a set of pixels. Each gene can have a binary value, “1” if made of metal, “0” if made of dielectric material. The geometries produced by the algorithm are forced to have all the metal pixels connected. The fitness function considers only the return loss value in the frequency range of interest. The optimization of a Bow-tie fractal antenna is detailed in [11]. In this case, the genetic algorithm helps to find the most important parametric variations on the characteristics of the antenna. In [12] the authors optimize, through a GA, the gain of a wideband microstrip patch antenna. The proposed antenna exhibits a wide operating bandwidth of 450 MHz high gain and directivity of about 8.35 dB.

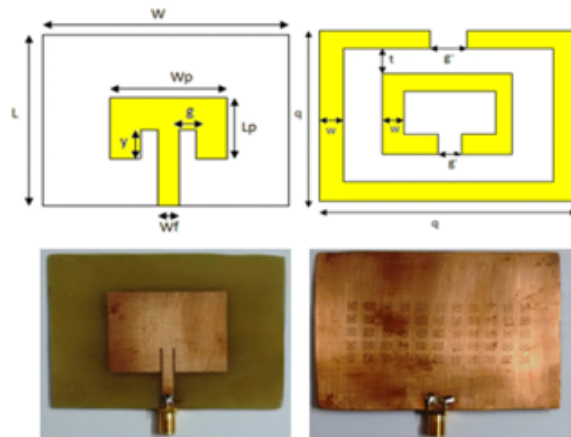


Figure 1.2: Geometry of the proposed metamaterials Wi-Fi antenna presented in [12]

Another example is reported in [13]; an evolved antenna based on a genetic algorithm is designed and fabricated. In this case, GA acts on the

geometry of the radiative part to enhance the gain value. In [14] a compact patch antenna has been optimized to work in the sub-6GHz band. The antenna has been optimized in terms of S_{11} and gain value at the frequency of interest and has been fabricated on a polyethylene naphthalate (PEN) biocompatible and flexible substrate, using a multi-material 3D printer. Another nature-inspired optimization algorithm is Particle Swarm Optimization (PSO). This algorithm follows the behavior of flocks of birds or shoals of fish. When an individual moves through a given direction is influenced by his past trials but also by the global trend of the swarm, hence it tries to find the optimal solution by considering not only his personal information but also the shared knowledge. This approach has been successfully applied to design ESAs for the first time in [15]. In [16] an ISM-band antenna has been optimized in terms of return loss at a given frequency (S_{11}), radiation pattern, and dimensions. The proposed antenna presents minimum area consumption of $435mm^2$ with a return loss of -30 dB and a gain of 10 dB. The algorithm has been applied also for the optimization of a flexible antenna for Radiofrequency Identification (RFID) [17]. Several parameters have been considered as input of the PSO algorithm to minimize the return loss, the bandwidth, and the gain of the device. Reference [18] details the optimization of a patch antenna using a PSO algorithm for its integration with a textile denim sensor. In contrast, a problem regarding GA and PSO is the cost function expression. Each antenna element of the set has to be evaluated through an electromagnetic solver and this comports huge computational costs. Therefore, in the last years, another strategy gaining interest is based on Artificial Neural Networks (ANNs). An ANN is a computer algorithm that emulates the behavior of a brain. The structure of an ANN is formed by an input layer linked to the output layer through a hidden section. The hidden layer is formed by vectors of neurons. Each neuron is modeled as a transfer function that combines the inputs to determine an output value. The way the neurons link the inputs to the outputs is specific to the neural network and is determined in the training initial phase. The main advantage of using ANN in comparison to other methods is that they do not need a cost function; after the training the algorithm can estimate the response of the antenna directly

from its geometry, speeding up the optimization. In [19] a method for the evaluation of the electromagnetic response of antennas in terms of the gain, radiation pattern, and S_{11} is presented. The approach was demonstrated to be effective in antenna optimization and very near to classical electromagnetic solver results, despite the very low resources required. An example of a flexible antenna optimized with ANN is reported in [20]. An ANN formed of 1 hidden layer of 15 neurons is presented. An error of less than 6% is produced during the learning, validation, and testing processes. In [21] an ANN was used to optimize the gain of a hexagonal shape slot antenna. In general, a drawback of small antennas is the low radiation efficiency. Hence, it is always necessary a trade-off between compactness and performance. In this sense, an interesting approach is the use of metamaterials to enhance the radiation properties of the antennas. A metamaterial is the expansion of the atom concept to a macroscopic scale. By arranging multiple cells having specific properties it is possible to tailor the electrical and magnetic characteristics of the entire structure. One of the commonest examples of metamaterial is the Split Ring Resonator (SRR) since its planar geometry and easy integration simplify the fabrication process. SRRs can be used as Artificial Magnetic Conductor (AMC) layers having effective permeability near zero, i.e. Zero Index metamaterials (ZIMs). ZIMs can be placed between the top layer and the ground plane of microstrip antennas. In this case, the ZIM acts as a very precise mirror that minimizes the back-reflected electromagnetic waves improving the directivity. In [22] a patch antenna based using a ZIM layer to enhance the gain is presented. The metamaterial structure is composed of very thin copper grids printed on the 2.65mil substrates (0.5 mm) with crossed dipole aperture lattices whose period p is equal to 17.6 mm. The antenna has been characterized showing a gain of 15.5 dB. In [23] a split-ring resonator-based metamaterial has been integrated with a patch antenna working in the C-Band. The results have been an enhancement of the bandwidth from 4.769 to 5.370 GHz, a better adaptation at the working frequency from -19.42 dB to -21.79 dB, and an increase of the gain from 5.36 dBi to 5.6 dBi. A problem arising from the use of metamaterials is the fabrication of the stack of metallic layers forming the antenna. In this sense, antennas suit-

able for wearable applications should be characterized by lightweight, mimic capabilities, and most important flexibility.

1.2 Flexible substrates

Flexible/stretchable antennas can be more conformally integrated into wearable electronics, drastically reducing the physical complexity of the application environment. In addition, due to the low density of most flexible substrates, the weight of microwave electronics can be drastically reduced. The state-of-the-art microstrip patch represents the best choice as regards flexible antennas in terms of facility of design and fabrication combined with very low costs. A microstrip patch antenna is formed by a dielectric material patterned with a radiative conductive part. The choice of the appropriate materials and fabrication technique takes into consideration several aspects such as the forming materials, i.e. substrate and metallic layers, the geometry of the antenna, its footprint, and the number of layers. Flexibility can be achieved by using appropriate substrates. The most used substrates are plastics because of their low costs and more straightforward fabrication techniques. A substrate can be characterized in terms of dielectric properties by two parameters, the relative dielectric constant (ϵ_r) and the loss tangent ($\tan\delta$). The use of materials with a high dielectric constant minimizes the footprint and the physical impact of the radiative region [24], while low dielectric losses enhance radiation efficiency. In the literature, several examples of flexible substrates applied to antennas are reported; polymers represent the most common solution. In [25] a Yagi Huda antenna fabricated on a Kapton substrate with a graphene conductive ink is shown. The antenna operates in a wide bandwidth starting from 3 GHz to 8 GHz covering three possible applications: the industrial, scientific, and medical (ISM) band type B at 5.8 GHz, the highest band of wireless local area network (WLAN)/Wi-Fi at 5 GHz, and the sub-6GHz of the 5G spectrum. Other examples of polymeric antennas based on Polyethylene Naphthalate (PEN) are presented in [14], [26], [27]. Polyethylene naphthalate (PEN) is a very attractive choice for flexible electronics since its low cost combined with good dielectric properties

($\epsilon_r = 2.9$; $\tan\delta = 0.005$); it also presents a high glass-transition temperature (T_g) of 250°C . Another interesting material is polyethylene terephthalate (PET), used in [28] for the fabrication of an RFID tag. The antenna is a dipole formed by two meander lines connected to a logical circuit chip. The substrate presents optimal dielectric properties, having $\epsilon_r = 2.9$ and $\tan\delta = 0.0002$. In [29], a Liquid Crystal Polymer (LCP) antenna is shown. The dielectric properties of the material are $\epsilon_r = 2.9$ and $\tan\delta = 0.0025$. The geometry is a tapered slot antenna working at 60 GHz. The authors claimed to have integrated the antenna in an array working for wireless personal area network (WPAN) applications. Reference [30] presents the design, fabrication, and characterization of a circularly polarised antenna with metamaterial loading-based LCP. The metal part is a $18\ \mu\text{m}$ -thick copper cladding, while the dielectric permittivity of the substrate settles around 2.9-3.2 with $\tan\delta$ of 0.0025.

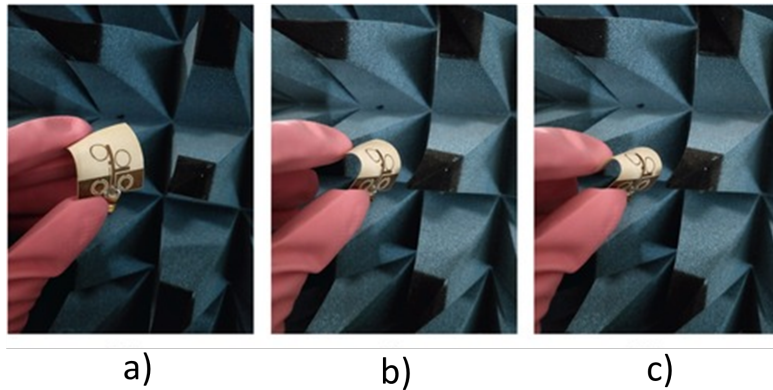


Figure 1.3: Images of the designed antenna at different bending angles: a) 15° , b) 30° and c) 90° . [28]

The downside of the rise of connected and flexible radiofrequency systems is the increasing use of halogenated or toxic compounds harmful to the environment. Therefore, a critical aspect concerns the environmental impact of the devices. The manufacture of antennas based on plastic-free and biodegradable substrates represents a strategic step forward in the direction of sustainability-conscious technology development. Regarding the integration of these eco-friendly substrates with flexible electronics, there are

two approaches. On one side, the bioreplacement solution tries to mimic the properties of monomers similar to petroleum-based. On the other side, bioadvantage polymers present the most interesting perspectives as, rather than replicating existing plastic materials, integrate ecological polymers upgrading the substrates with new peculiarities [31], [32]. In Reference [32] a bioadvantage approach has been successfully applied for the production of an antenna working at 2.5 GHz. The authors used a biological conductive ink based on cellulose fibers, zein proteins, and graphene nano-platelets (GnPs). Another very interesting work has been presented in [33] which details an antenna based on a cork substrate and having a conductive textile metallic part. However, the used substrate is not flexible, because a 2 mm-thick PVC layer has been used for passivation. Examples of flexible and eco-friendly antennas based on vegetal textile substrates have been presented in [34], [35]. The antennas have been fabricated on jute and knitted biodegradable synthetic fibers, respectively. They show optimal radiation properties combined with high flexibility; the drawback is the very huge footprint (almost $5 \times 5 \text{ cm}^2$), due to the low dielectric constant of the textiles. In literature there exist some examples of textile materials that are replacing both the dielectric substrate and the metallic components with conductive fabrics, to achieve all-textile antennas. For example, in [36] all-textile patch antennas are studied. In particular, the authors fabricate four different antennas for Bluetooth transmission having different metallic textiles and electrical polarizations. They tested silver-plated knitting and silver-copper-nickel-plated wooden textiles materials producing linearly polarised and left-hand-circular polarised patches. All the antennas work properly at the frequency of 2.4 GHz and can be folded up to a curvature radius of about 30 mm without significant modification on the resonance position. However, the gains are limited to the lower conductivities of the metallic layers of classical copper. Reference [37] presents six types of a 1.9 GHz single patch microstrip antenna having different combinations of woven patches and ground planes. All the woven antennas present good radiation performance. Moreover, the author demonstrates that the woven antenna with warp yarns parallel to the feeding direction exhibit a dipper return loss and a higher gain than the antenna

with a weft yarn parallel to the feeding direction. Other conductive materials suitable for flexible and stretchable electronics are liquid metals based on Gallium alloys. These materials offer attractive mechanical, electromagnetic, and chemical properties and have demonstrated their effectiveness in the fabrication of several antennas reported in the Ref [38].

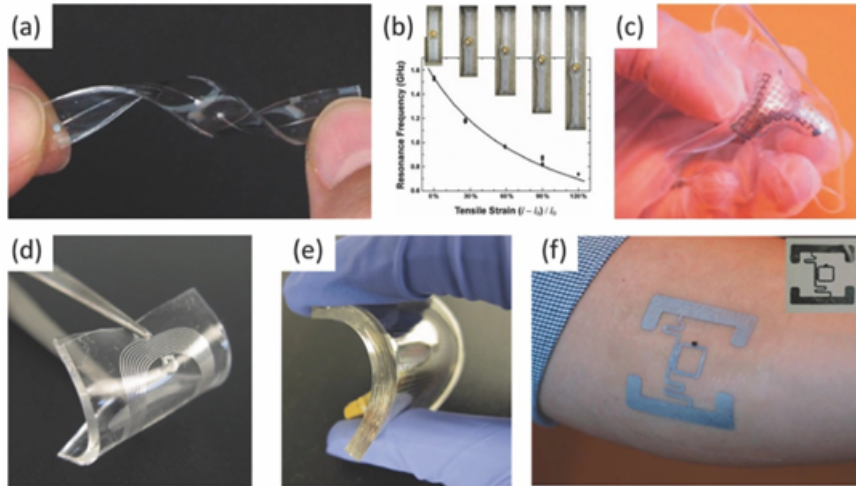


Figure 1.4: Examples of stretchable electronics. a) Stretchable dipole. b) Elongating a dipole shift in the resonant frequency for tuning the antenna mechanically or sensing strain. c) A soft loop antenna. d) A deformable coil antenna for wireless power transfer. e) An elastomeric patch antenna. f) RFID liquid metal with a chip placed on the arm. [38]

In [39] a Near Field Communication (NFC) antenna based on a liquid metal is presented. The system combines soft electronics materials and engineering designs with NFC functionality for human motion sensing. The liquid metal is based on Galinstan (a GaInSn alloy) and gives the system gel-like characteristics combined with a very high stretchability. Electromechanical characterization of the antenna reveals its robustness under large tensile and compressive strains, as well as more complex modes of deformation. In [40] a liquid conductive material composed of gallium indium eutectic (EGaIn) nanoparticles is embedded in an elastomeric matrix. In this case, the electrical conduction is induced by a pressure mechanical sintering. The peculiarity of this approach is the possibility to fabricate arbitrary shapes of antennas using a writing tool and it is very suitable for rapid prototyping of

flexible communication systems. To demonstrate the potentiality of the material, a dipole antenna has been fabricated by injecting the liquid metal into a PDMS microfluidic channel. The antenna does not radiate until pressure is applied. Moreover, by varying the area of the applied pressure it is possible to tune the resonant frequency in a range between 2 GHz and 3 GHz. The main problem in these kinds of liquid metal alloys is that the corrosive nature of Ga towards other metals might reduce the long-term stability of antenna performance. In this respect, conductive polymers (CP) represent a valid alternative. The conductivity of polymers is lower than metals, but it is high enough to build antennas; moreover, the biodegradability of such materials makes them a very interesting solution for eco-friendly wearable and edible sensors. Reference [41] details an RFID antenna made of PEDOT: PSS. The antenna has been fabricated by patterning a $1\mu\text{m}$ -thick layer of PEDOT: PSS on a biodegradable substrate. The gain of the antenna is - 8.5 dB. One of the biggest advantages of using liquid metals or CPs is the possibility of patterning using non-conventional processes such as subtractive metal etching, a very old process that is harmful to the environment.

1.3 Fabrication techniques

A very straightforward method for depositing metals on a flexible substrate is the screen-printing technique. In this technique, the metal ink is transferred only in certain areas of the substrate by the application of a stencil mask. Screen printing is very versatile and can be used for printing images on almost any solid material including polymeric or textile materials. It is a bottom-up approach allowing a minimum waste of material and a dramatic reduction of time and costs for fabrication. Several antennas have been fabricated exploiting this approach [42]. Reference [43] explores screen printing techniques for the fabrication of UHF RFID tags onto various low-cost and flexible substrates. More in detail, 20 different substrates have been tested among paper-based substrates, microfluidics, printed electronics, biodegradables, and flexible low-cost with and without adhesive. It is worth stressing that the printing technique has not changed in dependence of the substrate,

underlining the high potentiality of this technique in rapid prototyping antennas. In [44] two different fabric-based antenna designs called PICA and LOOP have been fabricated on a fabric substrate. The antennas have been tested in the proximity of a human body. Furthermore, tests on the stability against wrinkling, bending, fabric washing, or ironing have been performed. Another clear advantage of the screen-printing technique is the scalability of roll-to-roll productive systems. In Reference [45] 60 sheets of PEC antennas have been fabricated with a semi-automatic screen printer (ASYS EKRA X1-SL). The downside of this technique is related to the fact that there are many factors to be taken into account to achieve optimal results: the adhesion between substrate and stencil mask, the viscosity of the conductive ink, the velocity of the blade, and the applied pressure. Another valid bottom-up technique, combining high resolutions with rapid prototyping and low costs, is ink-jet printing. In ink-jet printing, the conductive ink is deposited on the substrate using hundred of nozzles electrically controlled. The deposition of the metal can be performed with very high precision. In the majority of printing systems, it is also possible to align the printing area to realize different stacks; moreover, multi-material ink-jet printers can be used also to deposit both dielectric and metallic inks making the system very attractive for the manufacturing of antennas. For example, in [25] a flexible graphene antenna printed on Kapton is reported. The prototyping has been performed using a Dimatix materials printer (DMP-2831), along with graphene ink (793663) from Sigma-Aldrich ($\sigma=2.5 \times 10^4 \pm 0.2 \times 10^4 \text{ S } m^{-1}$, after an annealing process of 20/30 min at 250/350 °C). The Kapton has been treated with an oxygen plasma to increase its hydrophilicity and to enhance the adhesion with the ink. The fabrication process was demonstrated to be effective as the antenna resonates at a frequency of 5.65 GHz with a radiation efficiency of 40 % and a maximum gain of 0 dB. As for screen printing, inkjet printing can be performed on almost any substrate very efficiently. In [46] an antenna has been produced by inkjet printing on a resin-coated paper substrate (thickness of 0.22 mm, ϵ_r of 3.2, and a $\tan\delta$ of 0.05). The results indicate that the antennas can work in most of the bands for mobile and wireless applications (PCS, UMTS, GSM1900, and WLAN) under flat and bent conditions. The

conductive ink is a silver nanoparticle-based ink from Sigma–Aldrich ($\sigma = 1 \times 10^7$ S/m). Reference [47] details on reconfigurable antenna printed on a paper substrate working between 1.9 GHz and 2.4 GHz. Measured results show that the antenna has a gain and efficiency of 2 dBi and 50 %, respectively. Ink-jet printing can be applied also to textile materials as detailed in [48]. The authors describe the fabrication of textile patch antennas working at 2-6 GHz. The chosen fabric is a standard 65/35 polyester cotton fabric, which is widely used in everyday clothing. The wettability of the surface concerning the ink has been increased using an adhesion layer made of Fabink UV-IF1. The prototypes of the antennas have been characterized in an anechoic chamber and the radiation patterns are similar to a regular antenna (maximum gain of 5.8 dB). The antenna does not significantly change its performance after bending around a 125-mm-radius cylinder. Inkjet printing can be used to print dielectric materials together with metallic parts, the latter becomes a crucial advantage in the manufacturing of multilayer antennas on flexible substrates. In Reference [49] a Multimaterial Yagi-Uda has been fabricated on an LCP flexible substrate. The Metallic patterns are achieved with Cabot CCI-300 silver nanoparticle-based ink, composed of a 20 w% suspension of silver nanoparticles within an alcohol-based solution; while the dielectric parts are obtained using a SU-8 polymer-based thick dielectric ink. The fabrication protocol has taken to a Yagi–Uda antenna exhibiting endfire realized gains up to 8 dBi in the 24.5 GHz ISM band. In conclusion, flexible antennas open the door to a multitude of applications especially in requiring lightweights, mimic capabilities, and minimally invasive environments. The combination with this kind of antenna becomes extremely interesting, especially in remote sensing platforms on flexible and wearable substrates. This integration can pave the way for a new class of non-invasive sensors connected to wireless sensor networks. Although these are very interesting perspectives, there are several challenges to overcome such as the design and the fabrication of antennas suitable for these systems. In this thesis, the design, fabrication, and characterization of flexible and wearable antennas for remote sensing applications have been reported. Different geometries of antennas as patches, evolved antennas, and PIFAs are described in detail

and then fabricated on several flexible substrates plastic-based (PEN, Polyimide or Kapton) and plastic-free and biodegradable (Chitosan) and flexible glasses. All the proposed antennas faced design challenges (miniaturization, increasing of the radiation properties, the inclusion of the effect of the body) and exploited some of the fabrication techniques previously detailed. All the prototypes have been characterized in terms of scattering parameter S_{11} and 3D or 2D radiation patterns. Finally, a practical application using flexible antennas in a complex system for remote heartbeat monitoring based on flexible piezoelectric sensors [50] has been proposed.

Chapter 2

Theoretical overview

The design of radio frequency antennas on wearable substrates presents several challenges to overcome. First, the antenna has to be designed properly depending on the application. Not only the geometry has to be opportunely designed to satisfy functional requirements in terms of radiation characteristics, but in wearable antennas, special care has to be taken of the effect that its integration can have on the human body. The design of these devices implies the determination of the electromagnetic (EM) field generated. In this scenario, computer-based numerical methods offer a disruptive help in solving Maxwell equations rapidly, even in complex situations. Besides the design of the antenna, another important aspect is the determination of the link budget. Radio propagation is extremely difficult to handle in wireless scenarios, not to mention in wireless sensor networks where strict power requirements are introduced. Several propagation models have been developed to formulate mathematical expressions of the necessary power transmission to establish a robust connection between the parts. In this chapter the theoretical instrument necessary for the design of the antennas and the radio links is detailed. In the first part, a brief description of the commonest figures of merit of the antennas is detailed. The second part is about the numerical simulations commonly included in computer-based algorithms for the estimation of the EM fields produced by the antennas. Finally, the third part details the radio propagation models used for the power-link budget of the

radio channels or to better analyze the antennas.

2.1 Figures of merit

The main function of antennas is to convert EM waves traveling through the air into transmission-line signals and vice-versa. The performance of an antenna can be evaluated by means of several figures of merit [51], [52]. The main parameter is the radiation intensity (U), defined as the power radiated from an antenna per unit-solid angle (Θ, Φ). The radiation intensity is evaluated for the far field and is defined in Equation 2.1:

$$U = \frac{r^2}{2} \text{Re}(E_\theta H_\phi) = \frac{r^2 E_\theta^2}{2Z_0} \quad (2.1)$$

where r is the distance from the source and Z_0 represents the impedance of the vacuum. The relation between received power and radiation intensity is given by Equation 2.2.

$$P_{rad} = \int_{\Omega} U d\Omega = \int_0^{2\pi} \int_0^\pi U(\theta, \phi) \sin\theta d\theta d\phi \quad (2.2)$$

If we consider an isotropic source, U is constant in all directions, and the radiation power can be evaluated as in Equation 2.3.

$$P_{rad} = 4\pi U_0 \quad (2.3)$$

Alternatively, we can define an isotropic antenna as an antenna having radiation intensity constant in all directions, as in Equation 2.4:

$$U_0 = \frac{P_{rad}}{4\pi} \quad (2.4)$$

The isotropy is only an idealization. In real cases, an antenna uses to radiate more power in a particular direction. The directivity expresses the concentration of the radiation intensity in a given direction and can be evaluated as in Equation 2.5.

$$D(\theta, \phi) = \frac{U(\theta, \phi)}{P_{rad}/4\pi} \quad (2.5)$$

In general, if no angles (Θ, Φ) are specified, the directivity is evaluated with the maximum value of the radiation intensity [53].

$$D = \max(D(\theta, \phi)) = \frac{\max(U(\theta, \phi))}{P_{rad}/4\pi} \quad (2.6)$$

Another important parameter is radiation efficiency which relates the power radiated to the input provided to the antenna.

$$\eta = \frac{P_{rad}}{P_i} \quad (2.7)$$

In general, there are several factors that can affect efficiency:

- ϵ_R : the reflection efficiency, related to impedance mismatching,
- ϵ_C : the conductive efficiency, related to the electrical conductivity,
- ϵ_D : the dielectric efficiency, related to the dielectric losses

Therefore, η is given by all three contributions as reported in Equation 2.8.

$$\eta = \epsilon_R \epsilon_C \epsilon_D \quad (2.8)$$

The combination of the directivity and the radiation efficiency of the antenna is the gain (G) expressed as in Equation 2.9.

$$G(\theta, \phi) = \eta D(\theta, \phi) \quad (2.9)$$

The value of the gain in all directions represents the 3D radiation pattern of the antenna. Another approach for representing this parameter is by means of 2D polar plots representing the gain in the θ and the ϕ planes. As for the directivity, if no angles are expressed, the value of the gain refers to the maximum value (see Equation 2.10).

$$G_0 = \eta \max(D(\theta, \phi)) = \eta D_0 \quad (2.10)$$

2.2 SAR Evaluation

A very important merit factor, especially in wearable antennas is the Specific Absorption Rate (SAR) coefficient. The SAR measures the quantity of energy emitted by the antenna and absorbed by the human tissues. This quantity strictly depends on the emitted power of the antenna and on the human tissue exposed to the radiation, i.e. electrical conductivity (σ) and density (ρ). In general, the SAR is an average of the absorbed power on a volume of tissue (V).

$$SAR = \frac{1}{V} \int_V \frac{\sigma(r)|E(r)|^2}{\rho(r)} dr \quad (2.11)$$

where E is the value of the electric field emitted by the antenna. The maximum limit of the SAR is set by law and in Europe is limited to 2.0 W/kg averaged over a volume of 10 grams of tissue. SAR is a critical parameter for the design of wearable antennas. If the SAR value exceeds the law limit the input power shall be reduced affecting the maximum transmitting range. A way to minimize the SAR is to increase the radiation efficiency, improve the impedance matching, and choose metals and dielectrics having low losses. Another strategy can be the optimization of the radiation pattern of the antenna to concentrate the radiation intensity in an opposite direction to the human body.

2.3 Design techniques: FEM, FDTD, MoM

The parameters listed above are essential for analyzing the performance of an antenna. However, their evaluation requires the calculation of the EM field, which is extremely difficult to determine by equations, especially for complex antenna geometries. A commonly used approach in the design of antennas is the evaluation of the EM field through computer-based numerical methods. Finite Difference Time Domain (FDTD), Finite Element Model (FEM), and Method of Momentum (MoM) represent the state of the art of numerical simulations. The FDTD method can be applied to a huge number of EM

problems including the design of antennas [54–60]. FDTD derives the EM field by solving Maxwell’s equations expressed in the time domain. As a first step, the geometry and the forming materials have to be specified. The material can be air, conductive materials, or dielectrics. New materials can be inserted by specifying their electromagnetic properties. After, the sources have to be defined in terms of position and excitation signals. The method is based on the solving of Maxwell’s equations in the time domain:

$$\frac{dE}{dt} = \frac{1}{\epsilon_0} \nabla_x H \quad (2.12)$$

$$\frac{dH}{dt} = -\frac{1}{\mu_0} \nabla_x E \quad (2.13)$$

Simplifying the problem in one-dimensional case, the equations (2.12) and (2.13) can be rewritten as:

$$\frac{dE_x}{dt} = -\frac{1}{\epsilon_0} \frac{dH_y}{dz} \quad (2.14)$$

$$\frac{dH_y}{dt} = -\frac{1}{\mu_0} \frac{dE_x}{dz} \quad (2.15)$$

where the EM wave is traveling in the z-axis direction. The idea to solve the problem is quite simple: the entire geometry is discretized in time and space, then the equations (2.14) and (2.15) are solved for each single element instant by instant using central difference approximations following Yee’s scheme [61]. More in specific, the vectors E_x and H_y are considered shifted in time and space of one-half of a unit cell (see Equations 2.16 and 2.17).

$$\frac{E_x^{n+\frac{1}{2}}(k) - E_x^{n-\frac{1}{2}}(k)}{\Delta t} = -\frac{1}{\epsilon_0} \frac{(H_y^n(k+1/2) - H_y^n(k-1/2))}{\Delta z} \quad (2.16)$$

$$\frac{(H_y^{n+1}(k + \frac{1}{2}) - H_x^n(k - \frac{1}{2}))}{\Delta t} = -\frac{1}{\mu_0} \frac{(E_x^{n+1/2}(k + 1) - E_x^{n-1/2}(k + 1))}{\Delta z} \quad (2.17)$$

The formula used for the FDTD algorithm can be found in Equations (2.18) and (2.19) as follows:

$$\frac{(E_x^{n+\frac{1}{2}}(k))}{1} = E_x^{n-\frac{1}{2}}(k) + \frac{\Delta t}{\epsilon_0} \frac{(H_y^n(k + 1/2) - H_y^n(k - 1/2))}{\Delta z} \quad (2.18)$$

$$\frac{H_y^{n+1}(k + \frac{1}{2})}{1} = H_x^n(k - \frac{1}{2}) + \frac{\Delta t}{\mu_0} \frac{(E_x^{n+1/2}(k + 1) - E_x^{n-1/2}(k + 1))}{\Delta z} \quad (2.19)$$

Therefore, for each time stamp, the algorithm evaluates the E_x and H_y for each point k . The determination of the spatial and time resolutions is extremely important to correctly estimate the EM fields and the related quantities, i.e., directivity, gain, and SAR [56]. In general, the minimum spatial resolution Δz is taken at a maximum equal to one-tenth of the smallest EM wavelength in the simulation. It is worth stressing that in the case of the presence of dielectric materials the wavelength to be considered is shorter than the one in the vacuum, therefore the spatial resolution needs to be refined. The timestamp is determined starting from the spatial resolution Δz . For stability reasons, the waves cannot propagate more than one Δz in a single time stamp. This condition is expressed as the Courant condition:

$$\Delta t \leq \frac{\Delta z}{c_0 \sqrt{d}} \quad (2.20)$$

where $d = 1, 2, 3$ for one-, two- or three-dimensional problems respectively. Commonly Δt is taken equal to:

$$\Delta t = \frac{\Delta z}{2c_0} \quad (2.21)$$

The FDTD method can be used to efficiently simulate the EM field generated by an antenna; however, in this case, the waves are not confined and propagate through the air. The grid in FDTD has to be finite, therefore the analysis domain has to be truncated at some point. The termination of the grids can cause reflections and then, influence the final result. To minimize this effect, FDTD uses boundary conditions. In this case, the points at the end of the grid are treated as special absorbers able to absorb all the incoming waves [62]. The biggest issue of FDTD is the numerical mesh dispersion effects and the analysis of bent structures. Bended surfaces take to errors due to the staircase approximation of arbitrarily shaped objects whose geometries do not conform to the Cartesian coordinates. The only way to mitigate these errors is by reducing the mesh size at the cost of a higher computational time. However, FDTD can be easily parallelized using cluster processors, reducing the computational times [63], [64].

FEM uses an approach quite similar to FDTD but it derives the EM field through Maxwell's equations in the frequency domain and can be easily applied to designing antennas [62], [65–67]. The method comprises four main steps:

- Discretizing the region of the solution into unit elements.
- Deriving equations for each element.
- Assembling of all elements.
- Solving the matrix system.

In the frequency domain the EM problem becomes linear, on the form:

$$F = Ku \quad (2.22)$$

where F is the output, u is the input and K is the property of the structure. Then, in the FEM the equation (2.23) is derived for all the elements of the

region of the solution and assembled in a unique system expressed in the forms of matrixes:

$$\{F\} = [K] \{u\} \quad (2.23)$$

The matrix $[K]$ is the stiffness matrix, and the element $k_{i,j}$ represents the effect on the i -th element due to the input applied to the j -th element. It is worth noting that the more the j -th input is near to the i -th element, the higher the reported effect is; therefore, the matrix k is a diagonal sparse matrix and has a form as the one below:

$$[K] = \begin{pmatrix} k_{11} & k_{12} & 0 & 0 & \dots & 0 & 0 & 0 \\ k_{21} & k_{22} & k_{23} & 0 & \dots & 0 & 0 & 0 \\ \dots & \dots \\ 0 & 0 & 0 & 0 & \dots & k_{n-1,n-2} & k_{n-1,n-1} & k_{n-1,n} \\ 0 & 0 & 0 & 0 & \dots & 0 & k_{n,n-1} & k_{n,n} \end{pmatrix} \quad (2.24)$$

This kind of matrixes is invertible by means of well-known algorithms so the $[K]^{-1}$ matrix can be given [68]. Finally, the solution to the problem can be found by inverting equation (2.25) as:

$$\{u\} = [K]^{-1} \{F\} [K] \quad (2.25)$$

Although a very similar approach, there are some essential differences between FEM and FDTD. FEM can handle unstructured grids, therefore is more suitable for complex geometries. Another big difference is that the algorithm constructs the whole matrix of the system and then finds a global solution, rather than solving the problem iteratively with a different approach as in FDTD. Indeed, in the FEM model, the complexity of the problem in-

creases exponentially with the dimensions of the model, while in FDTD the increase is almost linear. Moreover, it is more difficult to parallelize the FEM operations concerning FDTDs as the execution of the algorithm requires the inversion of the whole matrix. In conclusion, FEM methods are more suitable for small and complex geometries and narrow-band analysis, while FDTD can handle simpler but more extended geometries (especially if parallelized) and wide-band studies [69].

Another very powerful method extremely suitable for the analysis of antennas is the Method of Moments [70]. In this method, the structure is discretized as in the previous two, but in this case, the EM field is extrapolated using an approach based on the Green Functions. A Green Function represents the effects of an EM source in the surrounding space [71]. Therefore, the use of this kind of analysis avoids the truncation of the model at the boundaries. The MoM starts with the extrapolation of the current distribution of the structure, then expresses the EM field using the Green Function of the system as reported in equations (2.26) and (2.27).

$$E = E_i + \int \int \int_V G_{EJ}(r|r')J(r') + \int \int \int_V G_{EM}(r|r')M(r') \quad (2.26)$$

$$H = H_i + \int \int \int_V G_{HJ}(r|r')J(r') + \int \int \int_V G_{HM}(r|r')M(r') \quad (2.27)$$

2.4 Power link budget

The EM propagation in wires is very easy to model, but in the case of wireless radio channels, the paths of the waves are not easily predictable. If we consider an antenna transmitting the data from a sensor in an indoor scenario there are several objects and obstacles which interfere with the radio propagation. Propagation models have been formulated to estimate the way the EM waves propagate in a given environment. The simplest propagation model is the free space propagation; in this case, the waves travel in a

scenario without any obstacle or attenuation source [72]. This model gives a good estimation of the received power for short-range transmissions like in personal area networks, but it loses validity for long-range transmission. The power loss for a transmission length d and at a frequency f is given by Equation 2.28:

$$P_L = 20\log\left(\frac{4\pi d}{\lambda}\right) = 20\log\left(\frac{4\pi df}{c}\right) \quad (2.28)$$

The estimation of the path loss is of great importance for the power-link budget, i.e., the evaluation of the needed transmitting power to emit an intelligible signal at the receiving side. The equation that connects the input power (P_T) to the signal received (P_R) considers the gain of the receiving and the transmitting antennas (G_T, G_R) and the length of the radio link (d), Equation 2.29:

$$P_R = P_T + G_T + G_R - P_L = P_T + G_T + G_R + 20\log\left(\frac{c}{4\pi df}\right) \quad (2.29)$$

If two identical antennas transmitting at a given power at a given distance are considered, it is possible to obtain the gain of the antennas by inverting the Friis Equation (2.30).

$$G_T = G_R = \frac{1}{2}(P_R - P_T + 20\log\left(\frac{4\pi df}{c}\right)) \quad (2.30)$$

The method can be extended also in the case of two identical antennas and a third different antenna by the transfer gain method. As a first step the gain of the two identical antennas is determined by using the previous approach, and then the third gain is evaluated as in Equation (2.31)

$$G_3 = P_R - P_T + 20\log\left(\frac{4\pi df}{c}\right) - G \quad (2.31)$$

Equations 2.30 and 2.31 have been used in this work to build up a set-up (Figure 2.1) able to extrapolate the radiation pattern of the antennas and estimate the gain.

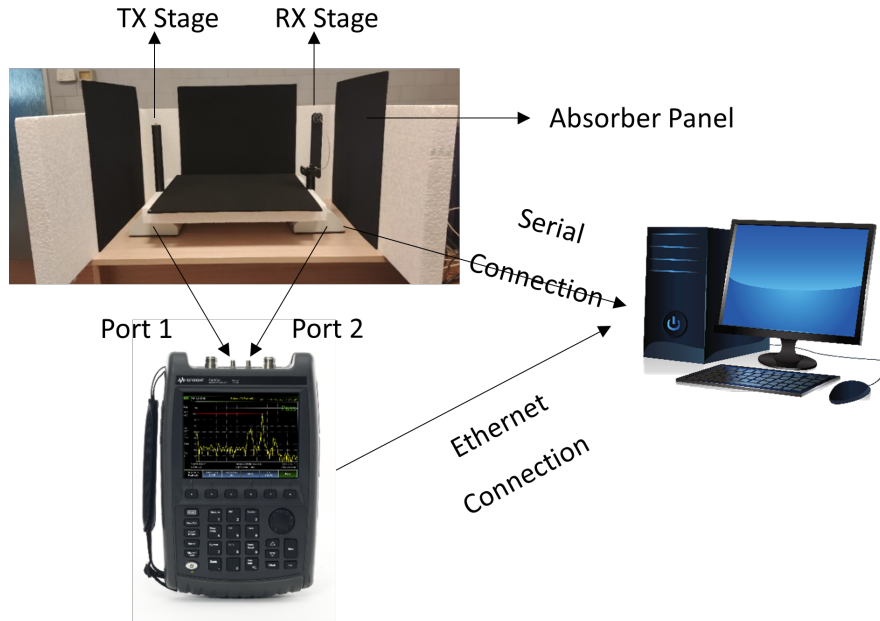


Figure 2.1: Measurements set-up with PC and VNA

More in detail, the set-up is composed of two supporting stages for the antennas, one fixed in position, the other rotating through a servo motor. The two stages are connected to a VNA, the transmitting antenna is plugged into port 1, while the rotating stage, holding the receiving antenna, is connected to port 2. The VNA is used to analyze the ratio between the transmitting and the received powers (module of the scattering parameter S_{21}). The VNA sends the S_{21} value to a computer, and the measure is repeated for different angles rotating the stage of the receiving antenna. At the end of the measurements, the computer can reconstruct the radiation pattern of the antennas and the gain value can be determined by applying Equation 2.30 in case of two identical antennas, or Equation 2.31 with the gain transfer method. Although the setup is very cheap and effective in evaluating the radiation properties there are some limitations. Firstly, the two antennas have to be aligned with very high precision and in the case of linear polarization, the device under test has to be in a parallel position. Secondly, the reflections of the environment cause artifacts, therefore, should be minimized using absorbing panels. Thirdly in the case of lightweight and flexible anten-

nas, the rotation movements cause vibrations and introduce noise; hence, the VNA has to be in average mode. The use of the free-space model together with the Friis equation is an optimal choice for the rapid estimation of the needed transmitting power in short-range applications; however, when the distance between sensors and reader increases the analysis raises in complexity, especially in indoor propagation at Gigahertz frequencies. When an EM wave propagates into an indoor scenario, it finds several objects on its way and scatters into several directions. The reflected signals interfere with each other depending on the frequency and their phases. In general, two signals can interfere in a destructive mode, i.e., the signals are strongly attenuated, or interfere constructively, enhancing their total power. In addition to interference phenomena, the waves can end up in several attenuation factors such as people moving in the environment, walls, floors, ceilings, and so on. All these factors can lead to a lower signal or a higher power level with respect to outdoor propagation, as the surrounding walls can act as a waveguide concentrating the signal and minimizing the dispersions [73].

Chapter 3

Compact evolved patch antenna

In this chapter, we detail the design and fabrication of a compact and flexible patch antenna. The antenna has been designed to be attached directly to the human body and to be integrated into a wireless and wearable sensor system based on a Polyethylene naphthalate substrate. We have chosen this geometry because of the presence of a ground plane which minimizes the back-radiation lowering the SAR. The footprint of the antenna has been optimized using a GA approach. The algorithm starts with a patch antenna working at 6 GHz, then thanks to the minimization technique adapts the antenna to work at 4 GHz. The antenna is subdivided into pixels [74], the material of each pixel is treated as a gene and the set of genes forming an antenna is identified as a chromosome. The cost function constructs the geometry of the patch starting from the chromosome values, then using an FDTD method evaluates the return loss of the antenna and the realized gain at the given frequency. The selection process of our GA is a chat roulette with a mutation rate of 1%. To further enhance the radiation property and to protect the body from the back radiation, we have integrated a split-ring-resonator (SRR) under the radiating layer which reflects the EM field generated by the antenna. After the optimization, the antenna is evaluated in terms of SAR. The last parameter is extremely important as the antenna shall be attached directly to the human body. The SAR is evaluated using an FDTD solver and a schematic phantom. The antenna presents a SAR of

0.1 mW/Kg, therefore 20 times lower than the law limit in Europe [75]. The multilayer stack has been fabricated on a PEN substrate through an ink-jet multi-material 3D printer based on silver-nanoparticles ink. The adhesion between the PEN substrate and the conductive ink has been increased by treating the substrate with plasma oxygen to increase the hydrophilicity of the surface. After the printing, the antenna is assembled and characterized in terms of scattering parameter S_{11} and radiation pattern using a VNA and an anechoic chamber respectively. The combination of the GA optimization algorithm and the use of the SRR takes to a very compact antenna having a footprint of about $17 \times 14 \text{ mm}^2$ and with optimal radiation properties with a gain of almost 2 dBi. The ink-jet 3D printer allows to increase in the speediness and the scalability of the fabrication and takes to a high yield of 10 PEN-based metamaterial evolved patch antennas in less than 2 hours.

3.1 Antenna design

The sketch of the device is shown in Figure 3.1.

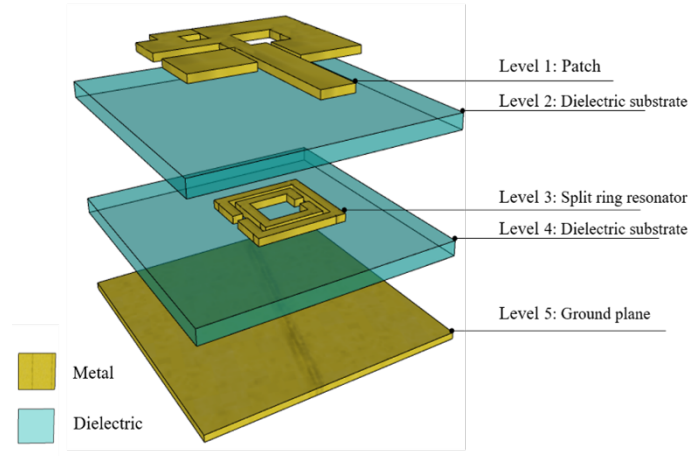


Figure 3.1: Exploded representation of the multilayer antenna

The proposed device is a multilayer antenna based on two dielectric layers made of Polyethylene Naphthalate (PEN) and three metallic ones. The first

layer (i.e the radiative one) is optimized by employing a Genetic algorithm to miniaturize the geometry; the second metallic layer is a metamaterial based on a Split Ring Resonator (SRR), used to improve the radiation properties of the device. Finally, there is a ground plane for protecting the body from backside radiation. The evolved antenna works at 4 GHz, in the sub-6GHz band of the 5G spectrum.

3.1.1 Polyethylene Naphthalate (PEN)

Polyethylene Naphthalate (PEN) is a semi-aromatic transparent polyester synthesized from naphthalene-2,6-dicarboxylic acid and ethylene glycol [76] as in Figure 3.2.

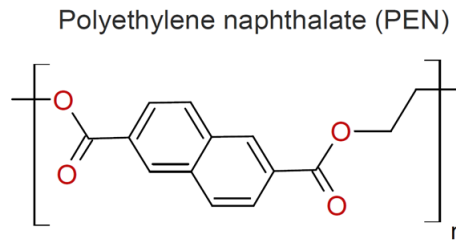


Figure 3.2: Polyethylene Naphtalate molecula

PEN is an optimal choice for flexible electronics for several reasons. As an example, differently from PET has lower oxygen permeability, and therefore is optimal for device passivation. In addition, PEN presents improved hydrolytic stability, which helps in printing processes. The mechanical properties of the materials are optimal for flexible applications as it is characterized by a higher tensile strength. Finally, PEN has one of the highest glass transition temperatures among other flexible materials ($120^{\circ}C$ vs $75^{\circ}C$ of PET) which simplifies the fabrication processes. Furthermore, it presents good resistance to acids and basis and a very high heat shrinkage coefficient [77, 78]. The substrate is $250 \mu m$ -thick with a relative dielectric constant equal to 2.9 and a loss tangent equal to 0.005.

3.2 Genetic algorithm: the evolved patch

The genetic algorithm is one of the most straightforward optimization methods for treating optimization problems by using a binary coding scheme. This algorithm was formalized for the first time in [79] and it is based on Darwinian laws. The workflow starts from an initial binary population representing the parents that evolve iteratively following a cost function. In Figure 3.3 the flowchart of GA is shown.

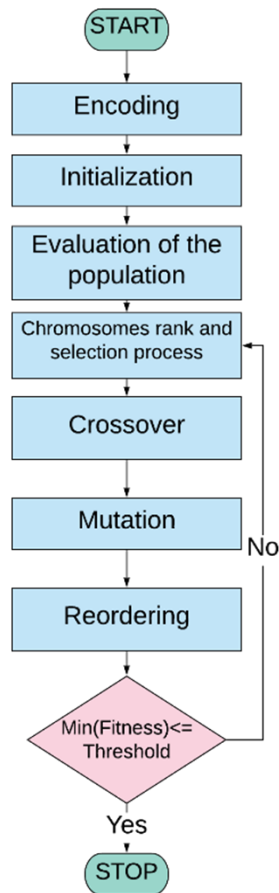


Figure 3.3: Flowchart of the Genetic Algorithm

1. Encoding: the solution to the problem is treated as a chromosome in which each gene represents a parameter to be optimized.

2. Initialization: Each member of the population is generated by randomly choosing its chromosome values.
3. Evaluation of the population: Darwinian fitness is related to each individual through a cost function, whose value represents the nearest to the optimal solution of the individual.
4. Chromosomes rank and selection process: the chromosomes mate accordingly to their cost values or in a random way
5. Crossover: the couples associated in the previous step generate new offspring having a combination of the genes of the parents.
6. Mutation: a random variation is applied to some elements of the population. This operation may increase the velocity of the algorithm convergence avoiding the stalling in the local minimum.
7. Reordering: the same operation of step 3 is performed on the new offspring.
8. Loop statement: in this step, it is decided if the algorithm has to be stopped according to the best fitness value and the maximum number of iterations. In case of a new iteration, the algorithm is repeated from Step 3.

The starting point for the design of the evolved radiative element is a classical patch antenna placed on a 250 μm -thick PEN substrate working at 6 GHz with a footprint of 17 x 14 mm^2 (i.e. electrical length equals $0.34 \lambda \times 0.28 \lambda$), sketched in Figure 3.4; the corresponding bandwidth is 50 MHz and the realized gain at the resonant frequency is equals 5.8 dBi.

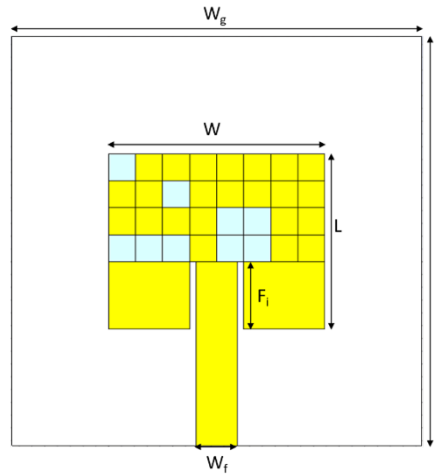


Figure 3.4: Top-view of the evolved patch antenna

The geometrical parameters used for the simulations are listed in Table 3.1; the dielectric substrate has been considered loss free for this purpose.

Table 3.1: Geometrical parameter of the considered patch antenna

Parameter	Value [mm]
W	16.88
L	13.77
F_i	5.26
W_f	3.19
W_g	32
L_g	32

All the steps previously described and represented in Figure 3.2 for a general Genetic Algorithm, are now detailed for our application.

1. Encoding: the patch antenna is subdivided into 32 pixels with a square form of 2 μm ; each of them represents a gene and assumes a value equal to 1 if the pixel is made of metal (yellow) or 0 if it is made of vacuum, as reported in Figure 3.4.
2. Initialization: members of the population are randomly generated. It is very important to fix the number of the population according to the field of the application of the GA: if the number of the population is high, the result is very precise with the drawbacks of a higher computational time. On the other side, when a small population is considered, the process is almost fast but a stack in the local minima can occur. In this case, the radiating area must be big enough to guarantee optimal radiation properties, so at least 60% of the gene has to be made of metal.
3. Evaluation of the population: the value of the fitness function $C(f_R)$, expressed in Equation 3.1, is evaluated for each device.

$$C(f_R) = \begin{cases} |50 - \text{Re}\{Z(f_R)\}|e^{\frac{f_R - f_c}{f_c}}, & f_c - \delta < f_R < f_c + \delta \\ 1000, & \text{otherwise} \end{cases} \quad (3.1)$$

In particular, the resonant frequency (f_R) and the value of the impedance ($Z(f_R)$) at the resonant frequency is estimated by means of a finite difference time domain (FDTD) solver. The objective frequency equals 4 GHz and is expressed as f_c . The term Δ is used to take into account the tolerance to the resonant frequency. All the combinations of the gene which compose antennas having the real part of the impedance that is far from 50 Ω are discarded.

4. Chromosomes rank and selection process: the chromosomes mate following a “roulette selection process” [80]. Each element has an associated probability of selection, π_i which follows a Boltzmann distribution,

as in Equation 3.2:

$$\pi_i = e^{-\beta c_i} \quad (3.2)$$

C_i is the value of the cost function of the i -th element of the population and β is a normalization factor equal to

$$\beta = \frac{1}{N} \sum_{i=1}^N c_i \quad (3.3)$$

5. Crossover: the couples associated in the previous step generate new offspring by a single-point crossover.
6. Mutation: a random variable is applied to a single gene on an element of the population with a probability equal to 1%.
7. Reordering: as in step 3, the fitness function is evaluated for each device of the new population. Then, elements are rearranged in ascendent order for the value of their fitness function: the ones characterized by a high-cost function are discarded.
8. Loop statement: The value of the cost function of the elements is compared with the threshold value of the algorithm: if the convergence is reached the process is completed, otherwise it restarts from step 3.

In this application, the algorithm converged after 12 iterations. The result is an evolved patch antenna with a footprint of $14 \times 17 \text{ mm}^2$ that resonates at 4 GHz with an S_{11} dip equal to -24.47 dB and a bandwidth of 14 MHz. the realized gain of the device at the resonant frequency is equal to -0.647 dBi.

3.3 Metamaterials: Split Ring Resonator

One of the drawbacks of the miniaturization step is a degradation of the radiation properties of the antenna. To improve this aspect a μ -negative split ring resonator is added between the top and ground plane. In detail, the geometry is a square split ring resonator (Figure 3.5 a)) composed of

two concentric split rings with the aperture placed in opposite directions and separated by a gap. The SRR can be treated as an LC circuit [81] as reported in Figure 3.5 b).

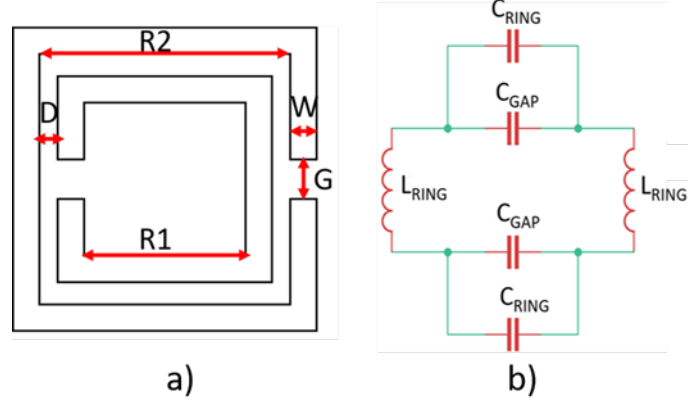


Figure 3.5: a) Geometry and b) equivalent circuit, of the SRR

The value of the inductance L_{RING} of each ring can be expressed as in Equation (3.4):

$$L_{RING} = \frac{\mu_0 D}{W} [R2 + R1] \quad (3.4)$$

where D represents the gap between two rings, W is the ring thickness, and $R2$ and $R1$ are the outer and inner radii of the rings, respectively. As regards the capacitance, C_{RING} represents the capacitance of the single ring while C_{GAP} the capacitance between the rings, respectively. C_{RING} can be defined as in the following expression, Equation (3.5)

$$C_{RING} = \frac{\epsilon_0 \epsilon_r t W}{G} \quad (3.5)$$

where t is the thickness of the ring and G is the aperture of the ring. Finally, C_{GAP} can be expressed as in Equation (3.6):

$$C_{GAP} = \frac{A \epsilon_0 \epsilon_r W (2R2 + 2R1 - G)}{2D} \quad (3.6)$$

A is an equilibrium constant. By considering the geometrical parameters of the SRR, the resonant frequency f_0 can be evaluated as in Equation (3.7):

$$f_0 = \frac{1}{2\pi\sqrt{L_{RING}(C_{RING} + C_{GAP})}} \approx \frac{1}{2\pi\sqrt{L_{RING}C_{RING}}} \quad (3.7)$$

In this thesis, the geometry of the square split ring resonator has been properly designed to increase the gain at the working frequency of the antenna. The geometrical dimensions of the square SRR are listed in Table 3.2.

Table 3.2: Geometrical parameters of the square SRR

Parameter	Value[mm]
R1	4.5
R2	3
W	1
D	0.5

The results of the simulations of the multilayer antenna are shown in Figure 3.6.

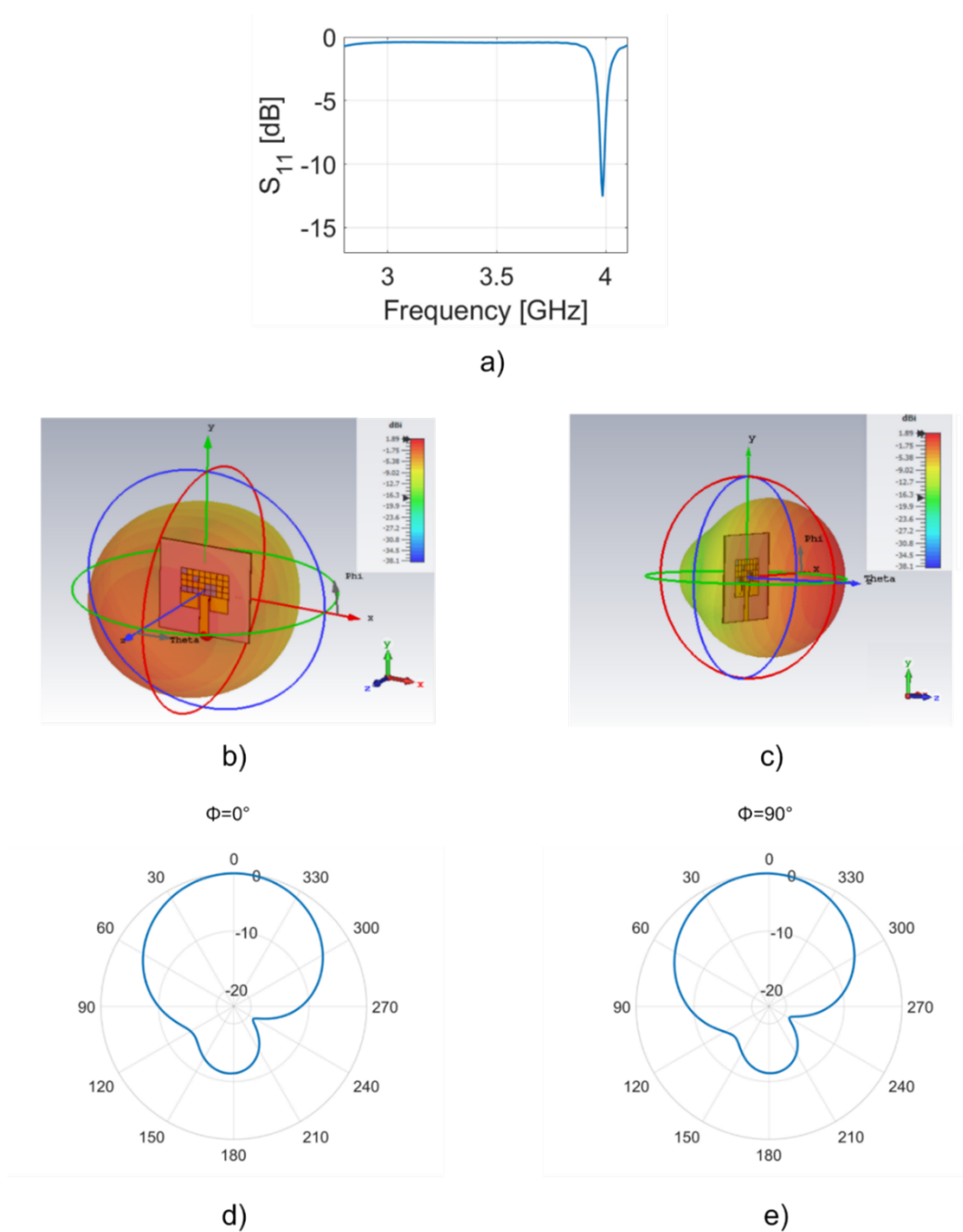


Figure 3.6: a) Simulated scattering parameter S_{11} of the multilayer antenna, b) front perspective and c) side perspective of 3D radiation patterns at 3.985 GHz; simulated polar plot for the plane d) $\phi=0^\circ$ and e) $\phi=90^\circ$.

In Figure 3.6 a) the trend of the scattering parameter S_{11} is shown; there

is a dip of -14.2 dB at 4 GHz with a bandwidth of about 15 MHz. For a different application, it is possible to increase the bandwidth of the device by considering as a starting point a circular patch antenna [82]. In Figures 3.6 b) and c) two different perspectives of the 3D realized gain of the patch antenna at the resonant frequency are reported; the corresponding maximum value is equal to 1.89 dBi. In Figures 3.6 d), e) the radiation pattern in the E-plane and H-plane are reported, respectively. In particular, the E-plane ($\phi=0^\circ$) presents a magnitude of the main lobe equal to 1.89 dBi, with a direction of 3.0 deg, and an angular width (3 dB) of 93.2° . Whereas, in the H-plane ($\phi=90^\circ$), the main lobe magnitude is equal to 1.88 dBi and the main lobe direction is equal to 0 deg with an angular width (3 dB) equal to 92° . The results of the miniaturization process have been summarized in Table 3.3.

Table 3.3: Comparison between a classical and the evolved patch antenna

	Classical Patch Antenna	Evolved Patch Antenna
Working Frequency	6 GHz	3.96 GHz
Electrical Length	$0.34\lambda \times 0.28\lambda$	$0.22\lambda \times 0.18\lambda$
Bandwidth	50 MHz	15 MHz
Gain	5.8 dBi	1.89 dBi
Physical Dimensions	$17 \times 14 \text{ mm}^2$	$17 \times 14 \text{ mm}^2$

If the simulations with and without the integration of the SRR are compared, an increase of 1.24 dBi of the gain without increasing the footprint of the device can be observed. The final device is an evolved patch antenna with a footprint of $14 \times 17 \text{ mm}^2$ resonating at 4 GHz: in comparison with a classical patch antenna working at 6 GHz, we obtain a size reduction of the 60%. Although the device presents a degradation of gain and efficiency due to the minimization of the antenna, the simulated values suggest its use for

wireless communications.

3.4 SAR simulations

In the field of wearable devices, an important parameter to be evaluated is the Specific Absorption Ratio (SAR), which represents the power absorbed by the human body. The maximum accepted value for this parameter is fixed equal to 2 W/Kg for 10 g of tissue in Europe [75]. A model representing a schematic body phantom has been realized in CST Microwave Studio to estimate this parameter. In [83] it has been demonstrated that by using a complex structure for the body, the simulation results are not improved. For this reason, the simplified phantom (Figure 3.7) is composed of different layers: bone, muscle, fat, and skin, having the thicknesses reported in [84].

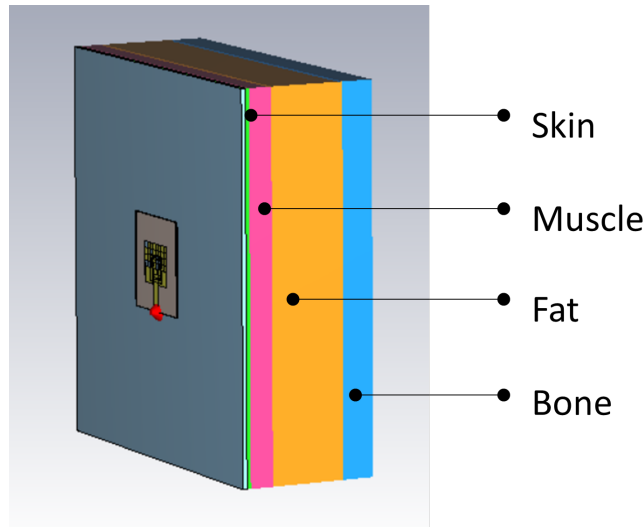


Figure 3.7: Sketch of the multilayer phantom

For each material is necessary to specify the permittivity, the conductivity, and the density. The properties and thicknesses of each layer are reported in Table 3.4. The result of this analysis shows that the SAR value in 10g of the tissue at the resonant frequency of 4 GHz is equal to 0.06 W/Kg by considering a stimulus power of 0.5 W (default value of the software), indeed the absorption of the body is below the limit. In particular, SAR value re-

Table 3.4: Property of tissues composing the phantom

Layer	Thickness [mm]	Permittivity	Conductivity [S/m]	Density [Kg/m^3]
Skin	1.5	38.1	1.44	1020
Fat	8.5	5.29	0.102	900
Muscle	27.5	52.8	1.71	1041
Bone	11.5	11.4	0.385	1850

sults linearly dependent to the variation of fat layer: by considering different thicknesses in the range [7.5:1:9.5] mm, the SAR is equal to 0.058 W/Kg, 0.06 W/Kg and 0.063 W/Kg, respectively. This is due to the high percentage of the water in fat tissues.

3.5 Antenna fabrication

The evolved patch antenna has been fabricated by means of the NanoDimension's Dragonfly LDM multi-material 3D printer (Figure 3.8 a)).

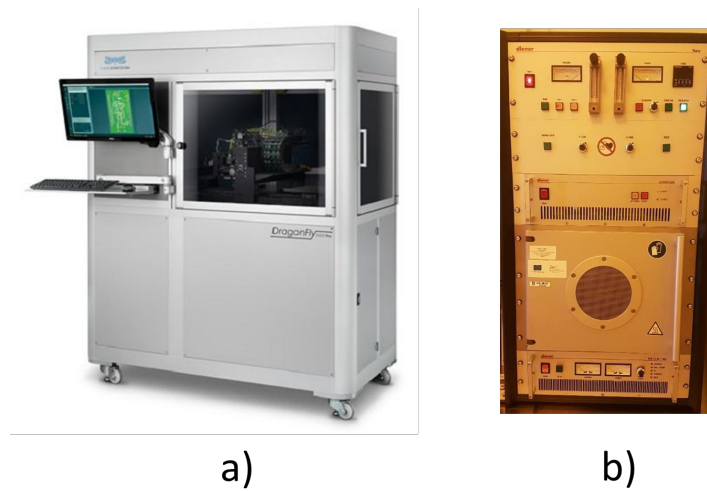


Figure 3.8: Antenna fabrication: a) multi-material 3D printer NanoDimension's Dragonfly LDM, b) Plasma Oxygen Diener Nano Version

It is a very powerful and innovative machine that allows the printing of both metallic and dielectric layers with high precision. For our purpose, only the conductive layer has been used and printed directly on the PEN substrate. The samples have been subjected to a preliminary Oxygen (O_2) plasma treatment. Oxygen is the most commonly used gas in plasma treatment due to its wide availability and low costs. The aim of the plasma-oxygen is the cleaning of the surface of samples made of plastic or glass. The treatment can be done in combination with other gases. As an example, oxygen is used together with Argon (Ar) for cleaning metal surfaces. In this case, the role of the O_2 /Ar-plasma is to strip the oxygen molecules away from the metal to prevent its oxidation. There exists a fundamental difference between argon and oxygen: the first does not cause surface modifications as oxygen, which in turn can also perform etching. This suggests an interesting application as the etching of the PEN surface increases the rugosity of the samples together with the wettability. The system used for this step is the Diener Nano Version (Figure 3.8 b)). The PEN samples have been treated for 15 minutes with a oxygen plasma generated using a power of 150 W. After this step, the printing process has been performed. In Figure 3.9 the fabrication steps are detailed. The first step of this process is the import of

the 2D Gerber file containing the geometry of the device converted by the printer in layer-by-layer instructions. The Ag-based ink is deposited through hundreds of nozzles present on the printing head patterning the geometry of the antennas. The ink curing and sintering have been carried out at a temperature of 140°C.

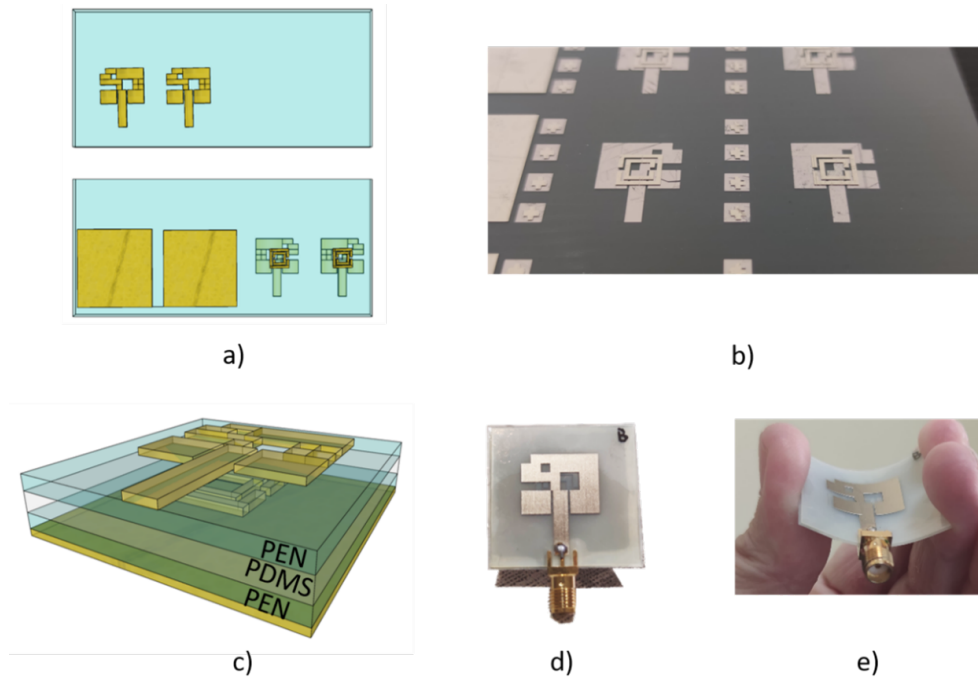


Figure 3.9: a) Steps of the 3D printing process, b) result of the alignment between patch and SRR and printed ground planes, c) representation of the multilayer antenna with the interlayer of PDMS, d) flat and e) bent fabricated prototype with SMA connector

The first printed layer is the radiative part of the evolved patch. Markers are patterned on the substrate to correct the alignment on the X and Y axis of the structure. Then, the substrate is flipped, the printing position is corrected and then the process goes on with the printing of both SRR, and the ground plane next to it (Figure 3.8 a)). All these radiating elements are printed with a thickness of 35 μm in order to guarantee optimal conductivity (the declared minimum thickness to obtain good conductivity is 17 μm). In Figure 3.8 b), the result of the alignment step on the PEN substrate is shown.

After the printing, the layer containing the patch together with the SRR and one containing the ground plane is cut by means of a laser-cutter (Universal Laser System vls2.30). A laser cutter is an economical and compact platform characterized by a working area of 12.585 cm^3 and a CO_2 laser of $10.6 \mu\text{m}$. Different parameters have to be fixed before the cut: the power of the laser (in the range of 10-30W), the velocity of the tip, the distance between the tip and the sample, and the Pulse Per Inch (PPI), driving the precision of the cut. The two layers are bonded together by means of an adhesive interlayer made of Polydimethylsiloxane PDMS (Sylgard 184, Dowsil), widely used silicon for flexible and biocompatible devices, very easy to prepare. It is worth stressing that the choice of this elastomer does not affect the flexibility of the antenna. The PDMS is mixed in a ratio of 1:10 with its curing agent. Then is spin-coated on one of the dielectric surfaces at 3500 rpm for 60" and cured at 90°C for 15 minutes on a hot plate with the second dielectric layer on it. The entire stack is schematized in figure 3.8 c). Finally, Figure 3.8 d) and e) report the fabricated prototype in flat and bend conditions, respectively.

3.6 Characterization

The device has been characterized in terms of the scattering parameter S_{11} , using a VNA Anritsu MS46122B, 3D radiation pattern, and polar plots. The results are shown in Figure 3.10.

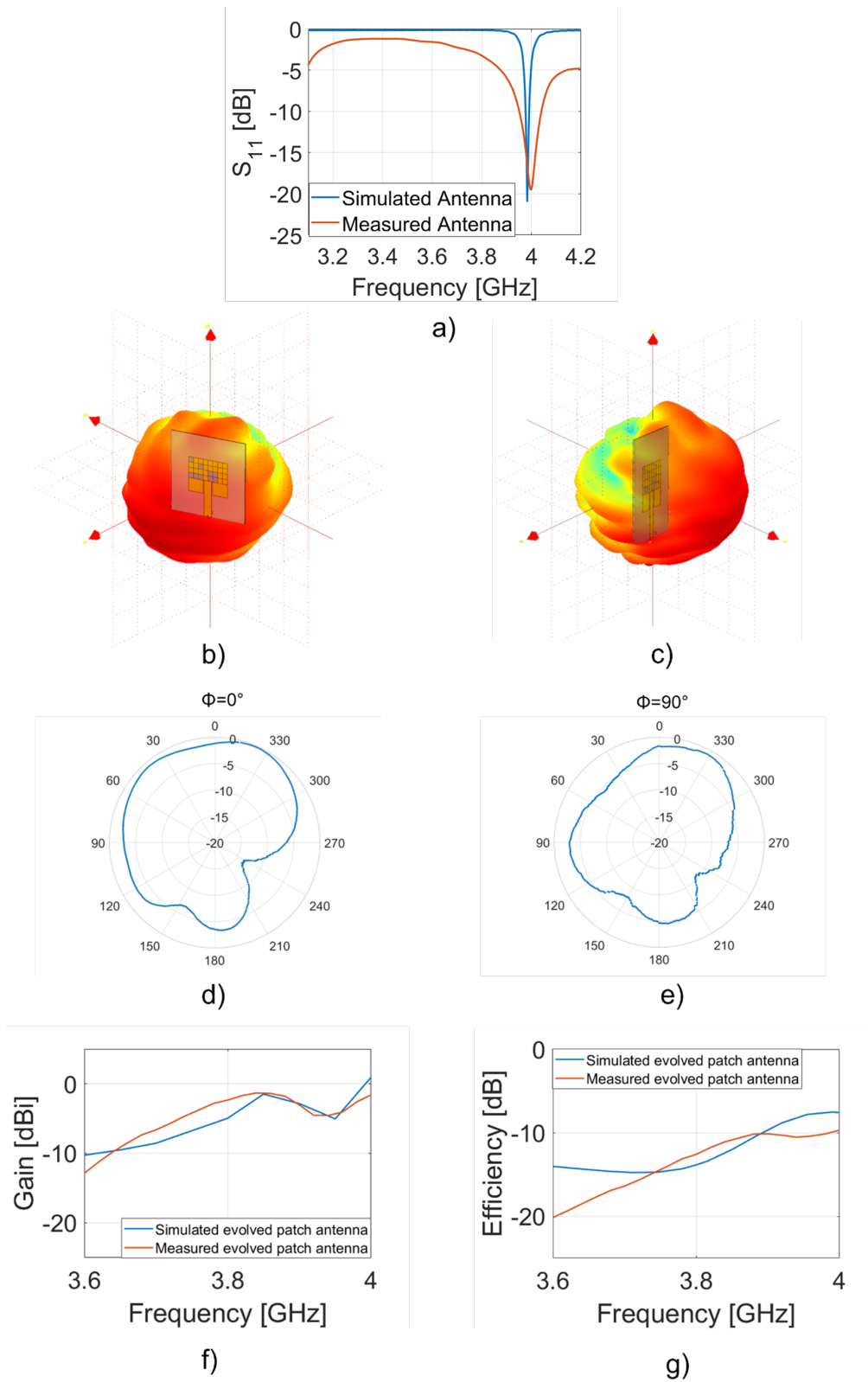


Figure 3.10: a) Simulated (blue curve) and measured (red curve) scattering parameter S_{11} of the multilayer antenna, measured b) front perspective and c) side perspective 3D radiation patterns; polar plot at d) $\phi=0^\circ$ and e) $\phi=90^\circ$ at 4 GHz; simulated (blue curve) and measured (red curve) f) gain and g) efficiency of the evolved patch antenna

Figure 3.10 a) shows a comparison between the trends of the simulated (blue curve) and the measured (red curve) scattering parameter S_{11} . In particular, it is possible to see a dip of -14.2 dB at 3.984 GHz and a dip of -13.41 dB at 3.962 GHz for the simulated and the measured evolved patch antenna, respectively. There is a shift of a few MHz between simulations and measurements which is due to the SMA connector. Indeed, the presence of a coaxial connector causes the presence of a static capacitance, so it increases the electrical length of the device [85]. The 3D radiation patterns are reported in Figures 3.10 b) and 3.10 c). The measurements are performed by means of an anechoic chamber (StarLab from Satimo), working in a frequency range between 800 MHz and 18 GHz. The working principle of the chamber exploits Huygen's principle, thanks to which it is possible to reconstruct the far field (FF) starting from the indirect measurements of the near field (NF). It is possible to see a very good agreement with the simulated ones shown in Figures 3.6 b) and 3.6 c). At the resonant frequency of about 4 GHz, the simulated realized gain is equal to -0.8 dBi by considering also the losses of the dielectric substrate, while the measured one is equal to -1.5 dBi. Measured 2D polar plots for E-plane ($\phi=0^\circ$) and H-plane ($\phi=90^\circ$) are presented in Figure 3.10 d) and e): for both planes, there is a good agreement between simulations and measurements (Figures 3.6 d) and e)). Figure 3.10 f) reports the comparison between the trend of the simulated (blue curve) and measured (red curve) gain near to the resonant frequency; also, in this case, the experimental results follow the numerical ones. Finally, in Figure 3.10 g), the trend of the efficiency is shown: the simulated value (blue curve) is higher than the measured one (red curve) at 4 GHz. This phenomenon may be caused by different factors: the soldering of the SMA connector, the presence of the solvent mixed with Ag-based ink used during the printing process of the radiating elements, and the losses of the PEN substrate that are reported in the datasheet until the frequency equal to 1 GHz.

3.7 Bending Analysis

Since the final goal is to put this device on the body (in particular, on an ankle) for health monitoring, further analysis has been performed to characterize the S_{11} trend of the device under bending conditions. More in detail, two different bending radii are considered: $R=5$ cm and $R=7$ cm. The comparison has been performed by considering a cylinder made of air for the numerical analysis and a cylinder made of Polystyrene for the experimental one. It is worth stressing that this material is transparent to microwave radiation. The results are reported in Figure 3.11 a)-c). As it is possible to see, there is a very good agreement between simulations and measurements. For the radius $R=5$ cm, there is a shift to a lower frequency for both (3.8 GHz for the simulations versus 3.9 GHz for the measurements). For $R=7$ cm, the resonant frequency is the same as the flat one for both curves.

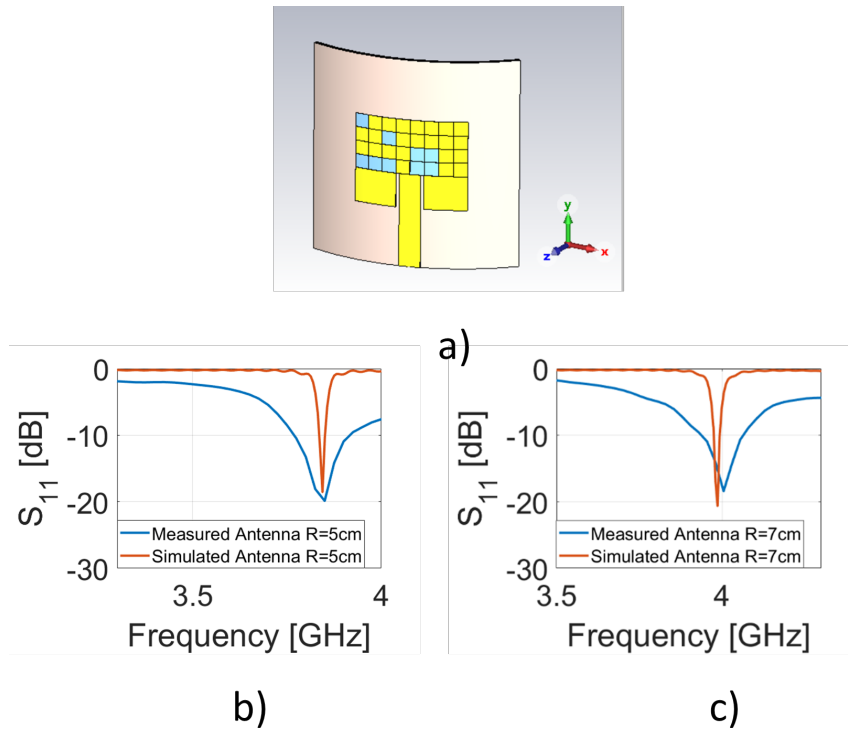


Figure 3.11: Bending analysis: a) device bent on the software, comparison between measured (blue curve) and simulated (red curve) scattering parameter S_{11} for a bending radius of b) 5 cm and c) 7 cm

Chapter 4

Planar Inverted-F Antenna on flexible substrates

Planar Inverted-F antennas (PIFAs) are very popular in daily technology such as smartphones. The geometry of a PIFA is very straightforward as is formed by a monopole shorted with the ground plane. The radiation pattern is omnidirectional, and the footprint is very lightweight and compact, as the presence of the shorting-pin decreases the dimensions of the antenna. The feed is placed between the transmission line and the shortcuted end. Varying the position of the feeding, impedance can be adapted without the use of external components. From a microwave point of view, the shorting pin acts as a parallel inductance, indeed the nearer the feeding is to the shorting pin, the higher the impedance of the antenna [86]. Another interesting property of PIFAs is the planar geometry which allows rapid and low costs fabrications. In this scenario, the integration of PIFA on flexible substrates can be very interesting combining their interesting peculiarities with bendability and wearability [87–89]. In this chapter, the design and fabrication of PIFAs on flexible substrates have been detailed. In particular, two generations of PIFAs are developed: the first one is based on a PEN material, while the second is on a flexible glass substrate. It is worth stressing that these materials have never been used for the fabrication of PIFAs. A first generation of antennas is printed using a 3D multi-material ink-jet printer based on sil-

ver nanoparticles. After the printing, the antenna connectors are mounted using two different approaches. The first is based on a z-tape conductive adhesive and a flip-chip machine to place the connector with very high precision. The second is performed by soldering the connector directly on the metallic pads of the antennas. A second generation, based on flexible glasses, allows the fabrication of antennas on a totally transparent substrate which further reduces the visive impact of the device. Also in this case the antennas are fabricated with the multi-material 3D printer. The fabrication protocol was optimized for this new substrate: in particular, the glasses are treated with plasma oxygen to clean all the organic compounds. The effectiveness of the approach was tested using an Atomic Force Microscope (AFM). Besides the printing process, the cutting of the antennas is optimized by developing an innovative procedure involving a laser cutter and a marker. The use of this approach allows the cutting of antennas without the formation of any cracks and with a percentage of success of 99%. All the fabricated antennas are characterized in terms of the scattering parameter S_{11} . This chapter demonstrates that PIFA geometry is an optimal choice for rapid prototyping antennas on heterogeneous kinds of flexible substrates.

4.1 Design and simulations

The sketch of the proposed antenna is shown in Figure 4.1, in which the red portion represents the antenna and the ground, while the light blue section is the substrate. All the optimized geometrical parameters are listed in Table 4.1.

Table 4.1: - List of the geometrical parameters

Parameter	Value[mm]
W1	6
W2	2
W3	4.5
W4	4
W5	8
H1	9
H2	11
H3	1.5
H4	1.5
H5	2.5
H6	3
H7	6

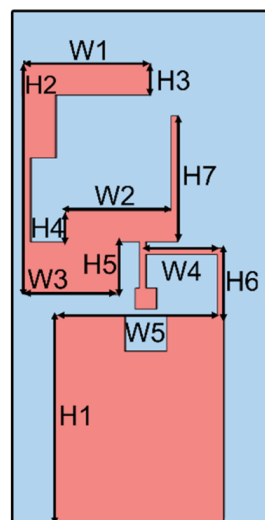


Figure 4.1: Sketch of the PIFA

The antenna is placed on a PEN substrate with a thickness of $250 \mu\text{m}$, a relative dielectric permittivity (ϵ) of 2.9 and a loss tangent of 0.005. It is a compact, flexible, and is dual-band device, resonating at 3.8 GHz and 6.1 GHz. Both of these frequencies are in the sub-6GHz band of the 5G spectrum and are licensed in Europe (3.8 GHz) and USA (6.1 GHz). The PIFA configuration is composed of two different L-shaped regions: $W1 \times H1$ is responsible for the impedance matching at the lower frequency, 3.8 GHz, while $W2 \times H2$ is used for achieving the impedance matching at the higher one, 6.1 GHz. The intermediate part of the antenna is used as a feeding point for placing the U.FL connector. The total footprint of the device is $10 \times 24 \text{ mm}^2$. The PIFA structure is very sensitive to geometrical variations; the slightest modification could cause impedance mismatching and variation in the resonant frequency. To achieve a good impedance matching at the two resonant frequencies, some parametrical sweeps have been performed. For example, the trend of the scattering parameter S_{11} by varying $H2$ and $H7$ has been reported in Figure 4.2.

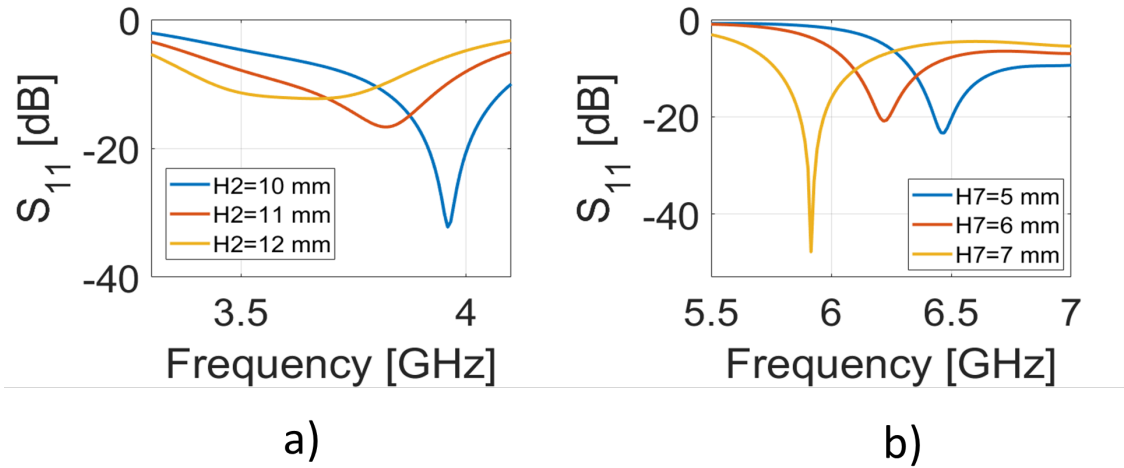


Figure 4.2: Effects of PIFA's parameters on return loss at a) around 3.81 GHz and b) 6.22 GHz

From Figure 4.2 a) it is possible to note that the resonant frequency decreases by increasing the value of $H2$ parameter. The optimal value is $H2=11\text{mm}$ since the resonance is in the band of interest (3.6 - 3.8 GHz). As

regards the parameter H7, in Figure 4.2 b), the S_{11} dip moves to a lower frequency when the value of H7 increases. To have the S_{11} in the band of interest, the parameter is fixed equal to 6 mm. It is worth stressing that H2 does not cause any variation in the higher band of the antenna; vice versa variations on H7 are not related to the resonance at the lower frequency. Furthermore, the other two fundamental parameters (W1 and W7) present the same behavior of H2 and H7; for this reason, the results are not reported. In Figure 4.3, the simulation results of the optimized antenna are exploited.

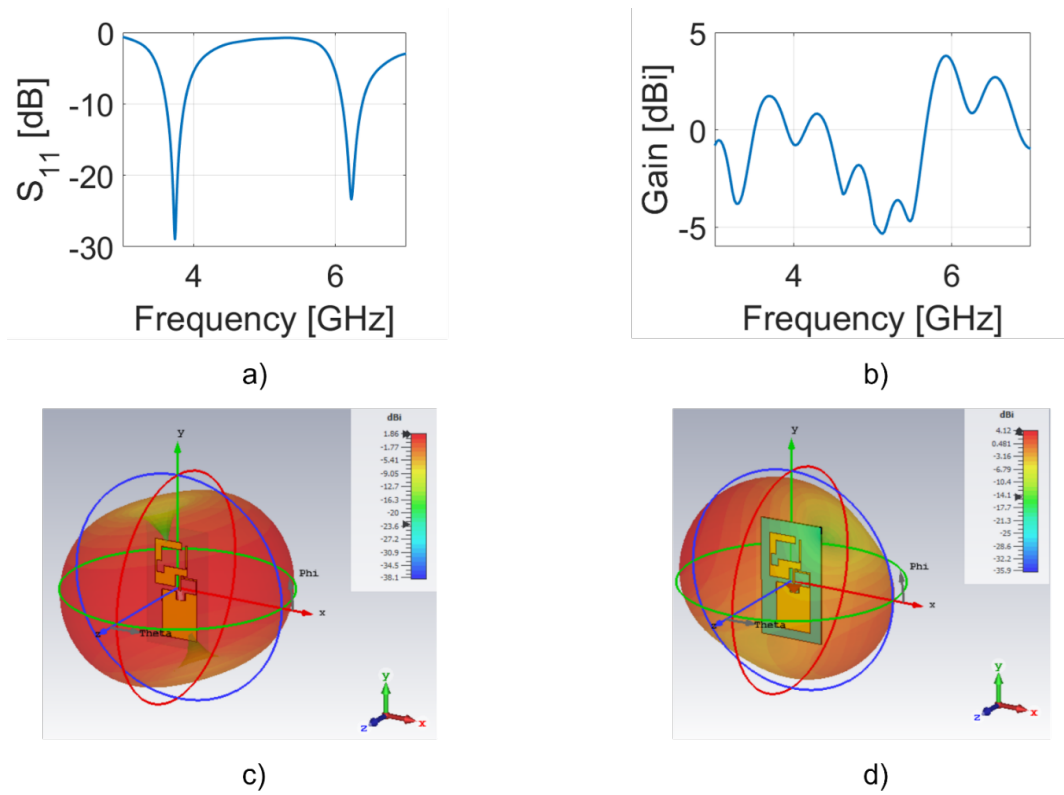


Figure 4.3: Simulated a) scattering parameter S_{11} , b) gain of the PIFA antenna, 3D radiation pattern at c) 3.8 GHz d) 6.1 GHz

In figure 4.3 a) the trend of the scattering parameter S_{11} is reported. There are two dips corresponding to the two resonant frequencies: -29 dB with a bandwidth of 270 MHz at 3.8 GHz; -18 dB at 6.1 GHz which corresponds to a bandwidth of 208 MHz. In figure 4.3 c) and d) the 3D radiation patterns for realized gain at two resonant frequencies are shown. The max-

imum value is equal to 1.86 dBi at 3.8 GHz and 4.12 dBi at 6.1 GHz. The simulated SAR is equal to 0.26 W/kg.

4.2 Fabrication and characterization on PEN

The device has been fabricated directly on the PEN substrate employing a multi-material 3D printer, NanoDimension's DragonFly LDMTM System, after a preliminary Plasma Oxygen treatment as explained in Section 3.5. The 2D PIFA sketch is provided as input to the printer and because of its parallel processing characteristic, this technique shows a high process yield. In this case, approximately 40 μm of metal have been deposited and a total of about 50 antennas are completed in a couple of hours on a printing area of about 18x18 cm^2 . An array of 3x3 fabricated antennas and some prototypes are shown in Figure 4.4. It is possible to note that some grid lines of a few micrometers thickness have been printed to cut the devices with the laser cutter, in a fast and precise way.

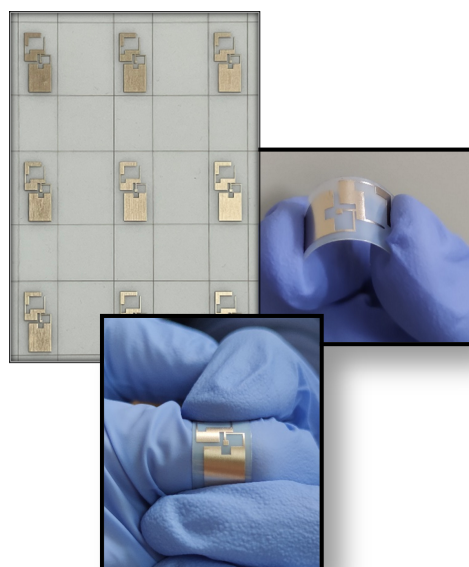


Figure 4.4: Fabricated prototypes

In the middle part of the PIFA, the U.FL connector has been placed for

performing the characterization step. As a first trial, we decide to use an ad-hoc small board realized with Dragonfly printer, composed of a $200\ \mu\text{m}$ -thick dielectric layer and a $30\ \mu\text{m}$ thick metal layer which represent the U.FL pads. The connector is sold on it and then attached to the antenna by using a z-conductive tape (3M 9703). For placing it in a very precise way, a Flip chip machine has been used (Figure 4.5).

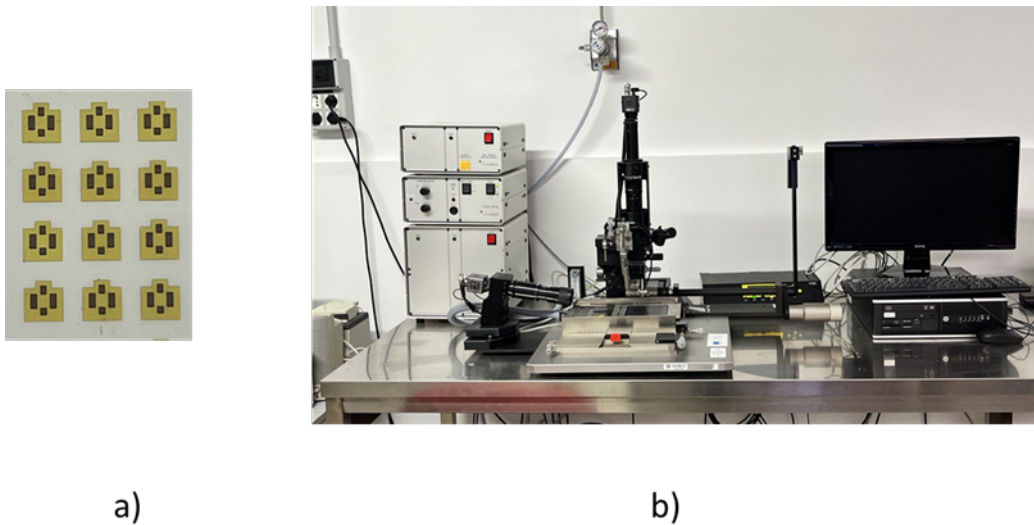


Figure 4.5: a) Small board and b) Flip-chip machine, used for the positioning of the connector

The flip chip is a powerful instrument to place components on boards with very high precision. The machine is formed of a bonding head holding the connector, and a bonding stage on which the antenna is vacuum-fixed. The bonding stage can be aligned with the connector by micrometric screws and a two-sight camera. After the alignment, the bonding head rotates the connector placing its bottom surface on the substrate. The temperature of the bonding stage and the force applied from the bounding head are computer controlled. In this case, the connector is pressed on the substrate with a force of $20\ \text{N}$ at room temperature for 30 minutes. The prototypes realized with this approach are characterized in terms of the scattering parameter S_{11} and the results are shown in Figure 4.6.

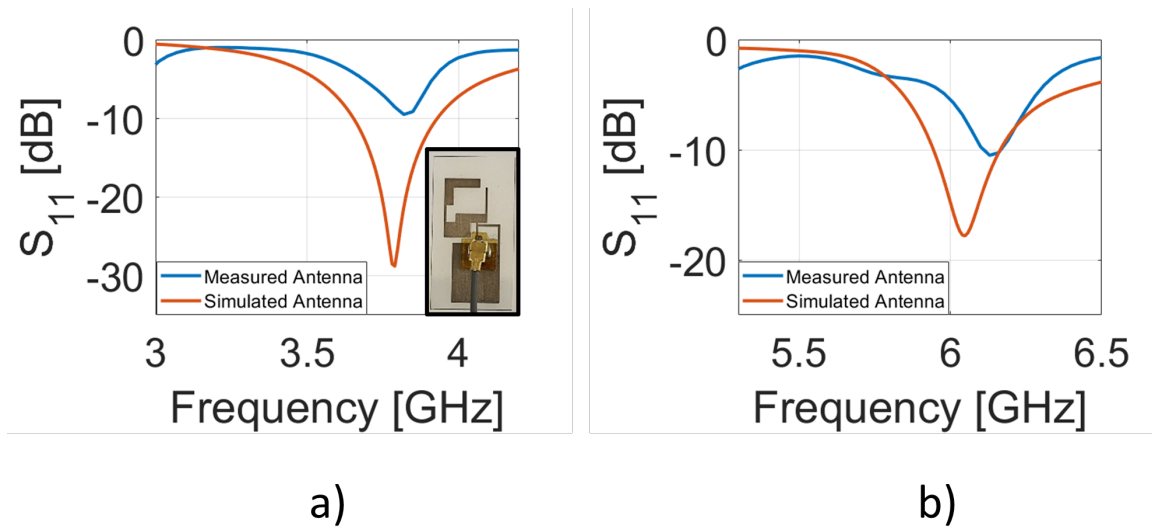


Figure 4.6: Comparison between measured (blue curve) and simulated (red) curves PIFA at a) 3.8 GHz and b) 6.1 GHz

As it is possible to see, the impedance is not perfectly matched for both frequencies; in addition, for the second band, there is a shift to a higher frequency. This happens because the z-conductive tape presents only some spot of conductive ink and this is not enough to guarantee optimal adhesion and conductivity with the metal device. It is possible to conclude that even if this approach is very precise and allows avoiding the use of the soldering directly on the substrate which could be damaged, it does not guarantee optimal results in terms of impedance matching. The second approach that we used is the soldering of the U.FL connector directly on the device. The results of this procedure and the characterization step have been reported in Figure 4.7 a) and b), respectively.

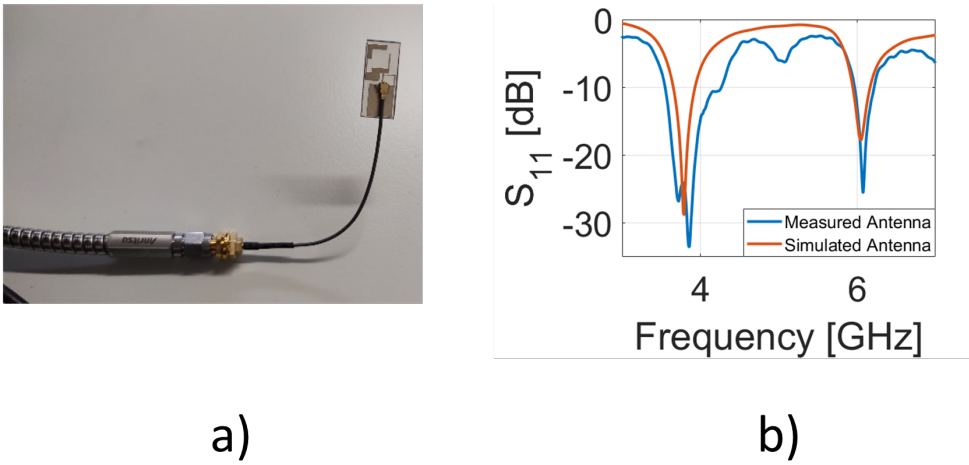


Figure 4.7: a) Fabricated prototypes and b) results of the characterization step

The fabricated PIFA (red curve) resonates a 3.86 GHz with a bandwidth of 700 MHz. It is larger than the simulated one (blue curve) due to the electromagnetic losses introduced by soldering the connector and by the presence of an amount of solvent mixed with the conductive ink. As regards the second resonance, at 6.1 GHz, there is a good agreement between simulations (red curve) and measurements (blue curve) also in terms of bandwidth, which is equal to 240 MHz. The measured gain is equal to 0.9 dBi and 1.1 dBi for 3.8 GHz and 6.1 GHz, respectively. For the lower frequency, the obtained value is very close to the simulated one; while for the higher frequency, the value is lower than the simulated one. This is probably due to some artifacts of the exploited set-up (see Section 2.4) and the presence of the RF cable on the radiating part of the antenna, reducing its radiation efficiency.

4.3 Fabrication and characterization on flexible glasses

The same device, described in detail in the previous section, has been realized on another flexible substrate: 100 μm and 200 μm -thick Corning Willow® Glass. The bending radius of these glasses is equal to 10 cm and 20 cm,

respectively. They present a high resistance to the temperature, until 600°C . The relative dielectric constant is 4.09 at 963 MHz (from the datasheet) and the corresponding value of loss tangent is equal to 0.0002. Since this material has never been used for the fabrication of antennas with NanoDimension's Dragonfly LDM multi-material 3D printer, as a first attempt we printed the device directly on the substrate. After this process, the fabricated device presents an issue: metal delamination, as shown in Figure 4.8.

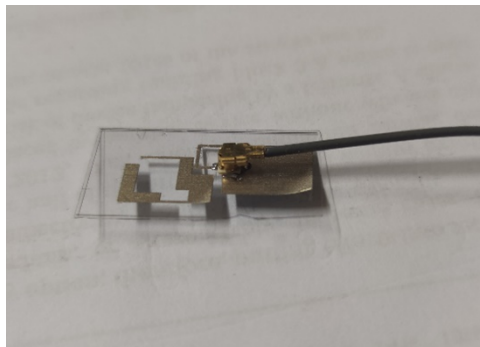


Figure 4.8: Metal delamination of the device after the printing process

The prototype shown above is placed on $200\ \mu\text{m}$ -thick Corning willow glass; the result is the same also for the thinner one. To better understand the reason behind this phenomenon, some Plasma Oxygen treatment has been performed. All the following analyses are performed on the glass with a thickness of $200\ \mu\text{m}$. Different configurations of power for different times have been used, as listed in Table 4.2.

The four configurations have been analyzed using Atomic Force Microscopy (AFM), sketched in Figure 4.9.

Table 4.2: Different configurations of Plasma Oxygen treatment

Configuration	Power [W]	Time [min]	Oxygen flow [sccm]
1	150	15	25
2	150	30	25
3	300	15	25
4	300	30	25

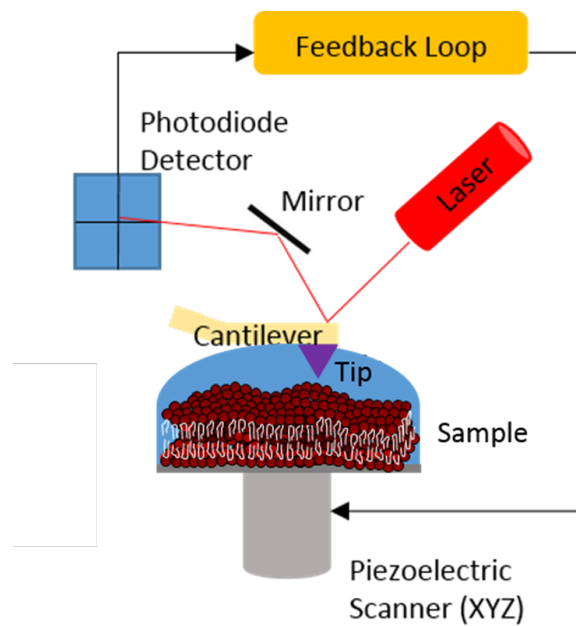


Figure 4.9: Sketch of the AFM

There is a laser that points at a cantilever. The reflected beam is collected by a four-quadrant photodiode. At the end of the cantilever, there is a non-conductive tip that contacts the samples. The sample is moved in 2D by a Piezo stage. Finally, there is a data acquisition control unit that drives the scanner, measures the data and converts them to an image. As a non-

conductive tip, a silicon tip FORT (AppNano) with a length of $225 \mu\text{m}$ has been used. There are two working modes: tapping mode or in contact mode. During the first one, the tip vibrates at its natural resonance, and, during the scanning of the surface and the proximity of the surface, the presence of the atoms shifts the frequency. The instrument registers this shift and modifies the z-position of the tip with respect to the sample and the original frequency is restored. In a loop, the instruments register the changes in z due to the morphology of the sample and reconstruct the topography of the surface analyzed. The second mode is performed by placing the tip constantly in contact with the samples and is based on the constant repulsion between the tip and the surface's atoms. This modality is easier than the first one, but the hard silicon tip risks to damage delicate samples [90]. In the case of antennas, since glass is not soft material, the contact mode has been used. The results of this analysis are reported in Figure 4.10 a)-e).

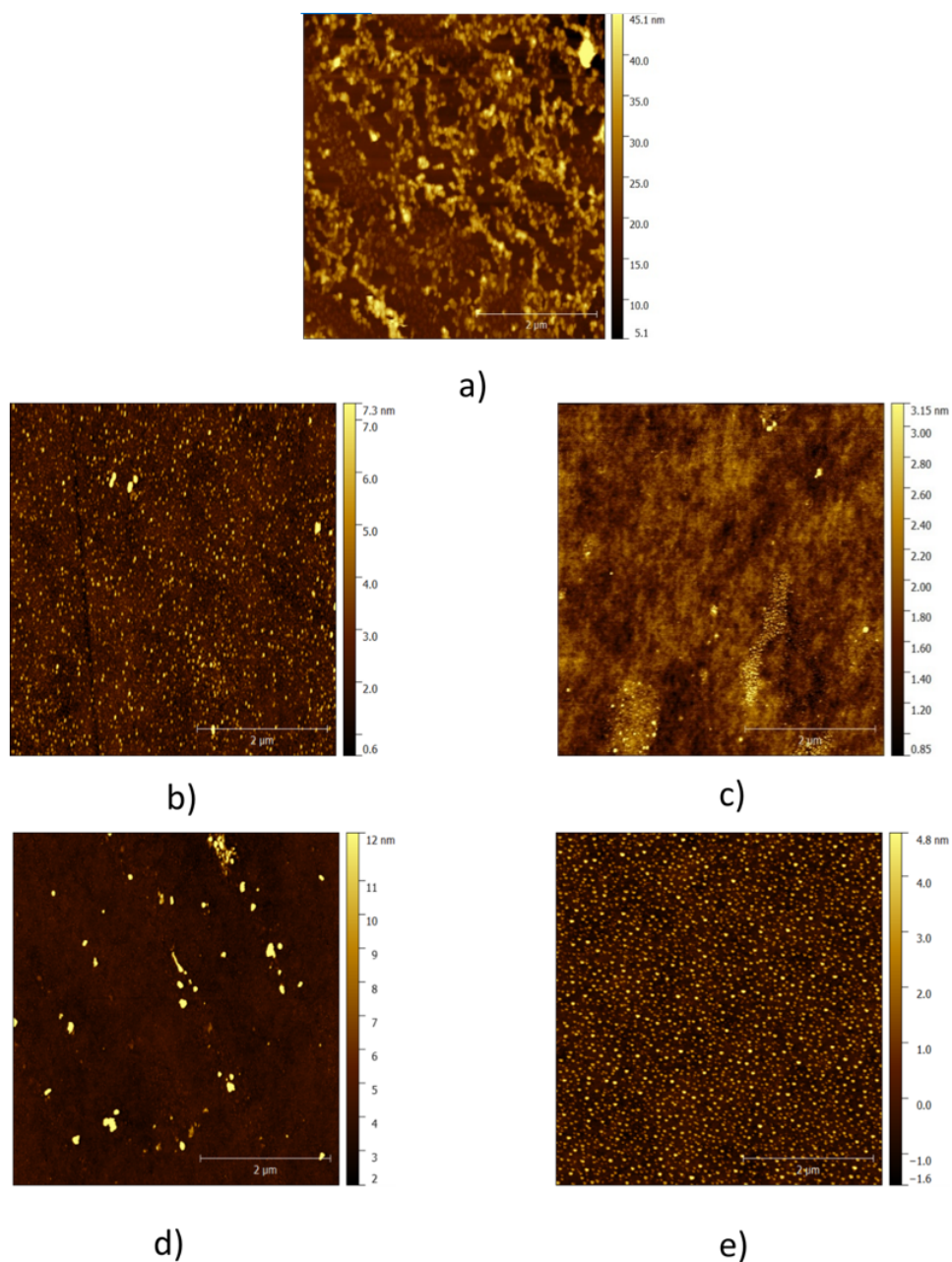


Figure 4.10: AFM analysis: a) substrate without any treatment and results after Plasma Oxygen treatment for b) configuration 1, c) configuration 2, d) configuration 3) and d) configuration 4

Analyzing the data, it results that by increasing the duration of the Plasma Oxygen treatment, the value of the roughness decreases. In fact,

on the sample without any Plasma Oxygen treatment (Figure 4.9 a)), the roughness is equal to 6.43 nm. With treatment at 150 W, it becomes equal to 0.958 nm after 15 minutes (Figure 4.9 b)) and 0.3 nm after one hour (Figure 4.9 c)). If we consider treatment at 300W, the roughness is equal to 1.74 nm after 15 minutes (Figure 4.9 d)) and 1.065 nm after one hour (Figure 4.9 e)). After this analysis, it results that the problem of delamination was due to organic residuals on the surface of the glass. To find a compromise between the goodness of the results and the velocity of the entire fabrication process, a treatment of 15 minutes at 150 W has been performed for improving the fabrication protocol. In addition, from Figure 4.8 it is possible to see that the edges of the antenna are not very precise; this is due to the use of a diamond tool for cutting the device from the glass sheet. To improve this aspect, we developed a protocol for cutting the device by using the laser cutter. In particular, first, it is necessary to draw a grid with a black marker on the glass, as shown in Figure 4.11: this step is useful for locally increasing the glass temperature when the laser passes on it.

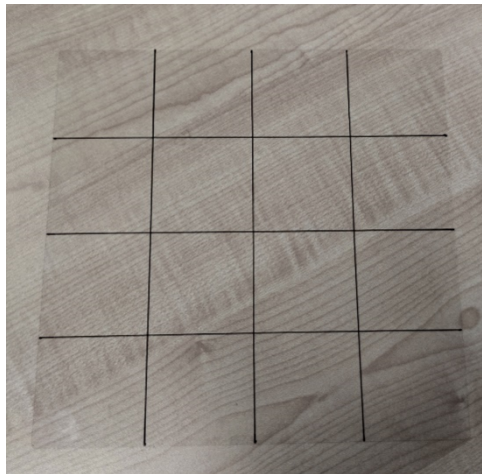


Figure 4.11: Preliminary step for cutting the glass by means of a laser cutter

The power and the velocity value have been fixed equal to 90% and 40%, respectively, while the distance of the tip from the glass (z) has been changed during the process. The following steps are included:

- Two at $z=0.3$ mm.

- Two at $z= 0.2$ mm.
- Seven at $z= 0.1$ mm.

With this approach, the fabricated prototypes are very precise, and the process becomes faster because it is possible to cut all the printed devices in only one step. Fabricated prototypes are shown in Figure 4.12: there is an optimal adhesion between the metal and the glass.

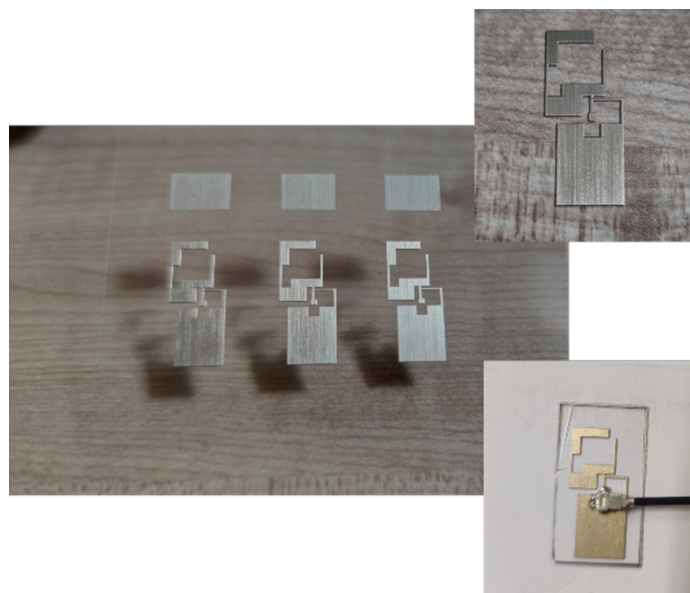


Figure 4.12: Fabricated prototypes on the glass substrate

The characterization step is performed for both the thicknesses of the glass: $200 \mu\text{m}$ and $100 \mu\text{m}$. The results in terms of the scattering parameter S_{11} of the comparison between numerical (blue curves) and experimental (red curves) results are shown in Figure 4.13.

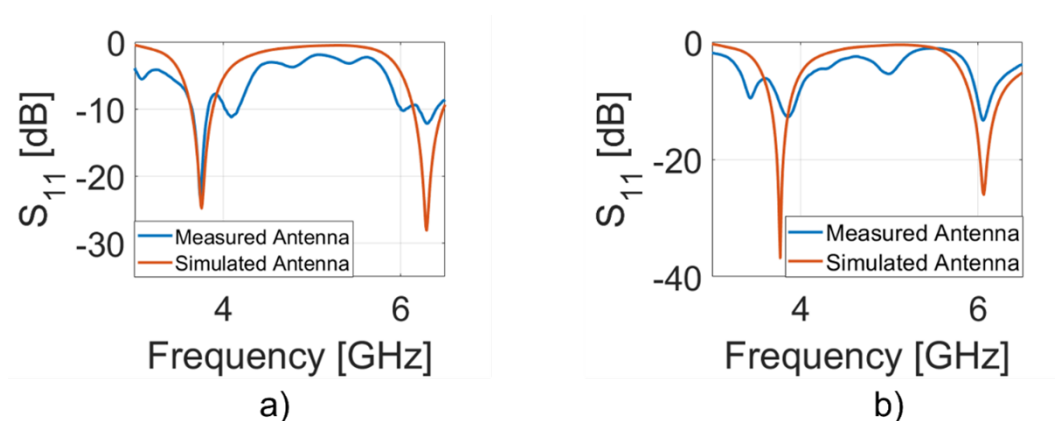


Figure 4.13: Comparison between simulated (red curve) and measured (red curve) for a) the 200 μm and b) 100 μm thick glass, respectively

Figure 4.13 a) shows that the results are in good agreement with the simulations as there are two resonances at 3.8 GHz and 6.3 GHz. Figure 4.13 b) reports the same comparison in the case of 100 μm -thick glass substrate; Also, in this case, it is possible to observe a good agreement between the two curves. In both of them, it is possible to note the presence of some small oscillations near the main dips due to the presence of the U.FL to SMA adapters.

Chapter 5

Chitosan-based Planar Inverted-F antenna

In the previous chapters, some examples of plastic-based antennas are reported, however, especially during this historical period, the bioimpact of the devices becomes a crucial aspect to take into consideration. The manufacture of antennas based on plastic-free and biodegradable substrates represents a strategic step forward in the quest for sustainability-conscious technology development. Among other bioadvantage materials, Chitosan is one of the best choices. Chitosan is a biodegradable material very cheap and can be easily extracted even from shrimp shells. Flexible foils having a high dielectric constant equal to 5 can be synthesized as reported in [91]. Another big advantage of this material is its optical transparency, which can reduce the visual impact by camouflaging the antenna. Chitosan obtained with this protocol presents also optimal piezoelectric properties suggesting its use in complex systems integrating radiofrequency antennas with microelectromechanical transducers (MEMs) [92, 93]. In this chapter, we combine the optimal peculiarity of PIFAs with eco-friendly materials realizing plastic-free antennas. In particular, we present two generations of antennas, the first using biocompatible materials and having a radiative part based on silver ink, and the second completely based on biodegradable materials using a PEDOT: PSS conductive layer [94]. The two generations present the same geometry, a planar-f

inverted antenna, and the same 35 μm -thick chitosan substrate. The geometry is designed to have a resonant frequency of 4.5 GHz and is optimized using an FDTD solver. Then, two fabrications of the antennas are exposed. The first based on silver nanoparticle ink is fabricated by depositing the metal tracks on a glass donor substrate and then transferred to the chitosan through pressure transfer printing. The second generation is fabricated by depositing the PEDOT: PSS on a polypropylene surface, then shaped with a laser cutter and transferred to the chitosan. The antennas are characterized in terms of S_{11} and radiation patterns. The results on the first generation show a very good agreement with the measures and optimal characteristics for the antenna. The second generation presents optimal properties as well, but there is a shift between the simulations and the experimental results, therefore the fabrication process has to be improved. In general, this chapter shows the potentiality of plastic-free antennas to realize wearable and biocompatible systems; and proposes two methods for their fabrication. The latter can be a crucial step forward for the integration of antennas in the Internet of Healthcare (IoHT) systems.

5.1 Chitosan Substrate synthesis

Chitosan is a biopolymer largely found in nature, such as in shrimp shells, and allows to obtain transparent, low cost and plastic-free substrates. It derives from the N-deacetylation of Chitin, a renewable raw material that can be extracted from the exoskeleton of crustaceans, and it is composed by repetitions of two units of N-Acetyl-D-Glucosamine and D-Glucosamine (Figure 5.1 a)). Moreover, due to its piezoelectric properties [91] it has the advantage of a high dielectric constant of 5, which allows compacting the antenna dimensions with respect to the ones on standard polymeric materials typically used. The approach used for the preparation of the chitosan film is the one described in detail in [91], but with a modified amount of chitosan. More in detail, a solvent-casting green technique has been exploited to realize the film: the Chitosan with medium molecular weight (Sigma Aldrich), is mixed in a solution with Milli Q water and Lactic Acid (Sigma Aldrich).

Then, it is stirred for 9 hours until the complete dissolution of chitosan to obtain a final solution with 1% w/w chitosan and 1% w/w of Lactic Acid. 40 mL of this mixture is poured into a Petri dish which is placed in an oven at a temperature of 40°C and vacuum conditions of 200 mbar. Films are left in the oven for about 12 h. At the end of this process, the solvent is completely evaporated, and the films are rinsed with a solution based on NaOH and water, then washed with distilled water until the washing solution shows a pH of around 7. Finally, chitosan wet films of 55 μm thickness can be peeled off from the Petri, and it can be used for the fabrication of the devices (an example is reported in Figure 5.1 b).

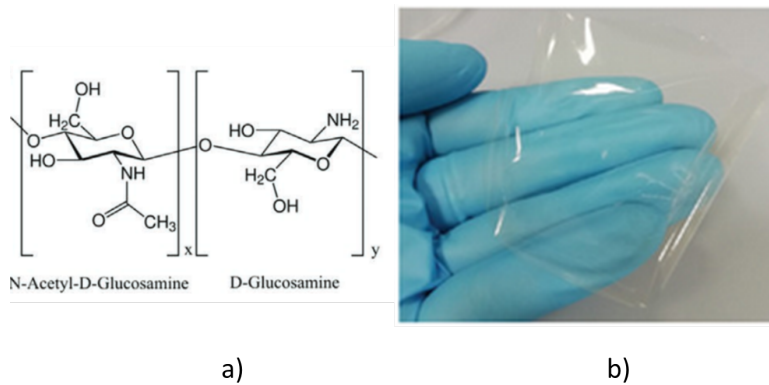


Figure 5.1: a) Chitosan molecule and b) example of chitosan film

5.2 Design and simulations of a metallic chitosan-based antenna

The designed geometry is a Planar Inverted-F Antenna, whose sketch is reported in Figure 5.2, with some modifications with respect to one of the previous chapter: the thickness of the strips has been increased to 1.5 mm and the parameters have been optimized for the new working frequency. This device is placed on biocompatible and flexible 55 μm -thick chitosan substrates. The geometrical parameter are listed in Table 5.1. The total footprint is 14x23 mm².

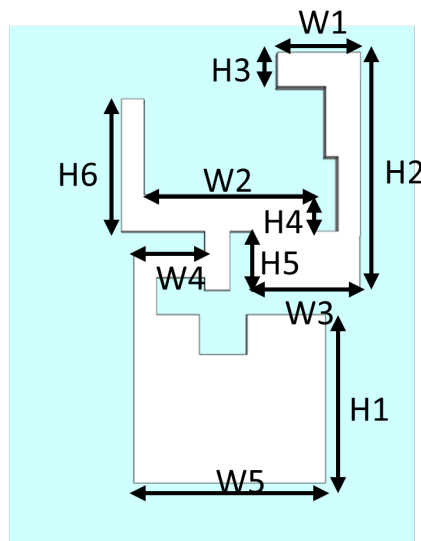


Figure 5.2: Sketch of the device

The most important parameters are $W1$ and $H1$, which are responsible for the resonant frequency, while the others are responsible for the impedance matching at 50Ω . The results of the simulations are shown in Figure 5.3.

Table 5.1: - List of the geometrical parameters

Parameter	Value[mm]
W1	3.5
W2	7
W3	4.5
W4	4
W5	8
H1	6
H2	10
H3	1.5
H4	1.5
H5	2.5
H6	3
H7	7

In figure 5.3 a) the trend of the scattering parameter S_{11} is reported: there is a dip of -14.6 dB at 4.5 GHz with a bandwidth of 250 MHz. The 3D radiation pattern for realized gain at the resonant frequency is shown in Figure 5.3 b); the maximum value is equal to 1.38 dBi. Finally, in Figure 5.3 c) and 5.3 d) the polar plots for E-plane ($\Phi=0^\circ$) and H-plane ($\Phi=90^\circ$) are represented. For $\Phi=0^\circ$, the main lobe magnitude is equal to 1.33 dBi and the main lobe direction is equal to 15.0 deg. Whereas for the $\Phi=90^\circ$ the main lobe magnitude is equal to 1.27 dBi and the main lobe direction is

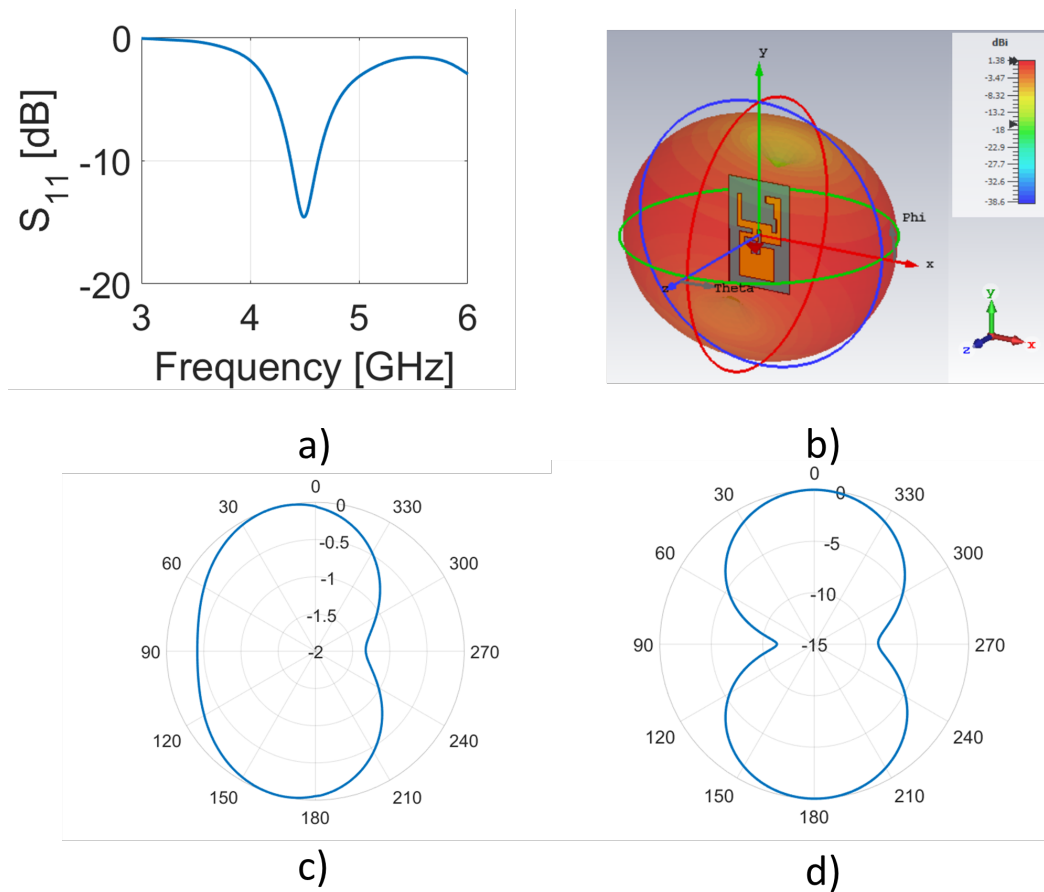


Figure 5.3: a) Simulated scattering parameter S_{11} of the PIFA, b) 3D radiation patterns at 4.5 GHz; simulated polar plot for the plane d) $\phi=0^\circ$ and e) $\phi=90^\circ$

equal to 0 deg. The simulated SAR is equal to 0.41 W/kg.

5.2.1 Fabrication Protocol

The steps for the antenna fabrication are shown in Figure 5.4.

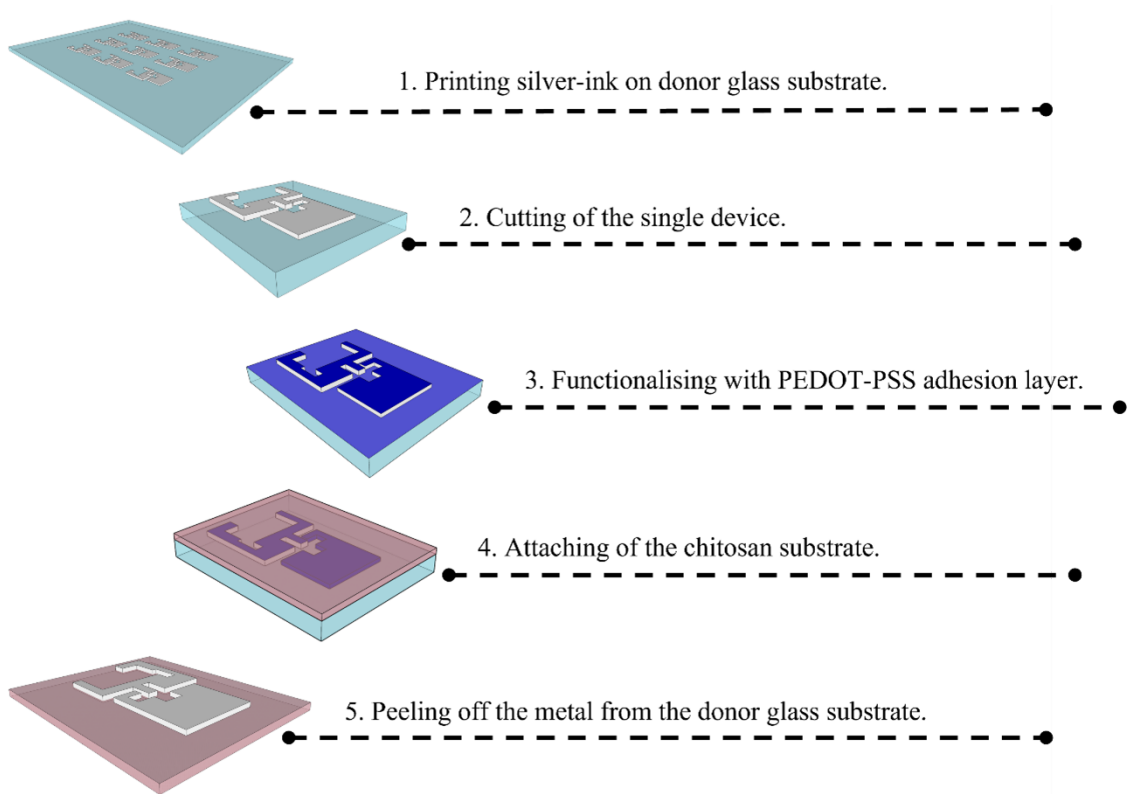


Figure 5.4: Fabrication steps

The first step is the printing of the Ag-based ink on a donor glass by means of NanoDimension's Dragonfly LDM multi-material 3D printer. In particular, $35\ \mu\text{m}$ of conductive ink is deposited and a total of about 25 antennas have been printed in less than two hours. After this, the process goes on with the second step, the cutting of a single antenna from the entire sheet utilizing a diamond tool (Figure 5.5); This passage is very important because each device becomes a sample on which the next steps are performed.

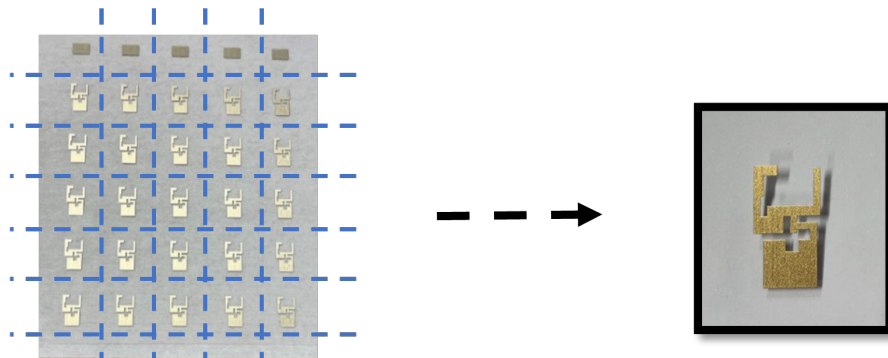


Figure 5.5: Cutting of the single device

The third step is the functionalization by a 200 nm-thick PEDOT: PSS/Glycerol (4%w/w) interlayer on the sample, which guarantees an optimal adhesion between the metal and the chitosan substrate, successively bonded on it. The PEDOT layer is cured at 140°C for 30 minutes. The last two steps are attaching the chitosan on PEDOT: PSS interlayer and peeling off the metal from the donor glass.

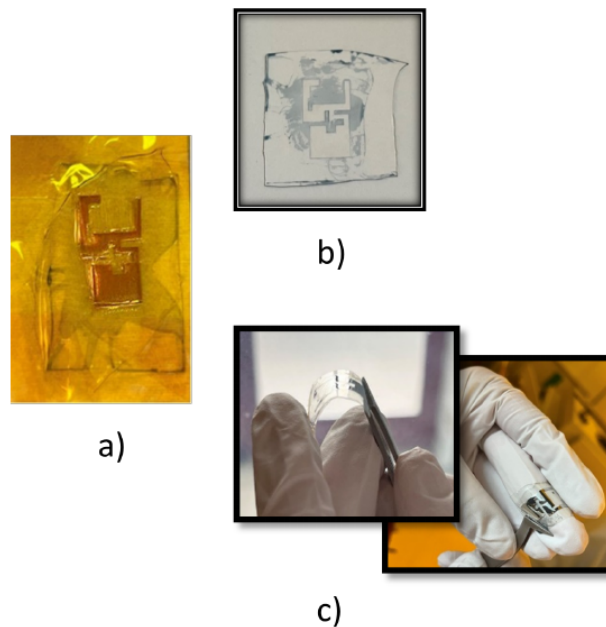


Figure 5.6: a) Attaching the substrate on the donor glass with a Kapton frame, b) peeling off the metal from the donor glass, c) final prototypes

More in detail, the chitosan substrate is placed on the donor glass with a frame of Kapton tape (Figure 5.6 a)) and it is put under a vacuum for 2 hours. Finally, the antenna is peeled off from the donor glass (Figure 5.6b)) and then, the prototype is completed with the soldering of the U.FL connector for performing the characterization step (Figure 5.6 c)). As it can be noted, the antennas are flexible and transparent, meeting the requirements for the realization of wearable and biodegradable sensors.

5.2.2 Characterization

The characterization of the device in terms of scattering parameter S_{11} by means of a VNA and radiation pattern polar plots. The results are reported in Figure 5.7.

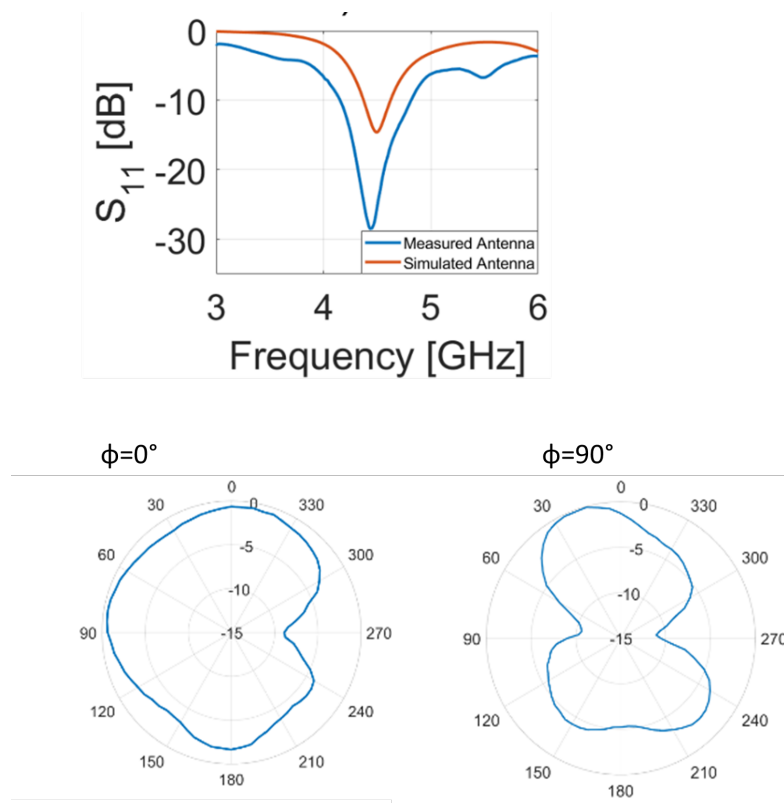


Figure 5.7: Simulated (red curve) and measured (blue curve) scattering parameter S_{11} of PIFA, measured polar plot at b) $\phi=0^\circ$ and c) $\phi=90^\circ$

In Figure 5.7 a) the comparison between the measured (blue curve) and simulated (red curve) scattering parameter S_{11} of the antenna is reported. It is possible to note a very good agreement in terms of resonance dip; the measured curve presents a wider bandwidth which is probably due to the losses of the material substrate and the presence of U.FL connector. In Figures 5.7 b) and c) the measured polar plots are shown. If we compare them with the simulated ones (Figure 5.2 c) and d)), it is possible to see that the positions of the nulls in the diagrams are the same for both planes (E-plane and H-plane). As regards the plane $\Phi = 0^\circ$, the measured one presents a minimum value that is lower than the simulated one; this is due to the presence of the cable in front of the antenna, the losses of the measurements set up, and the cables. For the second plane, $\Phi = 90^\circ$, there is a good agreement also in terms of minimum value, -15 dB for both of them. The back lobe of the measured one is lower than the simulated one: this is probably due to the presence of the absorber panels in the setup. The measured value of the gain is 1.72 dBi at the resonant frequency.

5.3 Design and Simulation of a non-metallic PIFA

The design of the device is the same as the section (see Figure 5.2). In this case, the conductive part is made of a 10 μm PEDOT: PSS layer with a conductivity of 1000 S/cm to have a biocompatible and biodegradable device. The substrate is, as before, the 55 μm -thick chitosan film. The results of the simulation are reported in Figure 5.8.

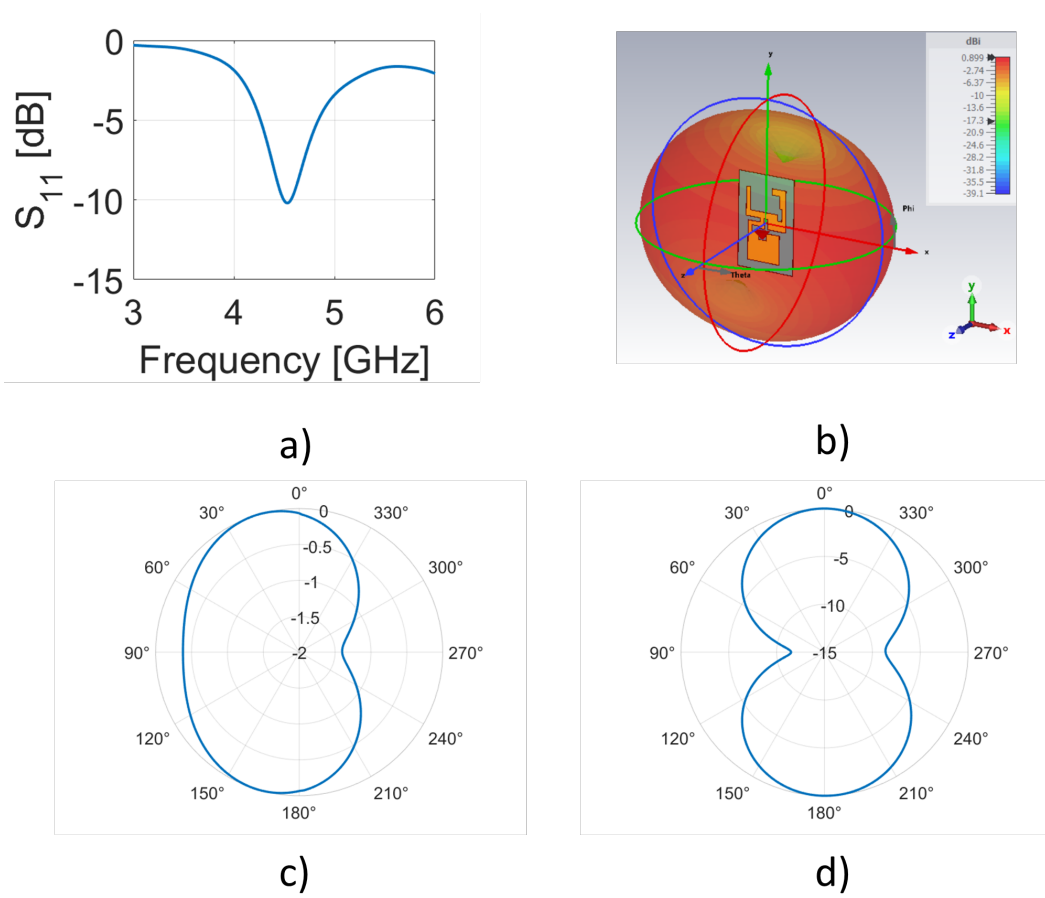


Figure 5.8: a) Simulated scattering parameter S_{11} of the PIFA, b) 3D radiation patterns at 4.5 GHz; simulated polar plot for the plane c) $\phi=0^\circ$ and d) $\phi=90^\circ$

In figure 5.8 a) the trend of the scattering parameter S_{11} is reported: there is a dip of -10.2 dB at 4.5 GHz with a bandwidth of 80 MHz. The 3D radiation pattern for realized gain at the resonant frequency is shown in Figure 5.8 b); the maximum value is equal to 0.89 dBi. Finally, in Figure 5.8 c) and 5.8 d) the polar plots for the planes $\Phi = 0^\circ$ (E-plane) and $\Phi = 90^\circ$ (H-plane) are represented. For the E-plane, the main lobe magnitude is equal to 0.81 dBi and the main lobe direction is equal to 17 deg. Whereas for the H-plane the main lobe magnitude is equal to 0.75 dBi and the main lobe direction is equal to 0 deg.

5.3.1 Fabrication

The preliminary step is the preparation of the dielectric substrate as detailed in Section 5.1. In this case, the radiating element is made of PEDOT: PSS (High conductivity grade, Sigma Aldrich) mixed in a solution with 4% of Glycerol (Sigma Aldrich). This specific percentage allows for obtaining a high conductive material ($\sigma = 1000 S/cm$), as explained in detail in [91]. The fabrication steps are exploited in Figure 5.9.

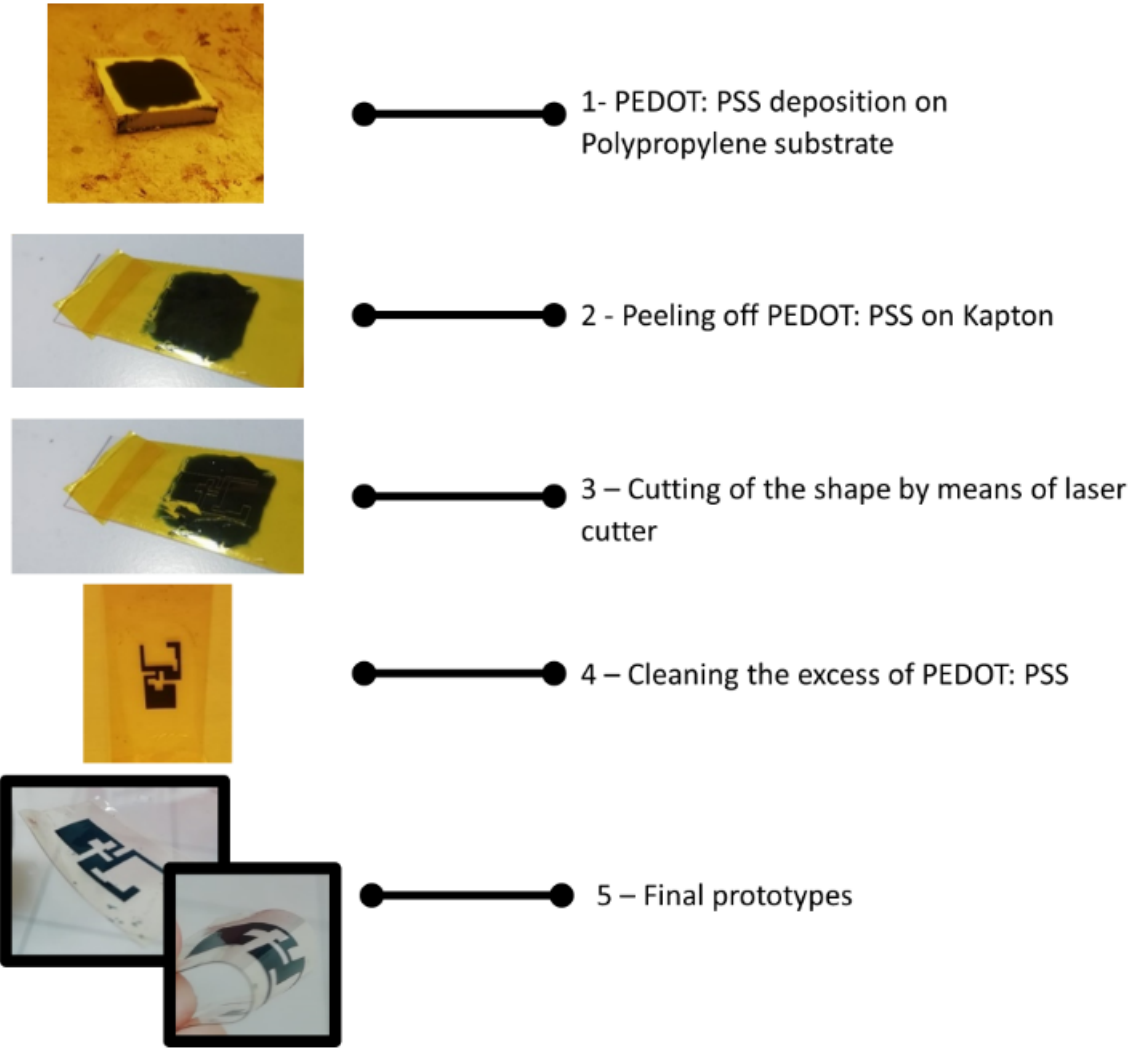


Figure 5.9: Fabrication steps

First, the PEDOT: PSS is deposited on a polypropylene substrate and cured at 140°C for 15 minutes. Next, the conductive layer is peeled off with a 25- μm thick Kapton tape: this is a very crucial step because it is necessary to avoid the breakage of the PEDOT: PSS layer; the polypropylene substrate allows to perform in a very easy way because its adhesion with the PEDOT is very low. After this, we cut the shape of the antenna using a laser cutter; and we clean the surface by removing the excess material. In the last step, the chitosan substrate is placed on the Kapton film, and the PEDOT: PSS layer is directly removed from it. The obtained final prototype is flexible and the adhesion between the two materials is very good.

5.3.1.1 Characterization of the fabrication process

Before characterizing the final prototypes, it is very important to characterize the fabrication process. Since the PEDOT: PSS is deposited on the substrate by hand, we have to verify the thickness of the conductive layer to avoid the insurgence of the Skin effect. When an alternating current flows in a conductor, the current distribution is not-uniform across the section of the conductor: it becomes higher in the outer part of the surface (skin) and lowers in the inner part [95]. This phenomenon can be neglected when the working frequency is in the range of 0 – 50 Hz with a section of the conductor of about tens of mm^2 . At high frequencies, we have to take into account that; in this case, the current J varies following an exponential function (Equation 5.1), decreasing from the surface towards the inside.

$$J(x) = J_0 e^{-\frac{x}{\delta}} \quad (5.1)$$

J_0 is the surface current density, x is the distance from the surface and δ is the deep of penetration at which $J(x) = J_0/e$. The depth of penetration can be expressed in the following Equation 5.2:

$$\delta = \sqrt{\frac{\rho}{\pi\mu f}} \quad (5.2)$$

It depends on the material of the conductor and on the frequency of the current: ρ is the conductor's resistivity, f is the frequency, and μ the absolute the magnetic permeability of the conductor. Since the PIFA has been designed for working at 4.5 GHz, the skin effect has to be taken into account. By considering the equation, it results that the minimum thickness for having a good conductive layer is $2.38 \mu\text{m}$. The thickness of the PEDOT: PSS layer has been measured employing an optical profilometer.

The results are shown in Figure 5.10.

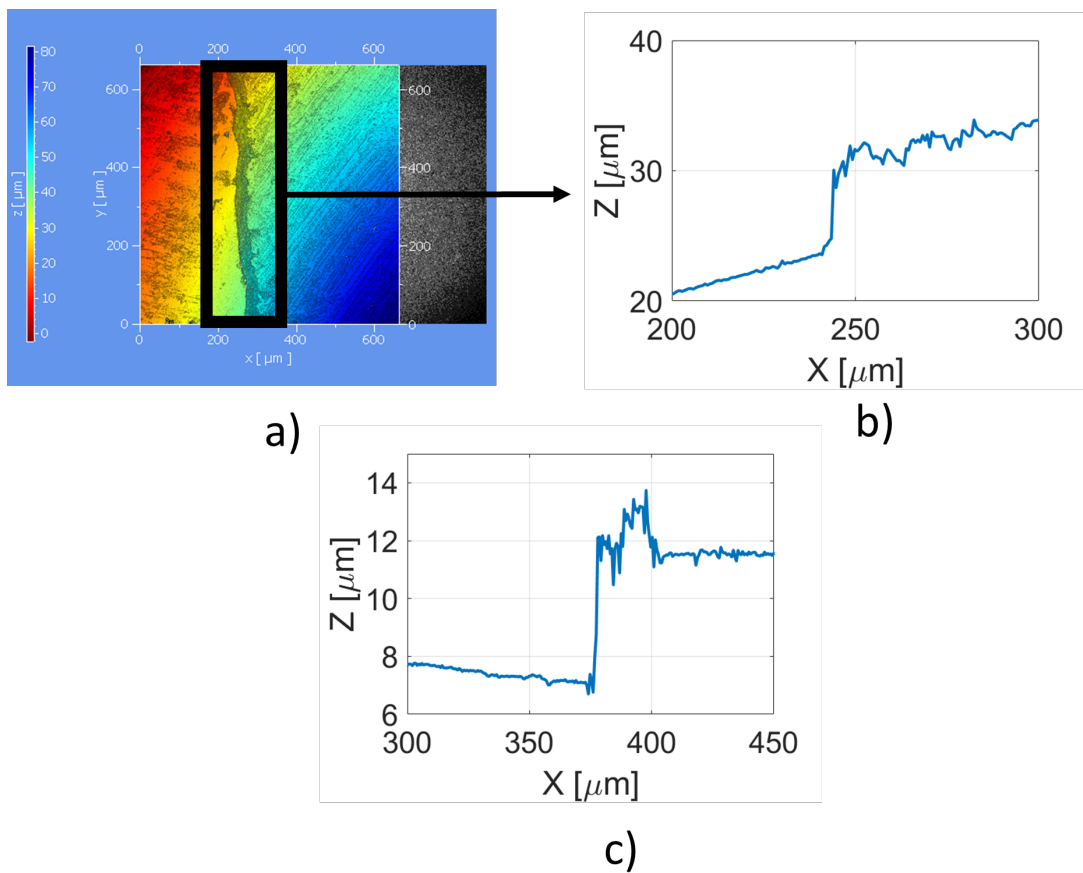


Figure 5.10: a) 3D and b) 2D measurements of the thickness of the PEDOT by means of an optical profilometer in the central part of the device, c) measurements of the thickness at the edges

It results that the thickness of the PEDOT: PSS is not uniform along the device. The analysis starts from the central part of the antenna. From

Figure 5.10 a) it is possible to see a variation in the height of the PEDOT layer: The thickness is equal to $11 \mu\text{m}$ (Figure 5.10 b)). The same approach has been used for the analysis of the edges. In this case, the thickness is low: it is about $4 \mu\text{m}$ (Figure 5.10 c)). As a consequence, it will be necessary to improve the fabrication process in order to better control the amount of the conductive material deposited on the substrate.

5.3.2 Device Characterization

For the characterization step, a U.FL connector is placed on the antenna. Since there are some limitations in terms of adhesion between the soldering and the PEDOT, for the positioning of the connector a silver-based conductive paste (MG Chemicals 8330S) has been used. It has been cured at 65°C for about 2 hours. Also for these prototypes, the characterization has been performed in terms of the scattering parameter S_{11} and 2D polar plots. The results are shown in Figure 5.11.

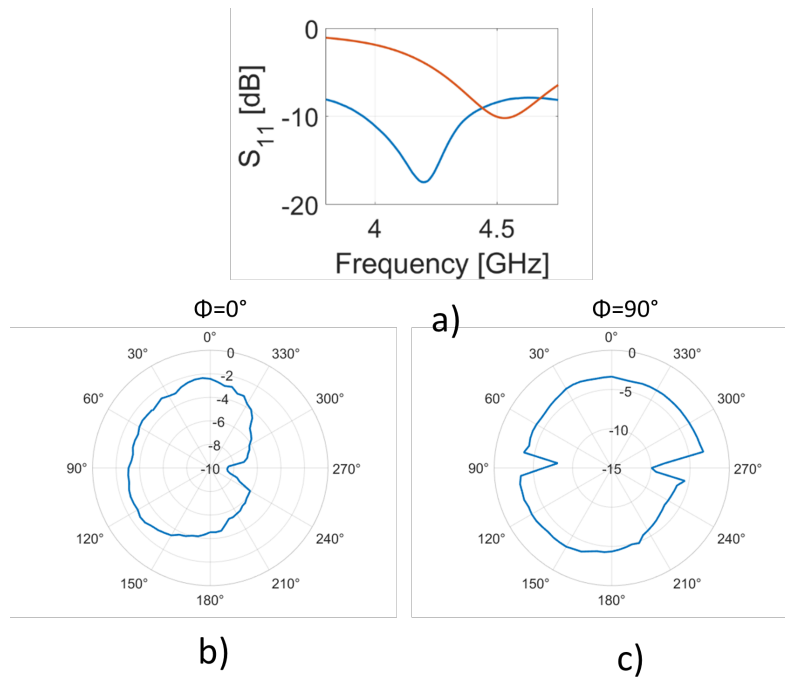


Figure 5.11: Simulated (red curve) and measured (blue curve) scattering parameter S_{11} of PIFA, measured polar plot at b) $\phi=0^\circ$ and c) $\phi=90^\circ$

From Figure 5.11 a) it is possible to note that the measured S_{11} is shifted at a lower frequency than the simulated one. This can be caused by multiple factors: the deposition of the PEDOT: PSS is performed by hand so the surface is not uniform and it is quite difficult to reproduce this in the simulations. In addition, for placing the connector it is necessary to put the device on a hot plate for a long time and this can vary the properties of the chitosan substrate. There are also losses due to the presence of the conductive paste and the U.FL connector.

As can be seen, comparing figures 5.8 b) and c) with figures 5.11 b) and c), the experimental polar plots slightly differ from the simulations. This effect can be justified with artifacts introduced by the radiation-pattern measurement kit. The antennas in this case present a very lightweight and flexible profile, therefore are subject to vibrations during the movements of the rotating stage which cause jags into the radiation pattern. Moreover, the maximum and minimum values of the gain are influenced by the polarization losses between the antennas. These are preliminary results: it is necessary to improve the fabrication protocol and also the properties of the conductive material for further characterization. As an example, [96] reported the chemical treatment used in to increase the conductivity of the PEDOT [97]. In particular, it has been demonstrated that by immersing the PEDOT layer in methanol, the conductivity will be significant increase by a factor of five. An alternative, reported in [98, 99], is to realize devices composed of a multilayer stack to increase the effective thickness of the conductive materials.

Chapter 6

Wearable system for vital parameters monitoring

The growing need to monitor vital parameters, accentuated by the SARS-COV-2 virus pandemic, encourages the exploration of technologies for wearable sensors. Among the physiological parameters that can be evaluated, the heart rate is one of the most measured and relevant since its demonstrated correlation with some clinical diseases [100, 101]. Electrocardiography (ECG) represents the gold standard technique for HR monitoring. The ECG electrodes measure the electrical activity of the heart from the skin surface. A typical waveform is characterized by five peaks and valleys (see Figure 6.1).

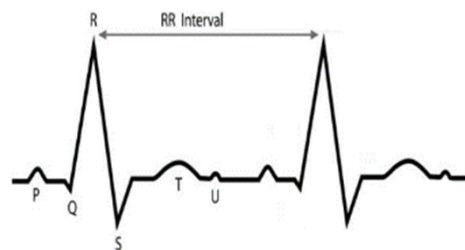


Figure 6.1: Classical ECG wave with identification of characteristic peaks [98]

On the contrary, photoplethysmography (PPG) is a well-known technology applied for example in smartwatches. PPG is a non-invasive technique

that is based on the study of the diffusion of light in the tissues to detect the change of blood volume in the subcutaneous micro-vascular network. The measures are typically taken in the peripheral areas of the human body, such as the fingers, feet, earlobes, forehead, etc. Although its great potential, PPG suffers from several disadvantages. Firstly, the outcomes are not as accurate as the EEGs. Moreover, the measuring system, composed of the light-emitting diode (LED) and the photodetector, complicates the sensing platform and increases power consumption.

Other information, such as the cardiac cycle and its phases can be extracted from the heart sound by means, for example, of echocardiogram. A single cycle of cardiac activity is composed of two different phases: diastole and systole. The first represents the period of time when the ventricles are relaxed; while the second regards the time during which the left and right ventricles contract and eject blood into the aorta and pulmonary artery, respectively.

A technology combining low-power consumption, high wearability, and also ability to relate the heartbeat derived from a mechanical deformation to an electronic signal can be extremely attractive, and piezoelectric sensors come to the aid. Piezoelectricity is the property of a material to produce an electronic signal in response to mechanical deformation and vice-versa. Reference [50] presents a flexible Aluminium Nitride (AlN) sensor on a polyimide substrate. The sensing platform shows extremely high sensitivity, and a compact footprint, and is based on a wearable and biocompatible Kapton substrate. Given this, it can be exploited to measure heartbeat through vein deformations in a non-invasive way.

Moreover, the integration of this technology with RF systems can pave the way for a new class of wireless and highly sensitive devices. The latter becomes a crucial challenge to integrate this technology into the scenario of the Internet of Healthcare Things (IoHT), where several nodes are connected in Wireless Sensor Networks (WSN). The standard architecture in IoHT systems exploits microprocessors to collect and transmit data. However, this approach increases the impact on the human body, the power consumption, and the costs of the sensing platforms.

In this chapter, we present a remote heart rate monitoring platform based on the sensor detailed in [50]. Rather than using a microprocessor, we transmit the raw data from the sensor using a Frequency Modulator (FM) and a patch antenna. This architecture reduces the number of supplementary components on the device and affects minimally the wearability of the sensing platform.

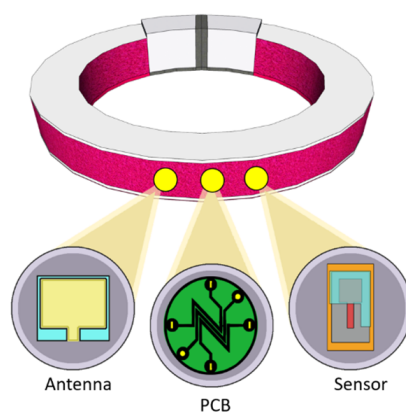


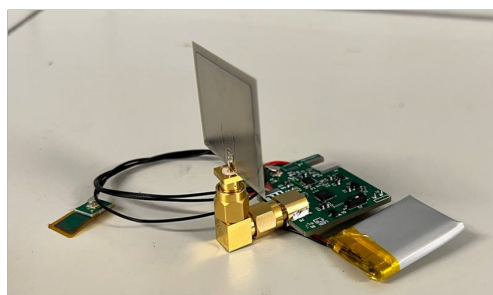
Figure 6.2: Sketch of the system

6.1 Design of the System

The realized sensing system is shown in Figure 6.3.



Receiving Side



Transmitting Side

Figure 6.3: Transmitting and receiving side of the realized system

More in detail, the platform is composed of a piezoelectric deformation sensor; a printed circuit board (PCB), and a patch antenna. The patch antenna has been designed for working at 3.6 GHz, in the sub-6GHz band of the 5G spectrum. The results in terms of the scattering parameter S_{11} and gain are shown in Figure 6.4. In Figure 6.4 a) the trend of the scattering parameter S_{11} is reported (blue curve): there is a dip of -23 dB at 3.6 GHz. Figure 6.4 b) shows the 3D realized gain for the antenna at the resonant frequency. The maximum value is 1.9 dBi.

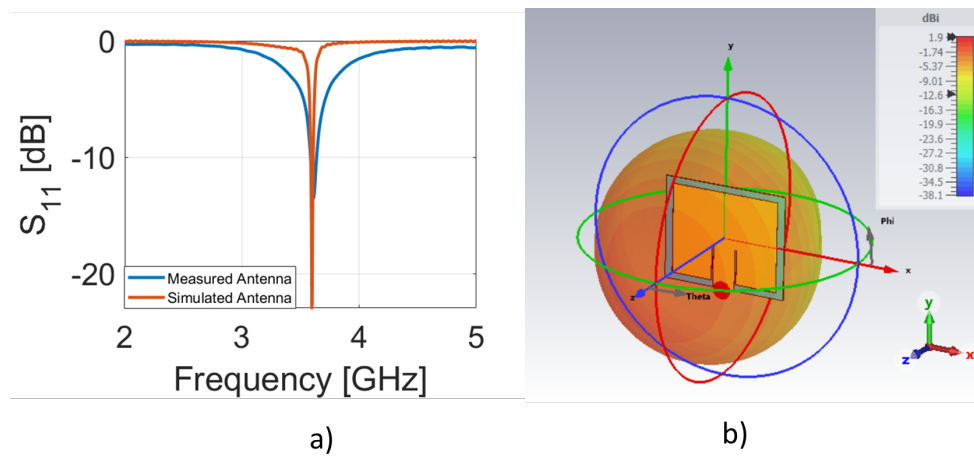


Figure 6.4: a) Comparison between the measured antenna (blue curve) and simulated antenna (red curve) of the scattering parameter S_{11} , b) 3D radiation pattern of the realized gain at 3.6 GHz

The Specific Absorption Ratio has also been simulated. The corresponding value is 0.05 mW/Kg with a stimulus power equal to 2 dBm, very far from the threshold of 2.0W/kg. The device has been fabricated on a PEN substrate with a 35 μm -thick metallic layer deposited by means of NanoDimension's Dragonfly LDM multi-material 3D printer. The antenna has been characterized in terms of S_{11} with a VNA. From Figure 6.4 a) it is possible to see a very good agreement between simulation (red curve) and measurements (blue curve) at the resonant frequency of 3.6 GHz. The piezoelectric sensor is shown in Figure 6.5.

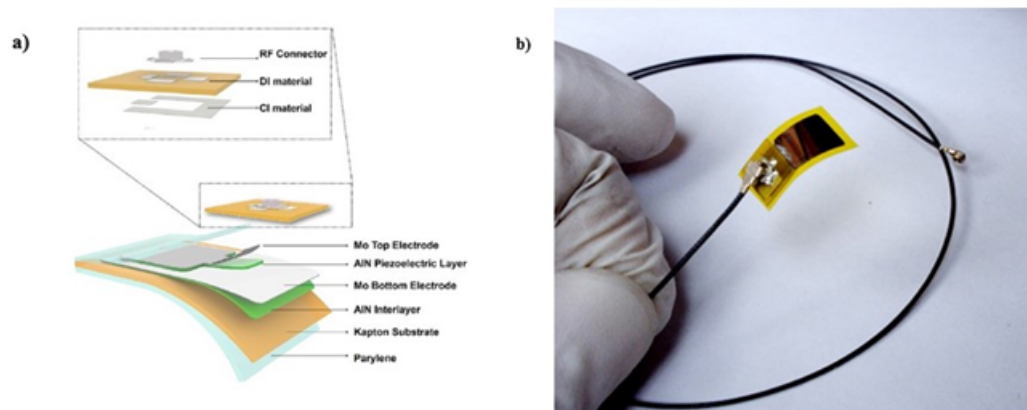
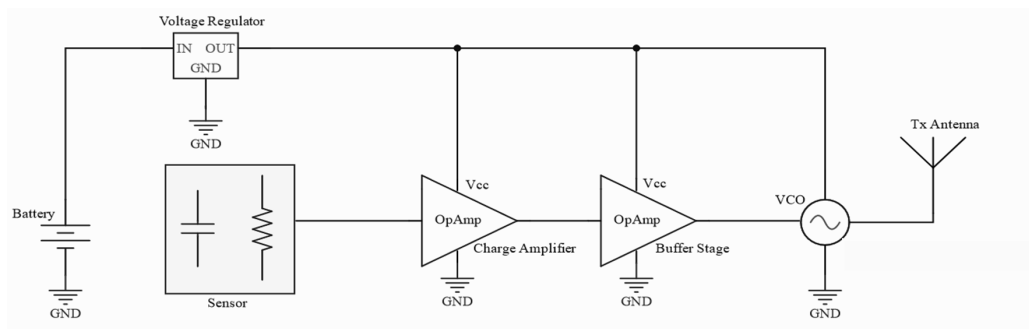
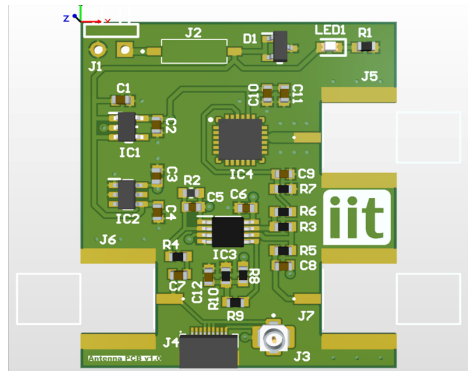


Figure 6.5: Flexible piezoelectric sensor; a) Exploded structure of the sensor and connector; b) picture of the sensor after all the fabrication processes [50]

The footprint is $10 \times 20 \text{ mm}^2$ with a sensitive area of 20 mm^2 and a thickness of fewer than $30 \text{ }\mu\text{m}$. The multilayer stack is formed by a piezoelectric aluminum nitride (AlN) layer sandwiched between molybdenum electrodes, grown on the top of an AlN interlayer deposited on a Kapton substrate. The structure has been protected by an electromagnetic shield made of parylene, titanium, and molybdenum for the stabilization of the charges. Finally, the sensor has been encapsulated in a supplementary parylene layer to guarantee waterproofing and resistance to oxidation of the metals. All the layers are obtained by sputtering depositions and patterned through a lift-off process. All the forming materials are non-toxic and biocompatible, minimizing the possibility of unwanted reactions after the application on the patients. The PCB reported in Figure 6.6 has been designed for conditioning the signal from the sensor and to perform the frequency modulation through a Voltage Controlled Oscillator (VCO).



a)



b)

Figure 6.6: Printed circuit board: a) Schematic of the board; b) Sketch of the mounted board

More in detail, the PCB consists of four main elements: the battery protection circuitry, the charge amplifier, the buffer stage, and VCO. The charge amplifier and the buffer stage are powered by voltage reference circuits whilst a dedicated voltage regulator is used for the VCO. The charge amplifier gain is 1 mV/pC to guarantee a minimum signal-to-noise ratio (SNR) of 80 dB. The buffer stage is utilized to tune the central frequency of the modulated signal on the desired working frequency. The VCO base frequency can be easily modified through a voltage divider circuitry, also integrated into the PCB. The last becomes a crucial aspect in the case of multiple sensors transmitting on a frequency division multiplexed channel. The sizes of the board have been contained to enhance the wearability of the system and are 30x35

mm^2 . The system comprises also a spectrum analyzer and a reader antenna to collect and analyze the signals from the board.

6.2 First generation board: Proof of Concept

To analyze the effectiveness of the system, the fidelity of the receiving signal has been tested by comparison with the modulating signal coming directly from the sensor. More in detail, the piezoelectric sensor has been attached to the skin in correspondence with the posterior tibial artery; and in the first phase, the signal has been collected by means of an oscilloscope (MDO4104-3-Tektronix) after the amplification by a benchtop charge amplifier (Kistler LabAmp Type 5165A), with the same settings used in the board (Figure 6.6). Secondly, the signal is applied as input to the board Figure 6.7

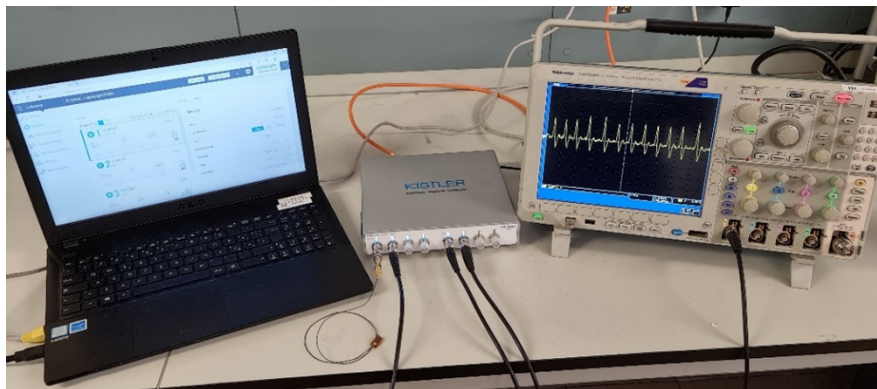


Figure 6.7: Measurements setup with Amplifier and Oscilloscope

Figure 6.8 shows the comparison between the output recorded by the oscilloscope (Figure 6.8a) and the one received at the reader side (Figure 6.8b). As it is possible to note, the HR measurement appears clear and with a very low level of noise in both cases. It results that no differences appear in the peak shapes obtained with oscilloscope or spectrogram.

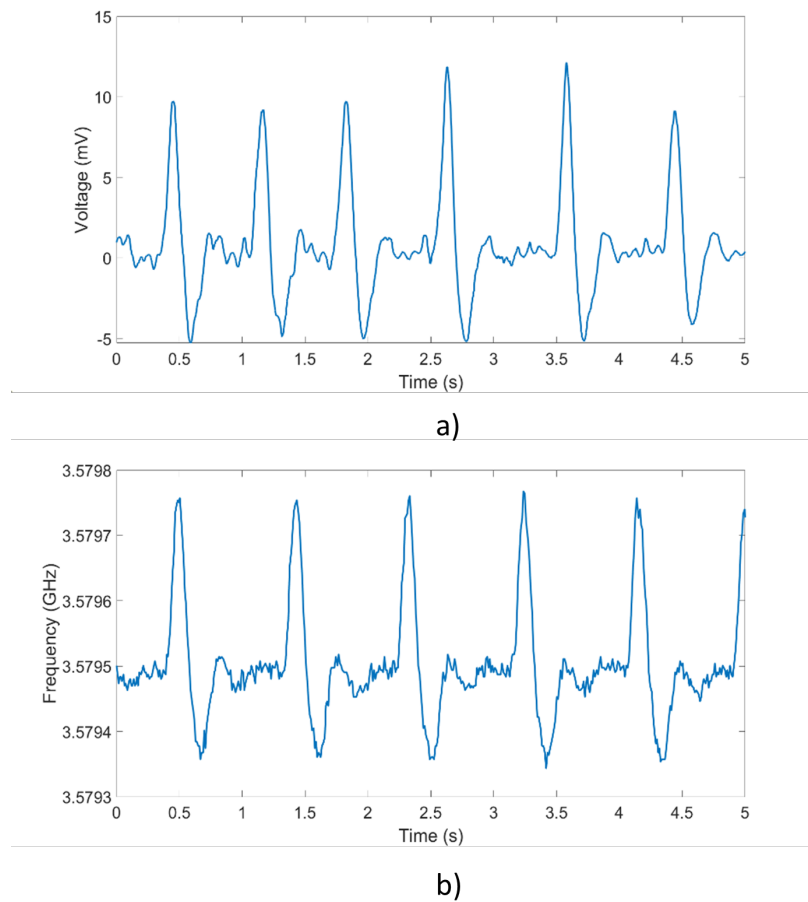


Figure 6.8: a) Signal recorded with the oscilloscope, b) signal received at the reader side

Although the system presents very interesting characteristics, there are some limitations in terms of power consumption (156 mW), which limits the battery life to 6h, and the dimensions of the antenna ($29 \times 24 \text{ mm}^2$).

6.3 Second generation board: integration of the evolved patch antenna

After the initial proof of concept, a new board has been developed to minimize the power consumption and the dimensions. The new system is shown in Figure 6.9.

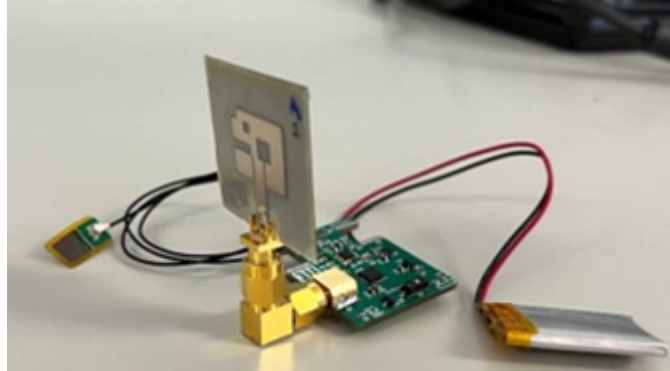


Figure 6.9: Realized system at 4 GHz with evolved patch antenna

The power has been reduced by the 50% (100 mW) and the battery life has been extended to 8.5h (250 mAh battery) using a low-consuming VCO working at the frequency of 4 GHz. Furthermore, the increase of the frequency allows for further reduce the dimensions of the antenna. In this regard, we have integrated the evolved patch antenna (see chapter 3) which combines a very small footprint ($17 \times 14 \text{ mm}^2$) with optimal radiation properties and low SAR values.

6.3.1 Characterization of the system

The second-generation board has been characterized in an indoor environment through the analysis of the signal-to-noise ratio (SNR), defined as in Equation 6.1 [102], for various angles and distances between the transmitting and the receiving antennas. The results are shown in Figure 6.10.

$$SNR = 10 \text{Log}_{10} \frac{P_{signal}}{P_{noise}} \quad (6.1)$$

where P_{signal} is the power of the signal, and P_{noise} is the noise level.

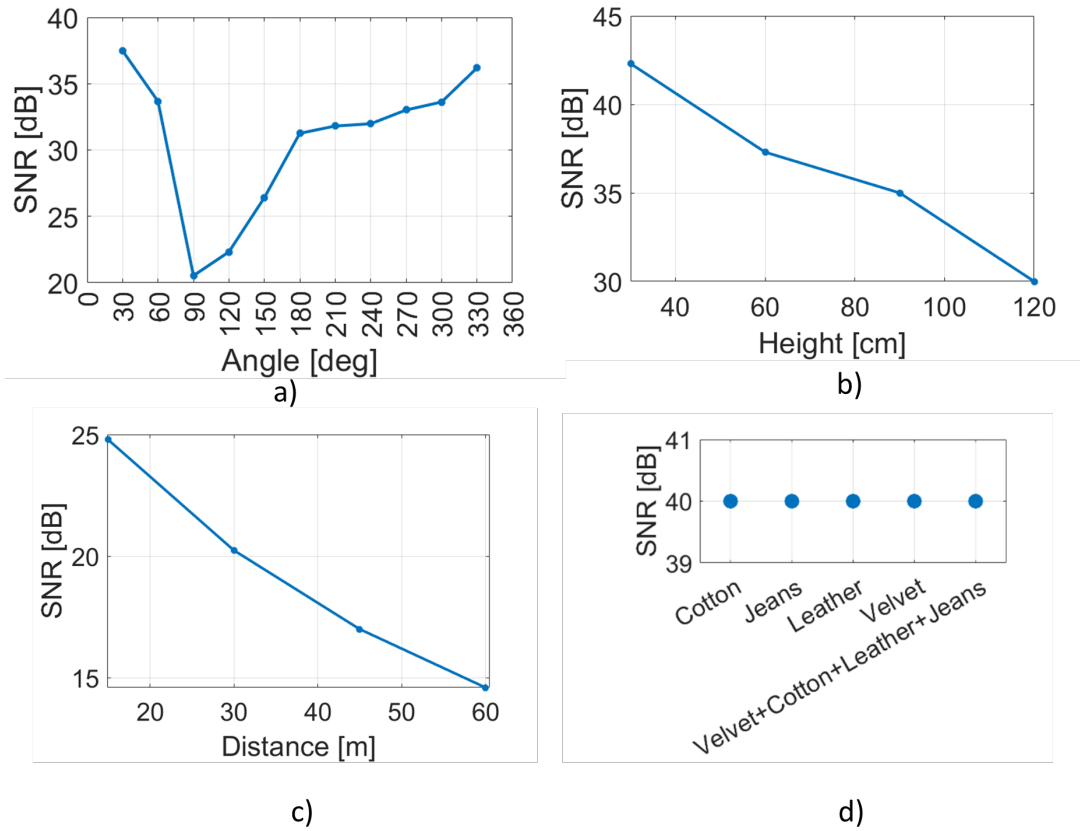


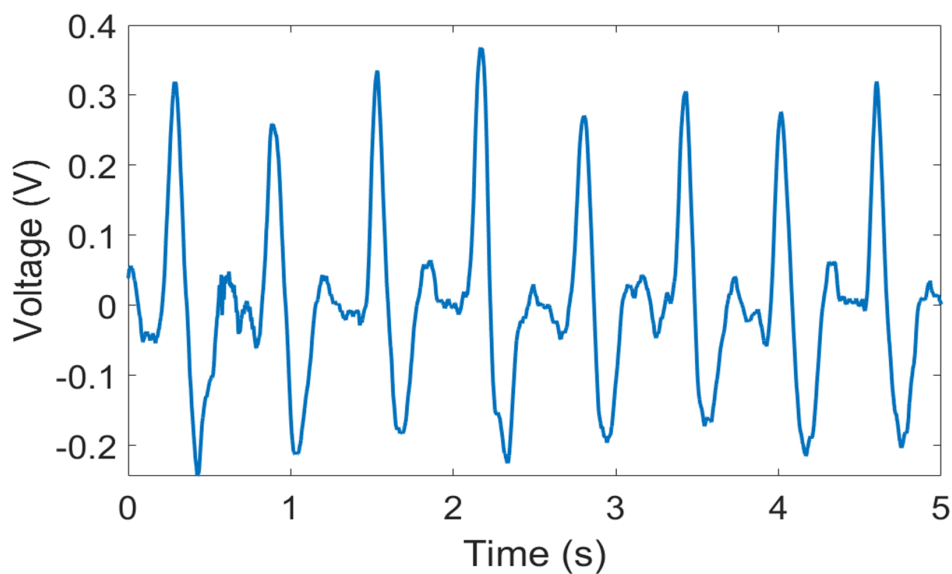
Figure 6.10: Signal to noise ratio (SNR) at different conditions: a) variation of angles between antennas; b) variation of heights between antennas; c) variation of the linear distance between antennas; d) different fabrics between antennas

Figure 6.10 a) reports the measured SNR for various angles. The antennas have been placed at a 1-meter distance from each other and one was rotated from 0 to 360°. As it is possible to note the signal level decreases monotonically from 0° to 90°. From 90° to 360° the trend is not symmetrical to the previous case. This situation is probably due to the asymmetry of the measurement environment affected by the presence of obstacles that cause multiple reflections (see Chapter 2). Figure 6.10 b) regards the SNR variations concerning the vertical angle between the antennas. The two antennas have been placed at a distance of 1 meter in the horizontal direction, while the vertical distance has been varied from 0 to 1.2 meters. The results are

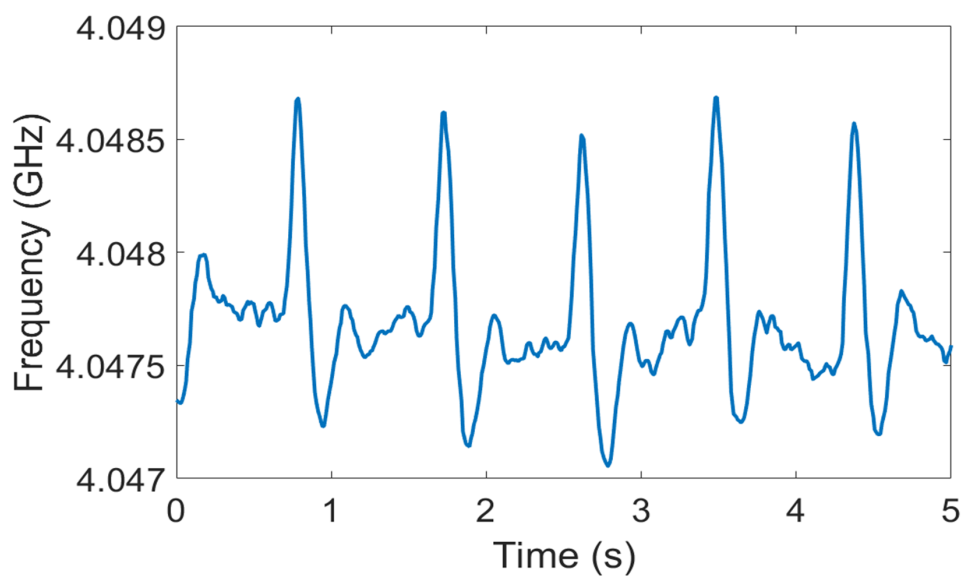
following theoretical expectations, as it is possible to note a decreasing trend as the vertical distance increases. In Figure 6.10 c) the antennas have been maintained in line of sight but their distance has been varied. The SNR level does not go under 15 dB even in the case of 60 meters. Figure 6.10 d) emulates the system in a wearable system. More in detail, the SNR has been measured after placing different fabrics between the antennas. As it can be noted there are no differences in the values of the signal level proving the possibility to integrate the antenna in pocket-like structures.

6.3.2 Measurements Results

After the characterization, the board has been placed on the ankle of the subject. The piezoelectric sensor has been attached to the skin in correspondence with the posterior tibial artery. The results have been reported in Figure 6.11.



a)



b)

Figure 6.11: Heartbeat signal; a) Signal from the oscilloscope b) Signal from the wearable system

Figure 6.11 a) shows the output signal analyzed using an oscilloscope (MDO4104-3-Tektronix) after the amplification by a benchtop charge ampli-

fier (Kistler LabAmp Type 5165A). Figure 6.11 b). It reports the demodulated signal after the wireless transmission; as can be noted from the analysis of the two graphs, the shapes of the peaks are identical, and no information has been lost during the transmission of the signal.

6.4 System Design in ISM Band

A new board fitting the Industrial Scientific and Medical (ISM) band has been fabricated. The working frequency of the antenna is around the central frequency of the band, at 5.8 GHz with a bandwidth of 150 MHz. Moreover, the new system reported in Figure 6.12 a) presents a significant reduction in dimensions; it is 24% smaller than the previous one.

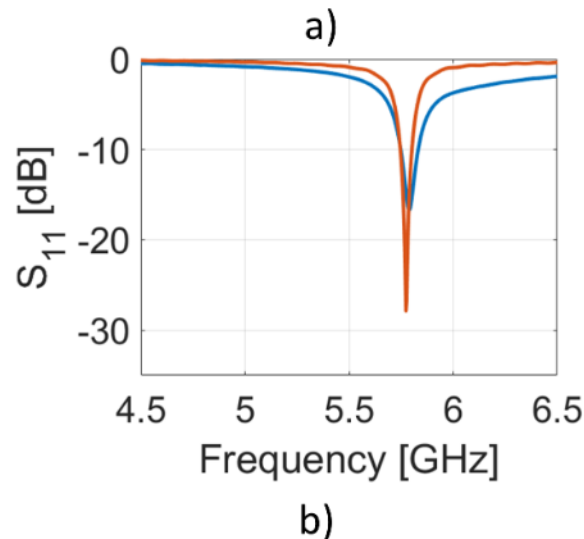
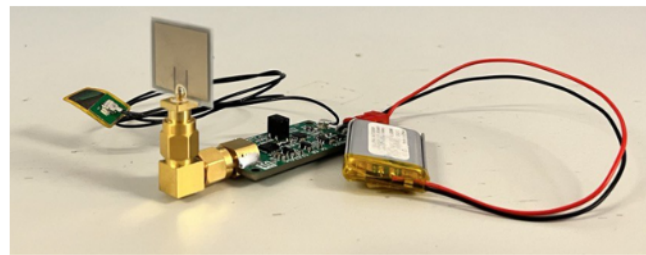


Figure 6.12: a) Realized system at 5.8 GHz and b) Characterization of the patch antenna

The antenna has been fabricated and characterized as detailed for the antenna in Section 6.1. The results of the comparison between the measured (blue curve) and simulated (red curve) show a very good agreement, Figure 6.12 b).

The Specific Absorption Ratio has been simulated also for this configuration. The corresponding value is 0.1 mW/Kg with a stimulus power equal to 2 dBm.

6.4.1 Characterization of the ISM Board

Figure 6.13 details the characterization of the new board in indoor and outdoor environments.

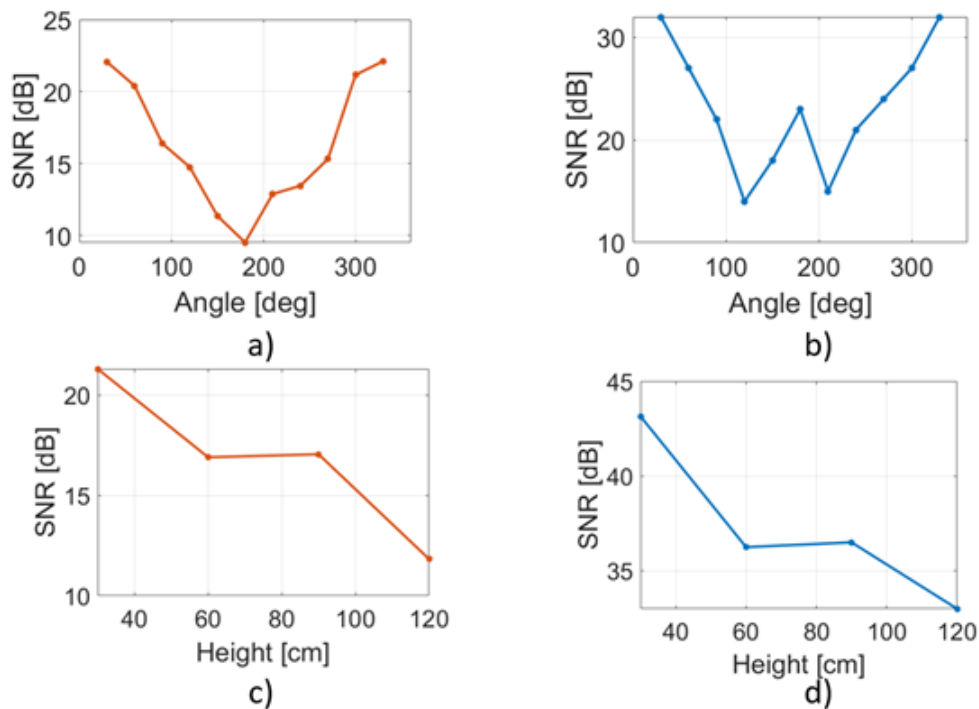


Figure 6.13: Signal to noise ratio (SNR) at different conditions: variation of angles between antennas a) outdoor and b) indoor; different heights between antennas c) outdoor and d) indoor.

Figure 6.13 a) reports the SNR for different angles in outdoor conditions. As it is possible to note the data are perfectly in accordance with expectations

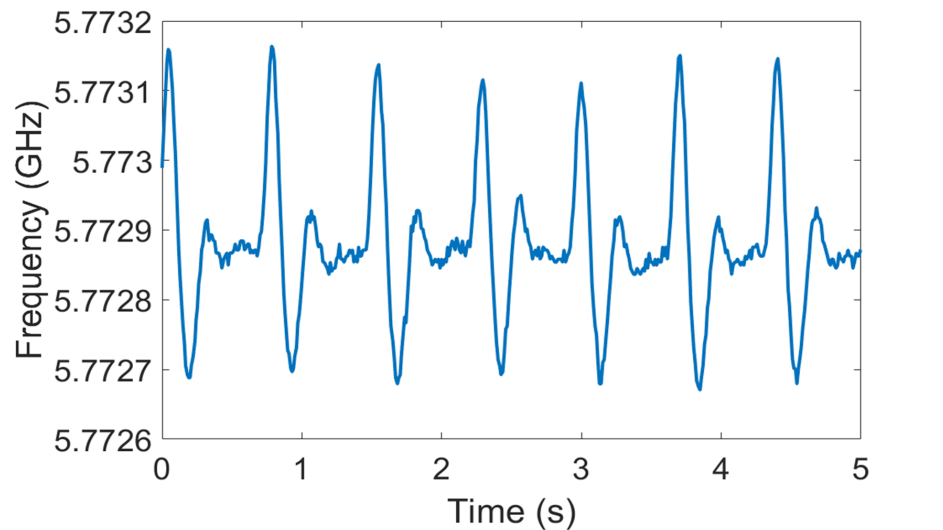
as there is a minimum at 180° . The indoor measurements are reported in Figure 6.13 b). Although also in this case it is possible to observe a decreasing behavior from 0° to 100° , while the signal level increases locally at 180° . This effect is due to reflections occurring in indoor propagation. Figure 6.13 c) and d) details on the SNR evaluated varying the position of the antennas in height in case of outdoor and indoor, respectively. In these cases, the trends indoors and outdoors are very similar and in line with theoretical expectations, as the SNR decreases with the increase of the relative height between the antennas.

6.4.2 Results in ISM band: from single to multiple subjects

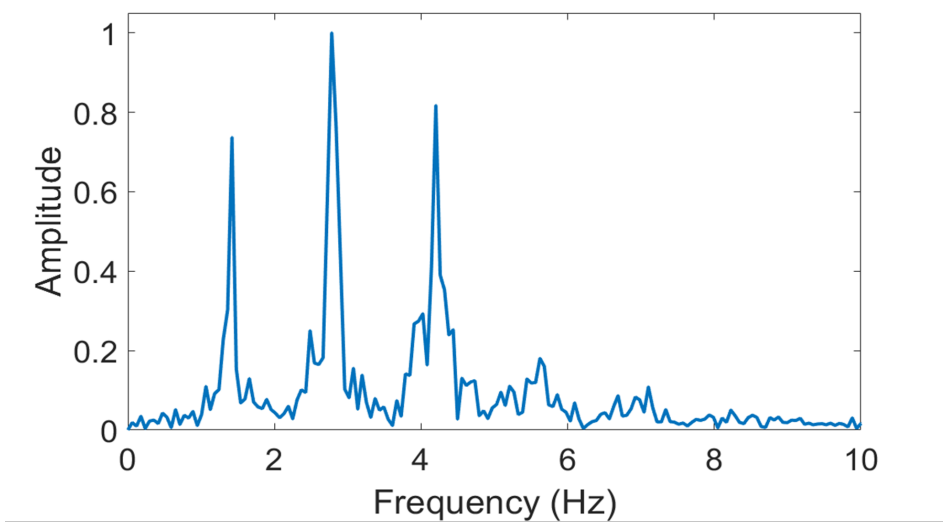
Figure 6.14 shows the results of the system in the ISM band. Figure 6.14 a) reports the signal directly acquired with the new board, while in Figure 6.14 b) the corresponding Fast Fourier Transform (FFT) is represented. From the FFT analysis, it is possible to extract important parameters like the heart rate, and the durations of the phases of the cardiac cycle, and the ratio between them [103]. Systolic and diastolic phases are generally measured from heart sound signals or echocardiograms [104, 105], while with this approach they are extracted from a mechanical deformation of the piezoelectric sensor. More in detail, as it can be noted in the spectrum of the signal there are three different peaks. Each one is referring to a different parameter:

1. The first peak between 0.8 and 1.5Hz is correlated to the heart rate, obtained by multiplying the frequency by 60, that at rest is in the range of 48 to 90 bpm.
2. The second peak between 2 and 3 Hz regards the diastole or rest of the heart, which at rest lasts about 0.4 seconds, and represents a phase of the heart cycle that has a duration that does not change very much with the duration of the heart cycle.
3. The third peak between 3 and 5 Hz regards the ventricular systole, which lasts about 0.3 seconds, however, the duration of this phase is

strictly correlated to the duration of the heart cycle.



a)



b)

Figure 6.14: Heartbeat signal transmitted at the frequency of 5.8 GHz; a) Demodulated signal; b) Fast Fourier Transform of the signal

With the new generation of the board, we explored also the possibility to read multiple sensors from several subjects. Three different boards having

the VCOs tuned at different frequencies are used to transport the HR-signals, exploiting a Frequency Division Multiplexing (FDM) approach and the same reader gateway. Figure 6.15 reports three signals acquired on three different subjects simultaneously.

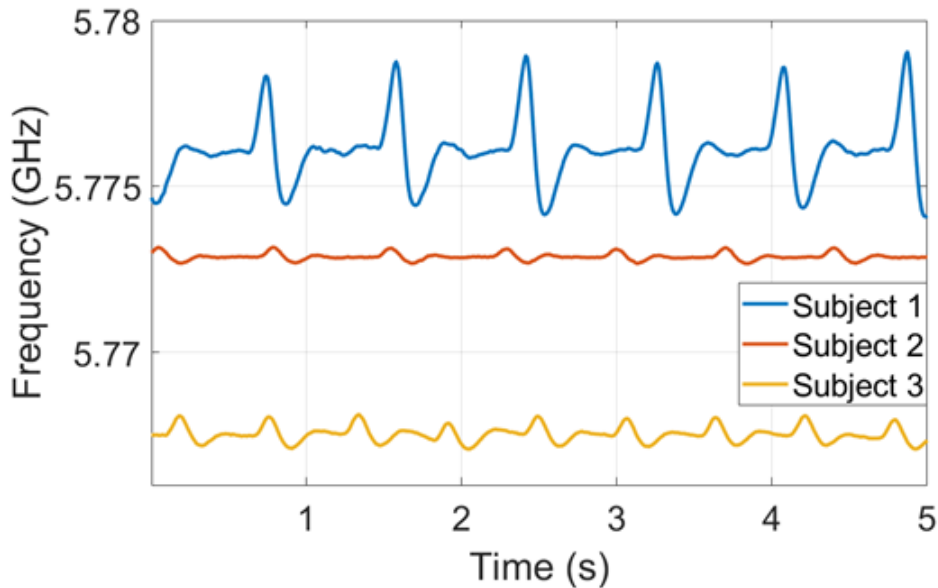


Figure 6.15: Heartbeats were extracted from three subjects

The signal of subject 1 (blue) is significantly higher concerning the others, this behavior can be associated with higher blood pressure which corresponds to a higher deformation of the artery. The blood pressure of the subjects has been measured with a medically validated device to justify this observation. As we were expecting subjects 2 and 3 have similar pressure, 109/73 mmHg and 114/66 mmHg respectively, while subject 1 shows a blood pressure of 134/95 mmHg confirming the initial assumptions. It is underlined that the maximum difference in frequency span observed in the signals is about 4 MHz; therefore considering a maximum amplitude of the signal of 7 MHz and about 3 MHz of guard bands, as estimation is possible to monitor about 15 people simultaneously using a single reader.

6.4.3 Summary of the sensor platform configurations

In conclusion, the main characteristics of the three wearable systems realized, are summarized in following Table 6.1.

Three different generations of the sensing platform have been developed. The first one works at 3.6 GHz and presents a high power consumption (156 mW) that causes a low battery life, of around 6 hours. The second generation has been improved regarding the previous two aspects; in fact, the power consumption is 102 mW while the battery is improved until 8.5 hours. The first two platforms present a quite big dimension; to make it suitable for wearable applications, the third generation has been realized with a size reduction of 24%.

Table 6.1: Summary of the three-generation boards

	First Generation	Second Generation	Thirth Generation
Working frequency [GHz]	3.6	4	5.8
Dimensions of the board [mm^2]	30X35	30X35	20X40
Dimensions of antenna [mm^2]	30X25	17X14	16X14
Power Consumption [mW]	150	102	102
Battery Life [h]	6	8.5	8.5

Chapter 7

Conclusion

The integration of wearable and flexible antennas with low-invasive sensors can pave the way for a new class of wireless and wearable platforms for health monitoring. Such kinds of devices found applications in a huge variety of scenarios that go beyond classical wearable technologies.

Although their interesting perspectives, several challenges have to be overcome in the realization of high-performance flexible antennas. The geometry of the antennas has to be properly designed to be as compact as possible and characterized by optimal radiation properties combined with minimal risks from the application on the human body. In this scenario, several examples of antennas have been designed, fabricated, and characterized in this thesis. They can be summarized below:

1. An evolved patch antenna loaded placed on an SRR which combines a very compact footprint and low SAR has been developed. The antenna has been realized with a fabrication protocol suitable for rapid prototyping and mass production. The results show optimal radiation properties and a lightweight profile ideal for wearable applications such as smart tattoos or remote sensing platforms.
2. Flexible PIFAs on PEN and flexible glasses are reported. The obtained antennas combine low-invasive profiles and optimal radiation properties. Moreover, the planar geometry allows a rapid printing process and increases the fabrication yield.

3. Two examples of plastic-free PIFA antennas are presented. The antennas are based on the same dielectric substrate made of biocompatible chitosan but the radiative part of the first is made of silver nanoparticle conductive ink, while the second is based on a biodegradable material as a conductive layer, the PEDOT: PSS. Both two generations show a compact footprint and a minimal visive impact and are demonstrated to be a valid choice for wireless sensor systems.

Concluding, all the proposed antennas represent an optimal choice in the Internet of Healthcare Things (IoHT) scenarios and, in general, for health remote monitoring.

Another extremely important factor to consider, especially in long term is the impact factor of the devices. Plastics and toxic compounds represent most of the materials utilized in the electronic industry; therefore, a strategy to reduce their use becomes crucial to follow scientific progress giving an eye on the health of our planet. In this regard, in the last part of this work, the integration between a flexible highly sensitive wearable sensor with three different wearable antennas is presented.

The first generation works at 3.6 GHz (in a licensed band of sub-6GHz band of 5G) by means of a small electronic board of $30 \times 35 \text{ mm}^2$, characterized by power consumption of 156 mW and a footprint of the antenna of about $25 \times 25 \text{ mm}^2$. With the second generation, the power consumption is strongly reduced, and the antenna is more compact, $14 \times 17 \text{ mm}^2$. The third generation works at 5.8 GHz in the ISM band. Despite the higher working frequency, the power consumptions are the same as the second generation, but the dimensions of the board are reduced to 31%. All three boards demonstrated the capability to transmit with very high fidelity the heartrate signal even in non-line of sight conditions, in indoor and in outdoor environments.

Future development can be the refining of the fabrication protocol of the chitosan antennas and the integration of a final biodegradable prototype for the monitoring of healthcare. The last can be a crucial step to open two interesting scenarios. On one side, the realization of a low-invasive wearable sensing platform, or on the other side, the fabrication of edible sensors exploiting the piezoelectric properties of the chitosan and the wireless com-

munication of the antennas.

Another step forward for this work could be the integration of the system composed of a flexible antenna, electronic board, and piezoelectric sensor in a final compact prototype which allows the possibility to realize a body area network able to monitor vital parameter on a different part of the human body at the same time.

References

- [1] S.-F. Tseng and Y.-S. Tsai, “Highly sensitive humidity sensors based on li-c3n4 composites on porous graphene flexible electrodes,” *Applied Surface Science*, vol. 606, p. 155 001, 2022, ISSN: 0169-4332. DOI: <https://doi.org/10.1016/j.apsusc.2022.155001>.
- [2] J. Yang *et al.*, “Flexible, tunable, and ultrasensitive capacitive pressure sensor with microconformal graphene electrodes,” *ACS Applied Materials & Interfaces*, vol. 11, no. 16, pp. 14 997–15 006, 2019. DOI: [10.1021/acsami.9b02049](https://doi.org/10.1021/acsami.9b02049).
- [3] X. Zhang *et al.*, “High-performance multimodal smart textile for artificial sensation and health monitoring,” *Nano Energy*, vol. 103, p. 107 778, 2022, ISSN: 2211-2855. DOI: <https://doi.org/10.1016/j.nanoen.2022.107778>. [Online]. Available: <https://www.sciencedirect.com/science/article/pii/S2211285522008552>.
- [4] C. Dagdeviren *et al.*, “Flexible piezoelectric devices for gastrointestinal motility sensing,” *Nature Biomedical Engineering*, vol. 1, pp. 807–817, 2017.
- [5] L. Beker and Y. Kaizawa, “Biodegradable and flexible arterial-pulse sensor for the wireless monitoring of blood flow,” *Nature Biomedical Engineering*, vol. 3, pp. 47–57, Jan. 2019. DOI: [10.1038/s41551-018-0336-5](https://doi.org/10.1038/s41551-018-0336-5).
- [6] W.-J. Tsay and J. Aberle, “Analysis of a microstrip line terminated with a shorting pin,” *IEEE Transactions on Microwave Theory and Techniques*, vol. 40, no. 4, pp. 645–651, 1992. DOI: [10.1109/22.127511](https://doi.org/10.1109/22.127511).

- [7] B. Hu, G.-P. Gao, L.-L. He, X.-D. Cong, and J.-N. Zhao, "Bending and on-arm effects on a wearable antenna for 2.45 ghz body area network," *IEEE Antennas and Wireless Propagation Letters*, vol. 15, pp. 378–381, 2016. DOI: 10.1109/LAWP.2015.2446512.
- [8] K. Fujimoto and H. Morishita, *Modern Small Antennas*. Cambridge University Press, 2014.
- [9] T. Inui, H. Koga, M. Nogi, N. Komoda, and K. Suganuma, "A miniaturized flexible antenna printed on a high dielectric constant nanopaper composite," *Advanced Materials*, vol. 27, no. 6, pp. 1112–1116, 2015. DOI: <https://doi.org/10.1002/adma.201404555>. eprint: <https://onlinelibrary.wiley.com/doi/pdf/10.1002/adma.201404555>. [Online]. Available: <https://onlinelibrary.wiley.com/doi/abs/10.1002/adma.201404555>.
- [10] P. Soontornpipit, C. Furse, and Y. C. Chung, "Miniaturized biocompatible microstrip antenna using genetic algorithm," *IEEE Transactions on Antennas and Propagation*, vol. 53, no. 6, pp. 1939–1945, 2005. DOI: 10.1109/TAP.2005.848461.
- [11] B. R. Behera, "Sierpinski bow-tie antenna with genetic algorithm," *Engineering Science and Technology, an International Journal*, vol. 20, no. 2, pp. 775–782, 2017, ISSN: 2215-0986. DOI: <https://doi.org/10.1016/j.jestch.2016.10.017>. [Online]. Available: <https://www.sciencedirect.com/science/article/pii/S2215098616306747>.
- [12] R. Mishra, R. Mishra, P. Kuchhal, and P. Kumari, "Optimization and analysis of high gain wideband microstrip patch antenna using genetic algorithm," *International Journal of Engineering and Technology (2227-524X)*, vol. 7, Jan. 2018. DOI: 10.14419/ijet.v7i1.5.9142.
- [13] P. Suraj, B. Behera, and R. Badhai, "Optimization of metamaterials-based wi-fi antenna using genetic algorithm," *National Academy Science Letters*, vol. 43, pp. 333–337, Jan. 2020. DOI: 10.1007/s40009-020-00876-5.

- [14] I. Marasco *et al.*, “A compact evolved antenna for 5g communications,” *Scientific Reports*, vol. 12, p. 10 327, Jun. 2022. DOI: 10.1038/s41598-022-14447-9.
- [15] Z. Li and K. Gong, “Design of a printed monopole antenna for dualband wlan application using pso,” in *2006 7th International Symposium on Antennas, Propagation & EM Theory*, 2006, pp. 1–4. DOI: 10.1109/ISAPE.2006.353472.
- [16] H. S. Girija, R. Sudhakar, K. M. Abdul Kadhar, T. S. Priya, S. Ramanathan, and G. Anand, “Pso based microstrip patch antenna design for ism band,” in *2020 6th International Conference on Advanced Computing and Communication Systems (ICACCS)*, 2020, pp. 1209–1214. DOI: 10.1109/ICACCS48705.2020.9074290.
- [17] I. Bouhassoune, A. Chehri, R. Saadane, and K. Minaoui, “Optimization of uhf rfid five-slotted patch tag design using pso algorithm for biomedical sensing systems,” *International Journal of Environmental Research and Public Health*, vol. 17, no. 22, 2020, ISSN: 1660-4601. DOI: 10.3390/ijerph17228593.
- [18] R. Vatti, B. Arthi, P. Kumar, and R. Prabha, “Gain enhancement by utilizing hexagonal reflector based optimized textile antenna,” *Journal of Ambient Intelligence and Humanized Computing*, Feb. 2021. DOI: 10.1007/s12652-020-02863-6.
- [19] L.-Y. Xiao, W. Shao, F.-L. Jin, and B.-Z. Wang, “Multiparameter modeling with ann for antenna design,” *IEEE Transactions on Antennas and Propagation*, vol. 66, no. 7, pp. 3718–3723, 2018. DOI: 10.1109/TAP.2018.2823775.
- [20] A. I. Hammoodi, M. Milanova, and H. Khaleel, “Design of flexible antenna for uwb wireless applications using ann,” in *2017 International Conference on Computational Science and Computational Intelligence (CSCI)*, 2017, pp. 751–754. DOI: 10.1109/CSCI.2017.344.

- [21] R. Kumar, D. P. Kumar, and R. Vijay, "Hexagonal shaped slot antenna resonant frequency determination using ann approach," *Microwave Review*, vol. 25, pp. 27–30, Jul. 2019.
- [22] Z.-B. Weng, Y.-C. Jiao, and F. Zhang, "A directive dual-band and dual-polarized antenna with zero index metamaterial," *Microwave and Optical Technology Letters*, vol. 50, pp. 2902–2904, Nov. 2008. DOI: 10.1002/mop.23855.
- [23] J. Colaco and R. B. Lohani, "Design and improvement in the performance of multi-band house-shaped microstrip patch antenna with srr-based metamaterial for 5g applications," in *ICT Systems and Sustainability*, M. Tuba, S. Akashe, and A. Joshi, Eds., Singapore: Springer Nature Singapore, 2022, pp. 85,94.
- [24] A. W. Rudge and K Milne, *The handbook of antenna design*. Iet, 1982, vol. 16.
- [25] I. I. Labiano and A. Alomainy, "Flexible inkjet-printed graphene antenna on kapton," *Flexible and Printed Electronics*, vol. 6, no. 2, p. 025 010, 2021. DOI: 10.1088/2058-8585/ac0ac1.
- [26] I. Marasco, G. Niro, F. Rizzi, M. De Vittorio, A. D'Orazio, and M. Grande, "Design of a pen-based flexible pifa antenna operating in the sub-6ghz band for 5g applications," in *2020 22nd International Conference on Transparent Optical Networks (ICTON)*, 2020, pp. 1–4. DOI: 10.1109/ICTON51198.2020.9203160.
- [27] I. Marasco *et al.*, "Compact and flexible meander antenna for surface acoustic wave sensors," *Microelectronic Engineering*, vol. 227, p. 111 322, 2020, ISSN: 0167-9317. DOI: <https://doi.org/10.1016/j.mee.2020.111322>. [Online]. Available: <https://www.sciencedirect.com/science/article/pii/S0167931720301106>.
- [28] G. A. Casula, G. Montisci, and G. Mazzarella, "A wideband pet inkjet-printed antenna for uhf rfid," *IEEE Antennas and Wireless Propagation Letters*, vol. 12, pp. 1400–1403, 2013. DOI: 10.1109/LAWP.2013.2287307.

- [29] L. Pazin and Y. Leviatan, "A compact 60-ghz tapered slot antenna printed on lcp substrate for wpan applications," *IEEE Antennas and Wireless Propagation Letters*, vol. 9, pp. 272–275, 2010. DOI: 10.1109/LAWP.2010.2046612.
- [30] M. Venkateswara Rao, B. T. P. Madhav, T. Anilkumar, and B. Prudhvinadh, "Circularly polarized flexible antenna on liquid crystal polymer substrate material with metamaterial loading," *Microwave and Optical Technology Letters*, vol. 62, no. 2, pp. 866–874, 2020. DOI: <https://doi.org/10.1002/mop.32088>.
- [31] N. B. Hernández, R. C. Williams, and E. W. Cochran, "The battle for the "green" polymer. different approaches for biopolymer synthesis: Bioadvantaged vs. bioreplacement.," *Organic & biomolecular chemistry*, vol. 12 18, pp. 2834–49, 2014.
- [32] P. Cataldi *et al.*, "Sustainable electronics based on crop plant extracts and graphene: A "bioadvantaged" approach," *Advanced Sustainable Systems*, vol. 2, no. 11, p. 1800069, 2018. DOI: <https://doi.org/10.1002/adsu.201800069>.
- [33] H. F. Khalili *et al.*, "Biodegradable dual semicircular patch antenna tile for smart floors," *IEEE Antennas and Wireless Propagation Letters*, vol. 18, no. 2, pp. 368–372, 2019. DOI: 10.1109/LAWP.2019.2891337.
- [34] S. de Holanda *et al.*, "Microstrip antenna based on knitted fabrics with biodegradable synthetic fibers," *Journal of Materials Science: Materials in Electronics*, vol. 28, Oct. 2017. DOI: 10.1007/s10854-017-7387-3.
- [35] A. Kinol, M. .D, D. Immanuel, N. Krishnamoorthy, G. Prince, and K. negash, "Design and fabrication of biodegradable antenna using jute material for uwb application," *Advances in Materials Science and Engineering*, vol. 2022, Mar. 2022. DOI: 10.1155/2022/2016737.

- [36] I. Locher, M. Klemm, T. Kirstein, and G. Troster, "Design and characterization of purely textile patch antennas," *IEEE Transactions on Advanced Packaging*, vol. 29, no. 4, pp. 777–788, 2006. DOI: 10.1109/TADVP.2006.884780.
- [37] Y. Kuang, L. Yao, H. Luan, S. Yu, R. Zhang, and Y. Qiu, "Effects of weaving structures and parameters on the radiation properties of three-dimensional fabric integrated microstrip antennas," *Textile Research Journal*, vol. 88, no. 19, pp. 2182–2189, 2018. DOI: 10.1177/0040517517716908.
- [38] M. D. Dickey, "Stretchable and soft electronics using liquid metals," *Advanced Materials*, vol. 29, no. 27, p. 1606425, 2017. DOI: <https://doi.org/10.1002/adma.201606425>.
- [39] Y. R. Jeong *et al.*, "A skin-attachable, stretchable integrated system based on liquid gainsn for wireless human motion monitoring with multi-site sensing capabilities," *NPG Asia Materials*, vol. 9, e443, Oct. 2017. DOI: 10.1038/am.2017.189.
- [40] Y. Lin, C. Cooper, M. Wang, J. J. Adams, J. Genzer, and M. D. Dickey, "Handwritten, soft circuit boards and antennas using liquid metal nanoparticles," *Small*, vol. 11, no. 48, pp. 6397–6403, 2015. DOI: <https://doi.org/10.1002/sm11.201502692>.
- [41] K. Guerchouche, E. Herth, L. E. Calvet, N. Roland, and C. Loyez, "Conductive polymer based antenna for wireless green sensors applications," *Microelectronic Engineering*, vol. 182, pp. 46–52, 2017, ISSN: 0167-9317. DOI: <https://doi.org/10.1016/j.mee.2017.08.007>.
- [42] G. G. Xiao, Z. Zhang, S. Lang, and Y. Tao, "Screen printing rf antennas," in *2016 17th International Symposium on Antenna Technology and Applied Electromagnetics (ANTEM)*, 2016, pp. 1–2. DOI: 10.1109/ANTEM.2016.7550245.
- [43] S. Smith, A. Oberholzer, K. Land, J. Korvink, and D. Mager, "Functional screen printed rfid tags on flexible substrates, facilitating low-

- cost and integrated point-of-care diagnostics,” *Flexible and Printed Electronics*, vol. 3, Apr. 2018. DOI: 10.1088/2058-8585/aabc8c.
- [44] I. Ibanez Labiano, D. Arslan, E. Ozden Yenigun, A. Asadi, H. Cebeci, and A. Alomainy, “Screen printing carbon nanotubes textiles antennas for smart wearables,” *Sensors*, vol. 21, no. 14, 2021, ISSN: 1424-8220. DOI: 10.3390/s21144934.
- [45] H. Sun, G. Xiao, S. Lang, Z. Zhang, and Y. Tao, “Screen printed hf rfid antennas on polyethylene terephthalate film,” *IEEE Journal of Radio Frequency Identification*, vol. 3, no. 2, pp. 91–97, 2019. DOI: 10.1109/JRFID.2019.2905418.
- [46] H. F. Abutarboush, M. F. Farooqui, and A. Shamim, “Inkjet-printed wideband antenna on resin-coated paper substrate for curved wireless devices,” *IEEE Antennas and Wireless Propagation Letters*, vol. 15, pp. 20–23, 2016. DOI: 10.1109/LAWP.2015.2425797.
- [47] H. F. Abutarboush and A. Shamim, “A reconfigurable inkjet-printed antenna on paper substrate for wireless applications,” *IEEE Antennas and Wireless Propagation Letters*, vol. 17, no. 9, pp. 1648–1651, 2018. DOI: 10.1109/LAWP.2018.2861386.
- [48] W. G. Whittow *et al.*, “Inkjet-printed microstrip patch antennas realized on textile for wearable applications,” *IEEE Antennas and Wireless Propagation Letters*, vol. 13, pp. 71–74, 2014. DOI: 10.1109/LAWP.2013.2295942.
- [49] B. K. Tehrani, B. S. Cook, and M. M. Tentzeris, “Inkjet printing of multilayer millimeter-wave yagi-uda antennas on flexible substrates,” *IEEE Antennas and Wireless Propagation Letters*, vol. 15, pp. 143–146, 2016. DOI: 10.1109/LAWP.2015.2434823.
- [50] L. Natta *et al.*, “Conformable aln piezoelectric sensors as a non-invasive approach for swallowing disorder assessment,” *ACS sensors*, vol. 6, no. 5, pp. 1761–1769, 2021.
- [51] C. A. Balanis, *Antenna theory: analysis and design*. John wiley & sons, 2015.

- [52] D. Poljak and M. Cvetkovic, *Human Interaction with Electromagnetic Fields: Computational Models in Dosimetry*. Academic Press, 2019.
- [53] V. Monebhurrin, “Revision of iee standard 145-2013: Ieee standard for definitions of terms for antennas [stand on standards],” *IEEE Antennas and Propagation Magazine*, vol. 62, no. 3, pp. 117–117, 2020.
- [54] A. F. Oskooi, D. Roundy, M. Ibanescu, P. Bermel, J. D. Joannopoulos, and S. G. Johnson, “Meep: A flexible free-software package for electromagnetic simulations by the fdtd method,” *Computer Physics Communications*, vol. 181, no. 3, pp. 687–702, 2010.
- [55] K. Fujii *et al.*, “Study on the transmission mechanism for wearable device using the human body as a transmission channel,” *IEICE transactions on communications*, vol. 88, no. 6, pp. 2401–2410, 2005.
- [56] A. Sani, Y. Zhao, Y. Hao, A. Alomainy, and C. Parini, “An efficient fdtd algorithm based on the equivalence principle for analyzing on-body antenna performance,” *IEEE Transactions on Antennas and Propagation*, vol. 57, no. 4, pp. 1006–1014, 2009.
- [57] F. Yang and Y. Rahmat-Samii, *Electromagnetic band gap structures in antenna engineering*. Cambridge university press Cambridge, UK, 2009.
- [58] D. M. Sheen, S. M. Ali, M. D. Abouzahra, and J.-A. Kong, “Application of the three-dimensional finite-difference time-domain method to the analysis of planar microstrip circuits,” *IEEE Transactions on microwave theory and techniques*, vol. 38, no. 7, pp. 849–857, 1990.
- [59] H. Mosallaei and K. Sarabandi, “Antenna miniaturization and bandwidth enhancement using a reactive impedance substrate,” *IEEE Transactions on antennas and propagation*, vol. 52, no. 9, pp. 2403–2414, 2004.
- [60] J. Kim and Y. Rahmat-Samii, “Implanted antennas inside a human body: Simulations, designs, and characterizations,” *IEEE Transactions on microwave theory and techniques*, vol. 52, no. 8, pp. 1934–1943, 2004.

- [61] S. C. Hagness, A. Taflove, and S. D. Gedney, "Finite-difference time-domain methods," *Handbook of numerical analysis*, vol. 13, pp. 199–315, 2005.
- [62] S. Gedency, "An anisotropic perfectly matched layered-absorbing medium for the truncation of fdtd lattice," *IEEE Trans Antennas Propagat*, vol. 44, no. 12, pp. 1630–1939, 1996.
- [63] M. Ruiz-Cabello N, M. Abaļenkovs, L. M. Diaz Angulo, C. Cobos Sanchez, F. Moglie, and S. G. Garcia, "Performance of parallel fdtd method for shared-and distributed-memory architectures: Application tobioelectromagnetics," *Plos one*, vol. 15, no. 9, e0238115, 2020.
- [64] W. Yu, R. Mittra, X. Yang, Y. Liu, Q. Rao, and A. Muto, "High-performance conformal fdtd techniques," *IEEE Microwave Magazine*, vol. 11, no. 4, pp. 43–55, 2010.
- [65] A. Hassan, S. Ali, G. Hassan, J. Bae, and C. H. Lee, "Inkjet-printed antenna on thin pet substrate for dual band wi-fi communications," *Microsystem Technologies*, vol. 23, no. 8, pp. 3701–3709, 2017.
- [66] L. Ukkonen, L. Sydanheimo, and M. Kivikoski, "Effects of metallic plate size on the performance of microstrip patch-type tag antennas for passive rfid," *IEEE Antennas and Wireless Propagation Letters*, vol. 4, pp. 410–413, 2005.
- [67] S.-S. Hsu, K.-C. Wei, C.-Y. Hsu, and H. Ru-Chuang, "A 60-ghz millimeter-wave cpw-fed yagi antenna fabricated by using $0.18 - \mu$ cmos technology," *IEEE Electron Device Letters*, vol. 29, no. 6, pp. 625–627, 2008.
- [68] R. Streich, "3d finite-difference frequency-domain modeling of controlled-source electromagnetic data: Direct solution and optimization for high accuracy," *Geophysics*, vol. 74, no. 5, F95–F105, 2009.
- [69] M. N. Sadiku, "A simple introduction to finite element analysis of electromagnetic problems," *IEEE Transactions on education*, vol. 32, no. 2, pp. 85–93, 1989.

- [70] R. Carter, *The method of moments in electromagnetics, by wc gibson: Scope: Modelling of electromagnetic radiation and scattering problems. level: Postgraduate and professional*, 2010.
- [71] S. M. Mikki and Y. M. Antar, "The antenna current green's function formalism—part i," *IEEE Transactions on Antennas and Propagation*, vol. 61, no. 9, pp. 4493–4504, 2013.
- [72] T Rappaport, "Wireless communications principles and practice edition," 2001.
- [73] C. Perez-Vega, J. M. L. Higuera, *et al.*, "A simple and efficient model for indoor path-loss prediction," *Measurement science and technology*, vol. 8, no. 10, p. 1166, 1997.
- [74] M. Lamsalli, A. El Hamichi, M. Boussouis, N. A. Touhami, and T. Elhamadi, "Genetic algorithm optimization for microstrip patch antenna miniaturization," *Progress In Electromagnetics Research Letters*, vol. 60, pp. 113–120, 2016.
- [75] .
- [76] L. Lillwitz, "Production of dimethyl-2, 6-naphthalenedicarboxylate: Precursor to polyethylene naphthalate," *Applied Catalysis A: General*, vol. 221, no. 1-2, pp. 337–358, 2001.
- [77] S. G. Kirtania *et al.*, "Flexible antennas: A review," *Micromachines*, vol. 11, no. 9, p. 847, 2020.
- [78] P. Kumar, T. Ali, and A. Sharma, "Flexible substrate based printed wearable antennas for wireless body area networks medical applications," *Radioelectronics and Communications Systems*, vol. 64, no. 7, pp. 337–350, 2021.
- [79] J. R. Sampson, *Adaptation in natural and artificial systems (john h. holland)*, 1976.
- [80] A. D. Irfianti, R. Wardoyo, S. Hartati, and E. Sulistyoningsih, "Determination of selection method in genetic algorithm for land suitability," in *MATEC Web of Conferences*, EDP Sciences, vol. 58, 2016, p. 03 002.

- [81] S. Naoui, L. Latrach, and A. Gharsallah, “Equivalent circuit model of double split ring resonators,” *Int. J. Microw. Opt. Technol.*, vol. 11, no. 1, pp. 1–6, 2016.
- [82] N. Aggarwall, G Kumar, and K. Ray, “Wide-band planar monopole antenna,” *IEEE Trans. Antennas Propag.*, vol. 46, no. 2, pp. 294–295, 1998.
- [83] M. S. Wegmueller *et al.*, “An attempt to model the human body as a communication channel,” *IEEE transactions on Biomedical Engineering*, vol. 54, no. 10, pp. 1851–1857, 2007.
- [84] Y. Song, Q. Hao, K. Zhang, M. Wang, Y. Chu, and B. Kang, “The simulation method of the galvanic coupling intrabody communication with different signal transmission paths,” *IEEE Transactions on Instrumentation and Measurement*, vol. 60, no. 4, pp. 1257–1266, 2010.
- [85] P.-Y. Lyu, C.-P. Chuang, C.-C. Chang, S.-F. Chang, and N. T. P. Nguyen, “Connector induced effect on small antenna design,” in *2018 IEEE International RF and Microwave Conference (RFM)*, IEEE, 2018, pp. 178–181.
- [86] W.-J. Tsay and J. T. Aberle, “Analysis of a microstrip line terminated with a shorting pin,” *IEEE transactions on microwave theory and techniques*, vol. 40, no. 4, pp. 645–651, 1992.
- [87] W.-H. Ng, Y.-H. Lee, E.-H. Lim, and B.-K. Chung, “Design of a compact pifa tag antenna for wearable electronics,” in *2018 IEEE 38th International Electronics Manufacturing Technology Conference (IEMT)*, IEEE, 2018, pp. 1–4.
- [88] G.-P. Gao, C. Yang, B. Hu, R.-F. Zhang, and S.-F. Wang, “A wide-bandwidth wearable all-textile pifa with dual resonance modes for 5 ghz wlan applications,” *IEEE Transactions on Antennas and Propagation*, vol. 67, no. 6, pp. 4206–4211, 2019.

- [89] H. Aliakbarian, A. Hajiahmadi, N. M. Saaid, and P. J. Soh, "Evaluation of a textile pifa for wearable iot application and its challenges," *ECTI Transactions on Computer and Information Technology (ECTI-CIT)*, vol. 15, no. 3, pp. 289–302, 2021.
- [90] P. Nguyen-Tri, P. Ghassemi, P. Carriere, S. Nanda, A. A. Assadi, and D. D. Nguyen, "Recent applications of advanced atomic force microscopy in polymer science: A review," *Polymers*, vol. 12, no. 5, p. 1142, 2020.
- [91] G. de Marzo *et al.*, "Sustainable, flexible, and biocompatible enhanced piezoelectric chitosan thin film for compliant piezosensors for human health," *Advanced Electronic Materials*, p. 2200069, 2022.
- [92] X. Yang and M. Zhang, "Review of flexible microelectromechanical system sensors and devices," *Nanotechnology and Precision Engineering*, vol. 4, no. 2, p. 025001, 2021.
- [93] G. Niro, I. Marasco, F. Rizzi, A. D'Orazio, M. De Vittorio, and M. Grande, "Design of a surface acoustic wave resonator for sensing platforms," in *2020 IEEE International Symposium on Medical Measurements and Applications (MeMeA)*, IEEE, 2020, pp. 1–6.
- [94] C. Boehler, Z. Aqrave, and M. Asplund, "Applications of pedot in bioelectronic medicine," *Bioelectronics in Medicine*, vol. 2, no. 2, pp. 89–99, 2019.
- [95] H. A. Wheeler, "Formulas for the skin effect," *Proceedings of the IRE*, vol. 30, no. 9, pp. 412–424, 1942.
- [96] S. J. Chen, C. Fumeaux, P. Talemi, B. Chivers, and R. Shepherd, "Progress in conductive polymer antennas based on free-standing polypyrrole and pedot: Pss," in *2016 17th International Symposium on Antenna Technology and Applied Electromagnetics (ANTEM)*, IEEE, 2016, pp. 1–4.

- [97] D. Alemu, H.-Y. Wei, K.-C. Ho, and C.-W. Chu, “Highly conductive PEDOT:PSS electrode by simple film treatment with methanol for ITO-free polymer solar cells,” *Energy & Environmental Science*, vol. 5, no. 11, pp. 9662–9671, 2012.
- [98] L. Shafai, S. Latif, and C. Shafai, “Loss reduction in planar circuits and antennas over a ground plane using engineered conductors,” in *2013 7th European Conference on Antennas and Propagation (EuCAP)*, IEEE, 2013, pp. 1031–1035.
- [99] S. I. Latif, L. Shafai, and C. Shafai, “An engineered conductor for gain and efficiency improvement of miniaturized microstrip antennas,” *IEEE Antennas and Propagation Magazine*, vol. 55, no. 2, pp. 77–90, 2013.
- [100] N. Kant *et al.*, “Continuous vital sign monitoring using a wearable patch sensor in obese patients: A validation study in a clinical setting,” *Journal of Clinical Monitoring and Computing*, vol. 36, no. 5, pp. 1449–1459, 2022.
- [101] K. G. Heimrich, T. Lehmann, P. Schlattmann, and T. Prell, “Heart rate variability analyses in Parkinson’s disease: A systematic review and meta-analysis,” *Brain Sciences*, vol. 11, no. 8, p. 959, 2021.
- [102] F. Mazda, *Telecommunications engineer’s reference book*. Butterworth-Heinemann, 2014.
- [103] P. Li, C. Karmakar, C. Liu, and C. Liu, “Analysing effect of heart rate and age on radial artery pressure derived systolic and diastolic durations in healthy adults,” in *2015 Computing in Cardiology Conference (CinC)*, IEEE, 2015, pp. 381–384.
- [104] G. Plehn *et al.*, “Loss of diastolic time as a mechanism of exercise-induced diastolic dysfunction in dilated cardiomyopathy,” *American Heart Journal*, vol. 155, no. 6, pp. 1013–1019, 2008.

- [105] T. Bombardini, R. Sicari, E. Bianchini, and E. Picano, “Abnormal shortened diastolic time length at increasing heart rates in patients with abnormal exercise-induced increase in pulmonary artery pressure,” *Cardiovascular Ultrasound*, vol. 9, no. 1, pp. 1–9, 2011.